

AD-759 556

CdGeAs₂ AND CdGeP₂ CHALCOPYRITE MATERIALS
FOR INFRARED NON LINEAR OPTICS

Helge Kildal

Stanford University

Prepared for:

Air Force Materials Laboratory

December 1972

DISTRIBUTED BY:

NTIS

National Technical Information Service
U. S. DEPARTMENT OF COMMERCE
5285 Port Royal Road, Springfield Va. 22151

CdGeAs_2 AND CdGeP_2 CHALCOPYRITE MATERIALS
FOR INFRARED NONLINEAR OPTICS

HELGE KILDAL
STANFORD UNIVERSITY

AD 739556

TECHNICAL REPORT AFML-TR-72-277

December 1972



Approved for public release; distribution unlimited.

Reproduced by
NATIONAL TECHNICAL
INFORMATION SERVICE
U S Department of Commerce
Springfield VA 22151

AIR FORCE MATERIALS LABORATORY
AIR FORCE SYSTEMS COMMAND
WRIGHT-PATTERSON AIR FORCE BASE, OHIO

184

NOTICE

When Government drawings, specifications, or other data are used for any purpose other than in connection with a definitely related Government procurement operation, the United States Government thereby incurs no responsibility nor any obligation whatsoever; and the fact that the government may have formulated, furnished, or in any way supplied the said drawings, specifications, or other data, is not to be regarded by implication or otherwise as in any manner licensing the holder or any other person or corporation, or conveying any rights or permission to manufacture, use, or sell any patented invention that may in any way be related thereto.

ADDITIONAL FOR	
NTIS	WITH SPILLS <input checked="" type="checkbox"/>
9 2	2-1-1962 <input type="checkbox"/>
DATE: 11/1/62	<input type="checkbox"/>
BY	
DISTRIBUTION/AVAILABILITY NOTES	
CIS: Avail. day / week	
A	

Copies of this report should not be returned unless return is required by security considerations, contractual obligations, or notice on a specific document.

DOCUMENT CONTROL DATA - R & D

(Security classification of title, body of abstract and indexing annotation must be entered when the overall report is classified)

1. ORIGINATING ACTIVITY (Corporate author)

W. W. Hansen Laboratory of Physics
Stanford University
Stanford, California

2a. REPORT SECURITY CLASSIFICATION

UNCLASSIFIED

2b. GROUP

N/A

3. REPORT TITLE

CdGeAs₂ and CdGeP₂ Chalcopyrite Materials for Infrared Nonlinear Optics

4. DESCRIPTIVE NOTES (Type of report and inclusive dates)

Final Report, 1 August 1970 - 31 July 1972

5. AUTHOR(S) (First name, middle initial, last name)

Helge Kildal

6. REPORT DATE

December 1972

7a. TOTAL NO. OF PAGES

370 184

7b. NO. OF REFS

66

8a. CONTRACT OR GRANT NO.

F33615-70-C-1640

b. PROJECT NO.

ARPA Order 1636

d.

9a. ORIGINATOR'S REPORT NUMBER(S)

AFML-TR-72-277

9b. OTHER REPORT NO(S) (Any other numbers that may be assigned this report)

M.L. Report No. 2118

10. DISTRIBUTION STATEMENT

Approved for public release; distribution unlimited.

11. SUPPLEMENTARY NOTES

12. SPONSORING MILITARY ACTIVITY

Air Force Materials Laboratory (LPL)
Air Force Systems Command
Wright-Patterson AFB, Ohio 45433

13. ABSTRACT

This work reports on new crystals for infrared nonlinear optics. The investigated crystals are II-IV-V₂ semiconductor compounds with chalcopyrite structure. We give both theoretical and experimental results on growth technique, material quality problems, semiconducting properties that affect the optical properties, and finally we discuss the linear and the nonlinear optical properties.

One of the crystals, CdGeAs₂, we have found to have the highest figure of merit of any presently available infrared nonlinear material. In addition the crystal has an extensive parametric tuning range between 3 and 18 μm. Using a TEA CO₂ laser we have observed a doubling efficiency of 2 percent in a 2 mm crystal.

The bandstructure of the chalcopyrites near the Brillouin zone center has also been determined, and we find good agreement between the calculated and the measured intraband absorption in p-type CdGeAs₂.

14.

KEY WORDS

LINK A

LINK B

LINK C

ROLE

WT

ROLE

WT

ROLE

WT

Chalcopyrite crystals

Nonlinear optics

Cadmium germanium diarsenide

Cadmium germanium diphosphide

Band structure of chalcopyrites

Index of refraction

Nonlinear optical properties

Second harmonic generation

Third harmonic generation

Pulsed carbon dioxide lasers

UNCLASSIFIED

Security Classification

CdGeAs_2 AND CdGeP_2 CHALCOPYRITE MATERIALS
FOR INFRARED NONLINEAR OPTICS

HELGE KILDAL
STANFORD UNIVERSITY

Approved for public release; distribution unlimited.

12

ERRATA SHEET FOR
CdGeAs₂ AND CdGeP₂ CHALCOPYRITE MATERIALS
FOR INFRARED NONLINEAR OPTICS

Page No.

- viii Figure 18 -- Change y to φ .
- viii Figure 21 -- Change transistors to transitions.
- viii Figure 26a -- CdGeHs₂ should read "CdGeAs₂".
- 18 Sixth Line, second term should be changed from
 $|2^{-1/2}(X + iY)\downarrow\rangle$ to $|-2^{-1/2}(X + iY)\downarrow\rangle$
- 49 Table III -- °C should read (°C).
- 58 Figure 12 should be replaced by Figure 14, page 63.
- 63 Figure 14 should be replaced by Figure 16, page 69.
- 69 Figure 16 should be replaced by the figure included in the
 Errata Sheet
- 111 Figure 21 -- In the caption, change "transistors" to read
 "transitions". Also, $p = 10^{16}$ should read $p = 2 \times 10^{16}$.
- 124 Figure 26a -- Change CdGeHs₂ to read CdGeAs₂.
- 133 Table XVI -- ℓ_c [m] should read ℓ_c [μ m] .
- 148 Figure 33 -- $p = 1.2 \times 10^{15} \text{ cm}^{-3}$ should read $p = 2.4 \times 10^{15} \text{ cm}^{-3}$


FOREWORD

This report covers work performed under Contract F33615-70-C-1640, by the Microwave Laboratory, W. W. Hansen Laboratory of Physics, Stanford University, Stanford, California. This research was sponsored by the Advanced Research Projects Agency under ARPA Order 1636. The technical monitor of the contract was Vincent L. Donlan, Air Force Materials Laboratory, Air Force Systems Command, Wright-Patterson Air Force Base, Ohio. The period of performance was 1 August 1970 to 31 July 1972.

The author expresses his thanks to the Microwave Laboratory and in particular to his research advisor, Professor R. L. Byer. The support of other students in Professor Byer's group, R. F. Begley, M. M. Choy, R. L. Herbst, and C. B. Roundy, is also acknowledged. The author is indebted to R. S. Feigelson, H. W. Swarts, and R. J. Raymakers of the Stanford Center for Materials Research for providing the chalcopyrite crystals, and to R. F. Griffin for orienting and polishing the crystals. The author thanks Professors S. Harris, H. Heffner, and A. E. Siegman for critical reading of the manuscript and Mrs. Valerie Lipinski, Mrs. Iona Williams, and Mr. N. Bettini for their invaluable assistance in preparing the manuscript.

This report was released by the author for publication as a Technical Report in November 1972.

This technical report has been reviewed and is approved.



WILLIAM GOLDBERG, Major, USAF
Chief, Laser & Optical Materials Branch
Electromagnetic Materials Division
Air Force Materials Laboratory

TABLE OF CONTENTS

	<u>Page</u>
I. Introduction.	1
II. Selection of Crystals for Nonlinear Optics.	4
A. General consideration	4
B. Estimation of the optical properties of the II-IV-V ₂ chalcopyrite compounds.	6
III. Bandstructure of the Chalcopyrites in the Vicinity of $k=0$. .	15
IV. Electric Properties and the Linear Thermal Expansion	
Coefficient of CdGeAs ₂	32
A. Electric transport properties	35
B. Measurement of the linear thermal expansion coefficient .	44
V. Crystal Growth and Material Evaluation.	55
A. Growth method	55
B. Initial testing	59
C. Other tests	66
VI. Linear and Nonlinear Optical Properties	76
A. Theory.	76
B. Experimental results.	114
VII. Application of Tunable Radiation for Air Pollution	
Detection	149
VIII. Conclusion.	150

TABLE OF CONTENTS (Cont'd)

	<u>Page</u>
APPENDIX A. Type I and Type II Phasematching Equations.	153
APPENDIX B. Second Harmonic Generation in a Wedged Platelet . . .	156
REFERENCES.	163

LIST OF FIGURES

<u>Figure</u>		<u>Page</u>
1.	Chalcopyrite unit cell.....	8
2.	Two and three phonon absorption in CdGeAs_2	11
3.	CdGeAs_2 band structure near $k = 0$	29
4.	Calculated intrinsic carrier concentration in CdGeAs_2	37
5.	Temperature dependence of the Hall constant for p-type CdGeAs_2	41
6.	Temperature dependence of the resistivity for p-type CdGeAs_2	43
7.	Experimental setup for measuring the linear thermal expansion coefficient.....	46
8.	dn_T/dT for dry air at 760 mm Hg.....	48
9.	Linear thermal expansion coefficient for silicon.....	50
10.	Linear thermal expansion coefficient for CdGeAs_2	54
11.	Oven gradient and quartz crucible for Bridgman- Stockbarger growth of CdGeAs_2	56
12.	CdGeAs_2 boule grown by the Bridgman method.....	58
13.	Transmittance of a single crystal of p-type CdGeAs_2 ...	62
14.	Transmission through CdGeP_2 photographed through an IR microscope.....	63
15.	Measured transmission range for n-type CdGeP_2	64

LIST OF FIGURES (CONT'D)

<u>Figure</u>		<u>Page</u>
16.	Etched CdGeAs ₂ slice number 9 from boule number 34.....	69
17.	Type I and type II phasematching in a positive birefringent crystal of $\bar{4}2m$ symmetry.....	78
18.	Definition of the angles θ , γ , and α for third order optical interactions.....	94
19.	Index of refraction measurement apparatus.....	98
20.	Determination of the birefringence by the platelet method.....	102
21.	Calculated total absorption coefficient for transitors between the split valence bands in p-type CdGeAs ₂ at three different temperatures but assuming a constant carrier concentration.....	111
22.	Index of refraction for CdGeAs ₂	117
23.	Temperature dependence of the birefringence in CdGeAs ₂ at 3.39 μm	119
24.	Type I and type II phasematching angles for SHG in CdGeAs ₂	121
25.	Theoretical tuning curves for CdGeAs ₂ for 90° type II phasematching	123
26a.	Theoretical tuning curves for type I phasematching in CdGeAs ₂ for several pump wavelengths.....	124
26b.	Theoretical tuning curves for type II phasematching in CdGeAs ₂ for several pump wavelengths.....	125

LIST OF FIGURES (CONT'D)

<u>Figure</u>		<u>Page</u>
27a.	Theoretical tuning curve and minimum bandwidth for type I phasematching for a one cm CdGeAs ₂ crystal pumped by a pump wavelength of 5.3 μm.....	126
27b	Theoretical tuning curve and minimum bandwidth for type II phasematching for a one cm CdGeAs ₂ crystal pumped by a pump wavelength of 5.3 μm.....	127
28.	Indices of refraction for CdGeP ₂	130
29.	Measurement of the nonlinear coefficients.....	131
30.	Angular dependence of the second harmonic output power.....	140
31.	Variation in the SHG output power over the crystal cross section.....	142
32.	Free electron absorption in n-type CdGeAs ₂	146
33.	Intra band absorption in p-type CdGeAs ₂	148
34.	Geometry for SHG in a wedged platelet	157

LIST OF TABLES

<u>Table</u>		<u>Page</u>
I.	Optical properties of the chalcopyrites.....	10
II.	Calculated valence band splitting energies and effective masses for the conduction and valence bands.....	27
III.	Linear thermal expansion coefficient for silicon.....	49
IV.	Linear thermal a-Axis expansion coefficient for CdGeAs ₂ .	52
V.	Linear thermal c-Axis expansion coefficient for CdGeAs ₂ .	53
VI.	Magnitude of $W_s F_s / F_u$ for microprobe analysis of CdGeAs ₂ .	68
VII.	Microprobe analysis of slice No. 9 from boule No. 3 ⁴ of CdGeAs ₂	70
VIII.	Microprobe Analysis of CdGeAs ₂	71
IX.	Impurity concentrations in cadmium germanium arsenide (in parts per million atomic).....	74
X.	Impurity concentrations in cadmium germanium arsenide (in parts per million atomic).....	75
XI.	Contracted notation for the third order nonlinear coefficient.....	92
XII.	Maximum effective third order nonlinear coefficient.....	95
XIII.	Measured indices of refraction for CdGeAs ₂	115
XIV.	Temperature dependence of the indices of refraction for CdGeAs ₂	118
XV.	Measured indices of refraction for CdGeP ₂	128

LIST OF TABLES (CONT'D)

<u>Table</u>	<u>Page</u>
XVI. Measurement of the SHG nonlinear coefficient.....	133
XVII. Figure of merits for infrared nonlinear crystals.....	136
XVIII. Phasematching experiments.....	138

CHAPTER I

INTRODUCTION

This work considers the development of new materials for applications in infrared nonlinear optics. The investigated crystals belong to the II-IV-V₂ class of ternary semiconductors with chalcopyrite structure. We discuss growth technique, materials quality problems, absorption mechanisms, semiconducting properties, and linear and nonlinear optical properties for two of the compounds: CdGeAs₂ and CdGeP₂.

In general nonlinear crystals are used to generate coherent radiation at wavelengths where lasers are not available. The process can be second harmonic generation (SHG), mixing, or parametric oscillation.

Since nonlinear optics require high optical power densities the material quality problems are extremely important. Also, the crystals must be phasematchable and have a high nonlinear figure of merit to give good nonlinear interaction efficiencies. Several useful crystals exist for the visible spectral region. In the infrared, however, there is a lack of high quality nonlinear crystals.

As a result of this study, CdGeAs₂ has been shown to have the highest figure of merit of any presently available infrared nonlinear material. With a positive birefringence of 0.1, CdGeAs₂ is phase-matchable for SHG and parametric interactions over most of its transparency range from 2.4 to 18 μm . By SHG of a TEA CO₂ laser we have observed a doubling efficiency of 2 percent.

To improve the understanding of the optical absorption mechanisms we have measured the semiconductor properties and determined the band structure near the Brillouin zone center. We have identified one of the absorption mechanisms in CdGeAs_2 as due to intraband transitions between the split valence bands. This absorption is avoided by reducing the hole concentration through compensation or doping.

The II-IV- V_2 chalcopyrite compounds were first synthesized in the late nineteen fifties.^{1,2} Over the past ten years Russian workers have reported extensive work on the compounds.³ We had therefore information about melting points and several attempted growth methods when the chalcopyrite growth program started at Stanford in the fall of 1969. The important properties for nonlinear optics such as dispersion, birefringence, and nonlinear coefficients were not known, but from the close resemblance with the III-V compounds we assumed that the nonlinear coefficients were large. From the crystal structure it was clear that the crystals would be birefringent because of the tetragonal distortion of the unit cell. We did not know, however, if the birefringence would be sufficient to satisfy the phasematching condition. Today, due to the recent work at Stanford and the Bell Telephone Laboratories, the potential of the II-IV- V_2 chalcopyrite compounds for nonlinear optics is fully confirmed.

The long-term goal of this research is to develop chalcopyrite crystals of high enough optical quality for the construction of a parametric oscillator tunable over the infrared frequency range. In Chapter VII we discuss the potential use of tunable infrared radiation

to detect air pollutants and compare the sensitivity with alternative laser detection schemes.

SELECTION OF CRYSTALS FOR NONLINEAR OPTICS

A. GENERAL CONSIDERATION

This chapter reviews briefly the crystal parameters of importance for nonlinear optics and introduces the properties of the chalcopyrite compounds. To evaluate nonlinear crystals it is necessary to consider the following properties:

1. Large nonlinear coefficient.
2. Sufficient birefringence for phasematching.
3. Crystal transparency range.
4. Optical quality.

The second order nonlinear coefficient d_{ijk} is defined by^{4,5}

$$P_i^{NL}(\omega_3) = d_{ijk} E_j(\omega_1) E_k(\omega_2) \quad (2.1)$$

with summation over repeated indices. In this equation $P_i^{NL}(\omega_3)$ is the nonlinear polarization generated by the electric fields $E_j(\omega_1)$ and $E_k(\omega_2)$. The symmetry of the d_{ijk} tensor follows from the crystal point group symmetry.⁶ For the crystal to have a nonvanishing nonlinear coefficient it cannot have a center of symmetry. In materials where the nonlinear coefficient has not been measured, the magnitude can be estimated by Miller's rule⁷ if the indices of refraction are known. The Miller's rule relates the indices of refraction n to the nonlinear

coefficient by

$$d_{ijk} = \delta_{ijk}(n_i^2 - 1)(n_j^2 - 1)(n_k^2 - 1) , \quad (2.2)$$

where δ_{ijk} is the Miller's constant. For most materials, δ_{ijk} is constant to within a factor of two while the nonlinear coefficient can vary over almost four orders of magnitude. Miller's rule works very well especially for crystals with the same point group symmetry.

The nonlinear polarization drives an electric field at ω_3 . In order for the driving polarization to stay in phase with the resulting electric field over the whole crystal length the phasematching condition

$$k_3 = k_1 + k_2 \quad (2.3)$$

must be satisfied. Since $k = n\omega/c$, we can rewrite the equation as

$$n_3\omega_3 = n_1\omega_1 + n_2\omega_2 . \quad (2.4)$$

In addition, energy conservation requires

$$\omega_3 = \omega_1 + \omega_2 . \quad (2.5)$$

In crystals we accomplish phasematching by using the birefringence to compensate for the dispersion in the indices of refraction. The condition that the crystals should have sufficient birefringence to achieve phasematching sets a very important limit on the number of crystals useful for nonlinear optics. Degenerate parametric oscillators or second harmonic generation (SHG) require the largest birefringence. The

phasematching angle for SHG is approximately given by (cf. Appendix A)

$$\sin \theta_I \approx \sqrt{D/|B|} \quad (2.6)$$

for type I phasematching and

$$\sin \theta_{II} \approx \sqrt{2D/|B|} \quad (2.7)$$

for type II phasematching. Here $B = n_e - n_o$ is the birefringence and $D = n_o^{2\omega} - n_o^\omega$ is the dispersion. The crystals must therefore have a birefringence larger than the dispersion between the second harmonic and the fundamental frequency.

The transmission range of crystals is determined by the bandgap absorption at short wavelengths and by two-phonon absorption at long wavelengths. Since efficient nonlinear interactions require high optical power densities, the absorption within the transparency range must be at an absolute minimum to avoid crystal damage or breaking of the phasematching condition. For reference, in a high optical quality infrared material such as GaAs the absorption is 0.02 cm^{-1} ,⁹ and the optical damage threshold is approximately 100 MW/cm^2 .¹⁰ Nonlinear absorption is also important and may even limit the maximum efficiency of the nonlinear interaction. We will discuss this in Chapter VI.

B. ESTIMATION OF THE OPTICAL PROPERTIES OF THE II-IV-V₂ CHALCOPYRITE COMPOUNDS

The III-V semiconductors have large nonlinear coefficients,¹¹ but due to the cubic symmetry they have no birefringence and phasematching is therefore not possible. If we replace the cation in the III-V

compounds with atoms from the second and fourth column of the periodic table, we generate a new class of crystals known as the II-IV-V₂ chalcopyrite compounds. These have very similar optical properties but with the important addition that they are birefringent. The chalcopyrite crystal structure is tetragonal and the point group symmetry of $\bar{4}2m$ allows both type I and type II phasematching.⁴

Figure 1 shows the atomic arrangement in the chalcopyrite unit cell.¹² The lattice parameters are a and c . Each cell contains four II-IV-V₂ formulas. If the II and IV atoms were indistinguishable, the chalcopyrite structure would reduce to a compressed sphalerite structure. However, because of the ordered arrangement of the II and IV atoms, the chalcopyrite unit cell is twice the sphalerite cell. The II and IV cations have different covalent radii, and the anion V is therefore not exactly in the center of the cation tetrahedra. It is positioned a distance $a(x - 1/4)$ off the center closer to the cations with the smallest radii.¹³ We can characterize the chalcopyrite structure by two parameters τ and σ where $\tau = 2 - c/a$ is the tetragonal compression and $\sigma = 4x - 1$ gives the position of the anion.

The growth of high optical quality material presents several problems. For maximum progress we decided to concentrate on a few compounds. In choosing which compounds to grow, the important considerations were transmission range, birefringence, and magnitude of the nonlinear coefficients. When we started the growth, the only

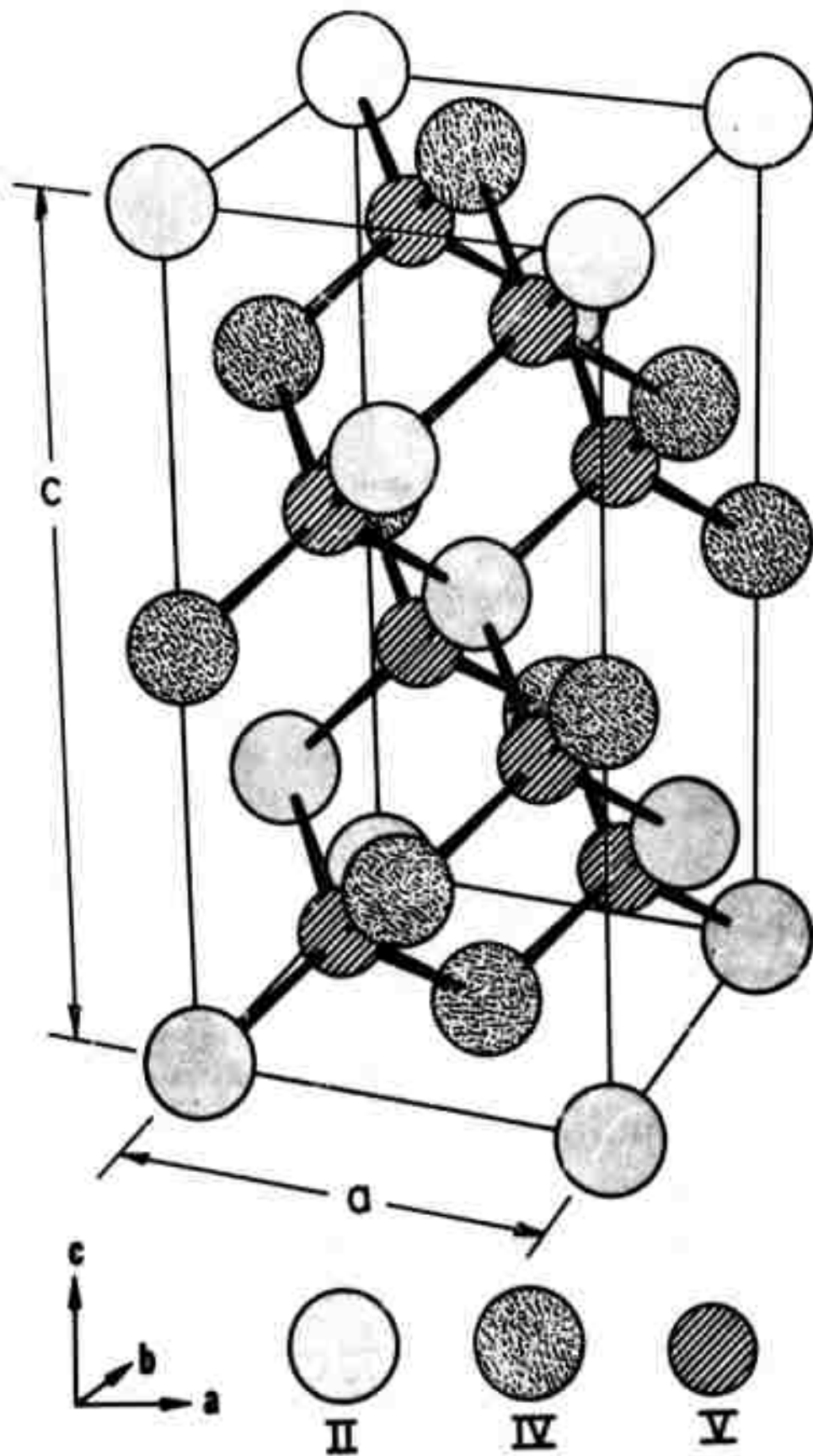


FIG. 1--Chalcopyrite unit cell.

useful information available was the crystal structure and the bandgap frequency. The other important properties such as the infrared cut-off frequency, the nonlinear coefficients, and the birefringence had not been measured. We therefore used the close resemblance with the III-V analogs to predict the properties. For reference the III-V analogs are listed in Table I. As pointed out, two-phonon absorption determines the infrared cut-off frequency, and the frequency is approximately twice the transverse optical mode frequency at the Brillouin zone center. When we assume the same force constants for the chalcopyrite bonds as for the III-V analogs, we estimate the transverse optical mode frequency to be equal to the largest transverse optical mode frequency of the III-V analogs. This leads to predicted cut-off wavelengths that agree with recent measurements to better than one micron. For example, for CdGeAs_2 we predicted a cut-off at $18.5 \mu\text{m}$ and measured $18 \mu\text{m}$ as shown in Fig. 2. The strength of the two phonon absorption in CdGeAs_2 is about 20 cm^{-1} at room temperature. There is also some weak three phonon absorption of approximately 0.3 cm^{-1} .

The chalcopyrites have only one independent nonlinear coefficient since $d_{14} = d_{36}$ according to the Kleinman symmetry condition.¹⁴ By applying the Miller's rule in Eq. (2.2), we estimate the magnitude using the measured Miller's constants for the III-V analogs. The agreement with the recent experimental values is within a factor of

TABLE I

OPTICAL PROPERTIES OF THE CHALCOPYRITES

	III-V analog	Melting point (°C)	Tetragonal compression $\tau = 2 - \frac{c}{a}$	$\sigma = 4x - 1$	Transmission range (μm)	Average index of refraction	Birefringence $n_e - n_o$	Nonlinear coefficient rel. GaAs
ZnSiP ₂	GaP + AlP	1370	0.066	0.076	0.54 - 10	3.1	0.06	0.83
ZnGeP ₂	GaP	1025	0.029	0.056	0.56 - 13	3.1	0.038	
ZnSnP ₂	GaP + InP	~ 950	0.000	- 0.044	0.86 - 14	2.85		
CdSiP ₂	InP + AlP	~ 1120	0.163	~ 0.172	0.56 - 10	(3.2)	- 0.05	1.21
CdGeP ₂	InP + GaP	~ 790	0.123	0.132	0.72 - 13	3.2	0.011	
CdSnP ₂	InP	~ 670	0.048	0.044	1.1 - (16)	3.3	0.04	
ZnSiAs ₂	GaAs + AlAs	~ 1080	0.061	~ 0.080	0.58 - 12	3.2	0.03	0.81
ZnGeAs ₂	GaAs	~ 880	0.034	0.056	1.5 - (18)	(3.3)		
ZnSnAs ₂	GaAs + InAs	~ 775	0.000	- 0.044	1.9 - (18)	(3.4)		
CdSiAs ₂	InAs + AlAs	~ 850	0.151	~ 0.164	0.80 - (12)	3.4		3.4
CdGeAs ₂	InAs + GaAs	670	0.112	0.144	2.3 - 18	3.6	0.095	
CdSnAs ₂	InAs	595	0.044	0.044	4.8 - (22)	3.8	0.16	

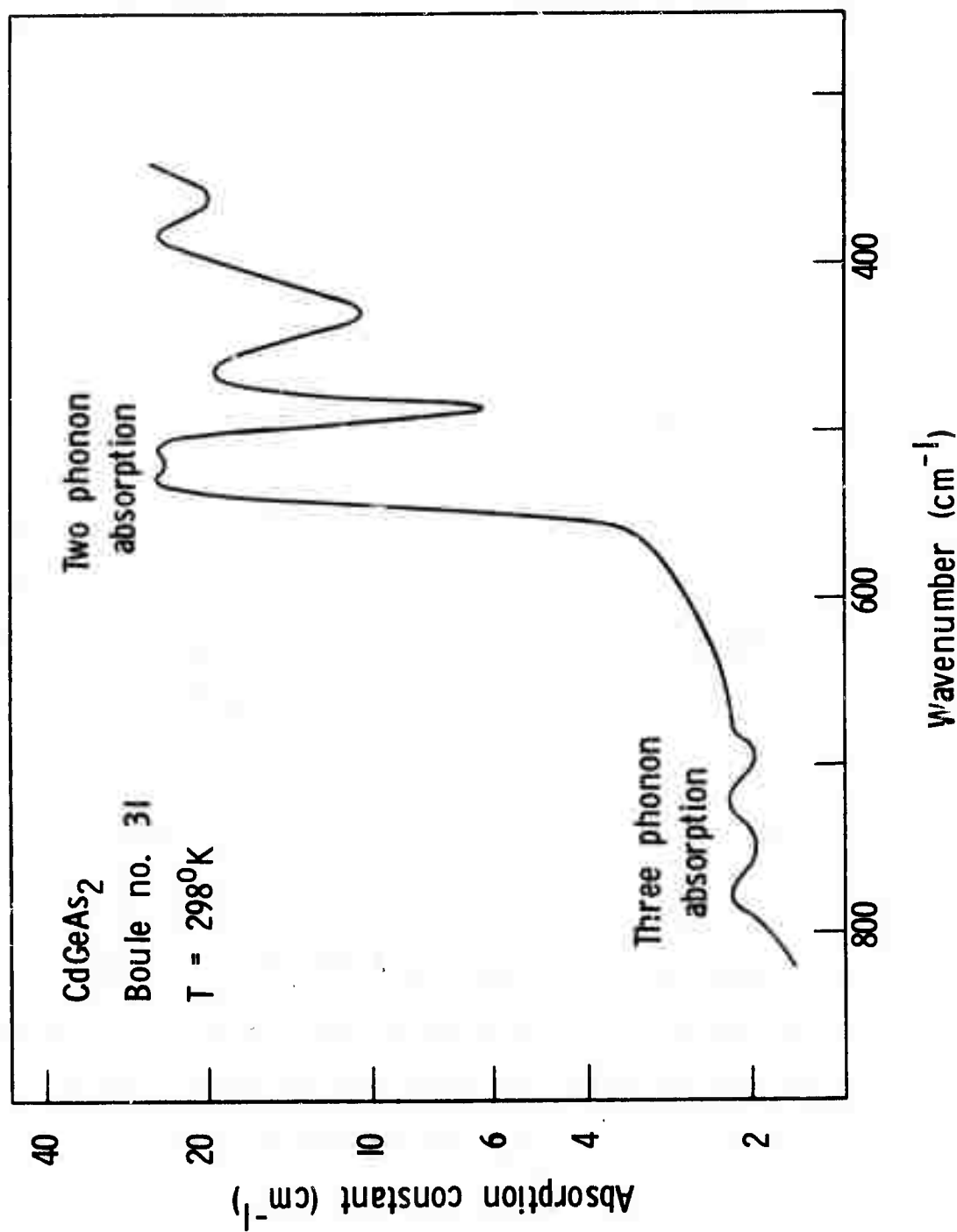


FIG. 2--Two and three phonon absorption in CdGeAs₂.

two. For compounds with unknown average index of refraction we use Eq. (2.10) to estimate the index.

The property most difficult to estimate is the birefringence. The c-axis compression of the III-V compounds results in a negative birefringence, so it was surprising that most of the chalcopyrites turned out to be positive birefringent. Initially, we assumed that the crystals with the largest tetragonal distortion had also the largest birefringence. We have shown later, however, that there is no such correlation. For example, both CdGeAs_2 and CdGeP_2 have large tetragonal distortion, but only CdGeAs_2 has large enough birefringence for phase-matching.

It is interesting to derive expressions for the indices of refraction and the birefringence for the chalcopyrites by assigning bond polarizabilities to the II-V and the III-V bonds. With a linear polarizability tensor $\bar{\alpha}$, we write the induced polarization of a bond as

$$\bar{p}(t) = \epsilon_0 \bar{\alpha} \cdot \bar{E}(t) \quad (2.8)$$

We assume uniaxial bond symmetry and write the transverse and the longitudinal linear bond polarizabilities as α_{\perp} and α_{\parallel} . We can then calculate the susceptibility tensor by summing over the thirty-two bonds within the chalcopyrite unit cell. Defining an average bond polarizability as $\alpha = \frac{1}{3}(2\alpha_{\perp} + \alpha_{\parallel})$ and the anisotropy as $\gamma = (\alpha_{\parallel} - \alpha_{\perp})$,

we follow Challa¹⁵ and obtain for the susceptibility tensor that

$$\bar{\chi} = \bar{\epsilon} - 1 = \frac{16}{V} (\alpha_{AC} + \alpha_{BC}) \mathbb{1} + \frac{16}{9V} \left[\gamma_{AC}(\tau + \sigma) + \gamma_{BC}(\tau - \sigma) \right] \begin{pmatrix} 1 & 0 & 0 \\ 0 & 1 & 0 \\ 0 & 0 & -2 \end{pmatrix}, \quad (2.9)$$

where AC and BC refer to the bonds to the largest and smallest cation and V is the unit cell volume. We assume the average bond polarizability is approximately the same as for the III-V analogs and calculate the average susceptibility for the chalcopyrites using the equation

$$\chi_{av} = \frac{V_a}{V} \chi_a + \frac{V_b}{V} \chi_b, \quad (2.10)$$

where V_a and V_b are the unit cell volumes and χ_a and χ_b are the measured susceptibilities of the III-V analogs.

For the relative birefringence we obtain from Eq. (2.9) that

$$\frac{\Delta n}{n} = \frac{n_e - n_o}{n} = \frac{\chi_e - \chi_o}{2(1 + \chi_{av})} \approx - \frac{\gamma_a(\tau + \sigma) + \gamma_b(\tau - \sigma)}{6(\alpha_a + \alpha_b)}, \quad (2.11)$$

since χ_{av} is always much greater than one. For the II-IV-V₂ compounds, τ and σ have about the same magnitude so we can approximate Eq. (2.11) by

$$\frac{\Delta n}{n} \approx - \frac{1}{6} \frac{\gamma_a}{\alpha_a + \alpha_b} (\tau + \sigma). \quad (2.12)$$

The maximum positive birefringence occurs when $\alpha_{\perp} \gg \alpha_{\parallel}$. This gives

$$\left(\frac{\Delta n}{n}\right)_{\max} = + \frac{1}{4} \frac{\tau + \sigma}{1 + \alpha_{\perp b} / \alpha_{\perp a}} . \quad (2.13)$$

According to Eq. (2.12) the birefringence depends mainly on the anisotropic polarizability of the AC bond. Consequently, since A is the cation with the largest radius, the birefringence of, for example, CdGeP_2 and CdSiP_2 should be determined mainly by the anisotropic polarizability of the CdP bond. However, it is not possible to estimate the birefringence of CdSiP_2 from the birefringence CdGeP_2 because the anisotropic polarizability of the CdP bond changes when silicon replaces germanium. Therefore, in practice the Eqs. (2.12) and (2.13) cannot be used to estimate the birefringence.

For reference, Table I gives a listing of the optical properties of the chalcopyrites. The numbers in parentheses have not been measured, but we believe they represent good estimates. The two most useful crystals for nonlinear optics will probably be CdGeAs_2 and ZnGeP_2 .

CHAPTER III
BANDSTRUCTURE OF THE CHALCOPYRITES
IN THE VICINITY OF $k = 0$

CdGeP_2 with a bandgap energy of 1.72 eV is expected to be the II-IV-V₂ chalcopyrite compound with the largest direct energy gap.¹⁶ All the chalcopyrites with smaller energy gaps, however, are direct bandgap material with the bandgap located at $k = 0$. Rowe and Shay¹⁷ discuss the splitting and symmetry of the valence and conduction bands, and they model the chalcopyrite structure as a strained version of the III-V sphalerite structure. This gives good agreement with the observed electroreflectance spectra. The S-like conduction band is singly degenerate (doubly counting spins). The triply degenerate P-like valence band (sixfold counting spins) is split into three sub-bands because of spin-orbit and crystal field interaction.

Knowledge of the splitting and the curvature of the valence and conduction bands near $k = 0$ is very important for the understanding of optical and electrical transport properties. From the curvature of the bands we determine the effective masses which allow us to calculate the intrinsic carrier density, the free electron absorption cross section, and the plasma frequency. From the plasma frequency we can determine how much the presence of free carriers perturb the indices of refraction. The components of the mobility and conductivity tensor are related to the anisotropy of the effective masses.

In p-type material there is optical absorption due to intraband transitions between the valence bands. Our band structure calculation allows us to estimate the magnitude of the absorption cross section. In Chapter V we also discuss third order nonlinear processes in the chalcopyrites. The largest contribution to the third order susceptibility tensor for III-V compounds with a free electron concentration of 10^{16} cm^{-3} is from the nonparabolicity of the conduction band near $k = 0$.^{18,19} Similar calculations are also possible for the chalcopyrites except they are more complicated, since the lack of cubic symmetry leads to much more complex bandstructure. It is interesting, however, that measuring the third order susceptibility tensor components provides a check on the bandstructure theory.

The bandstructure of the III-V compounds near the Brillouin zone center is very well described by a semi-empirical theory due to Kane.²⁰ Borshchevskii et al.³ adopt these results directly to the chalcopyrites to calculate the effective masses. This is not very satisfactory since there is a significant crystal field splitting in the chalcopyrites.²¹ We will therefore extend Kane's theory to the chalcopyrites and calculate the energy and wave functions to second order in k .

Including spin-orbit coupling, the Schrödinger equation for an electron in a periodic potential $V(\vec{r})$ is

$$\left[\frac{p^2}{2m} + V + \frac{\hbar}{4m^2 c^2} (\nabla \times \vec{p}) \cdot \vec{\sigma} \right] \psi_{\mathbf{k}} = E_{\mathbf{k}} \psi_{\mathbf{k}}, \quad (3.1)$$

where \bar{p} is the momentum operator and $\bar{\sigma}$ is the spin operator.

Introducing the Bloch-function $\psi_k = u_k e^{i\bar{k} \cdot \bar{r}}$, where u_k has the periodicity of the lattice, we obtain

$$\left[\frac{p^2}{2m} + V + \frac{\hbar}{m} \bar{k} \cdot \bar{p} + \frac{\hbar}{4m^2 c^2} (\nabla \times \bar{p}) \cdot \bar{\sigma} + \frac{\hbar^2}{4m^2 c^2} (\nabla \times \bar{k}) \cdot \bar{\sigma} \right] u_k = \left(E_k - \frac{\hbar^2 k^2}{2m} \right) u_k \quad (3.2)$$

We neglect the term $(\hbar^2/4m^2 c^2)(\nabla \times \bar{k}) \cdot \bar{\sigma} u_k$, since it is very small according to Kane, because most of the spin-orbit interaction occurs in the interior of the atom where the atomic momentum \bar{p} is much larger than the crystal momentum $\hbar \bar{k}$. We write the potential as $V = V_0 + V_{cr}$. Here V_0 has cubic symmetry and V_{cr} is the potential caused by the tetragonal distortion. We let

$$H_0 = \frac{p^2}{2m} + V_0 \quad (3.3)$$

be the Hamiltonian for the unperturbed problem and treat

$$H' = V_{cr} + \frac{\hbar}{m} \bar{k} \cdot \bar{p} + \frac{\hbar}{4m^2 c^2} (\nabla_0 \times \bar{p}) \cdot \bar{\sigma} \quad (3.4)$$

as the perturbation where the tetragonal potential is neglected in the spin-orbit coupling term. As basis functions we take the wavefunctions for the valence and conduction band. Restriction to these eight wave functions means that the influence of the higher

and lower lying bands are considered small. This approximation works best when the energy separation to the other bands at $k = 0$ is much larger than the bandgap energy. We follow Kane and use the basis functions:

$$|1S\downarrow\rangle, |2^{-1/2}(X - iY)\uparrow\rangle, |Z\downarrow\rangle, |2^{-1/2}(X + iY)\uparrow\rangle,$$

$$|1S\uparrow\rangle, |2^{1/2}(X + iY)\downarrow\rangle, |Z\uparrow\rangle, |2^{-1/2}(X - iY)\downarrow\rangle.$$

The first four functions are respectively degenerate with the last four. The symbols \uparrow and \downarrow indicate spin up and down referred to the z-axis. S refers to the conduction band wave functions. They transform as atomic s-functions under the symmetry operations of the tetrahedral group. Similarly X, Y, and Z refer to the valence band wave functions, and they have the symmetry properties of the atomic p-functions x, y, and z under the tetrahedral group operations.

With these basis functions, it follows that the 8×8 Hamiltonian matrix can be written

$$H = \begin{bmatrix} H_1 & H_2 \\ H_2^+ & H_1 \end{bmatrix}, \quad (3.5)$$

where

$$H_1 = \begin{bmatrix} E_s & 0 & k_z P & 0 \\ 0 & E_p + \frac{\delta}{3} - \frac{\Delta}{3} & \frac{\bar{2}^{1/2}}{3} \Delta & 0 \\ k_z P & \frac{\bar{2}^{1/2}}{3} & E_p - \frac{2}{3} \delta & 0 \\ 0 & 0 & 0 & E_p + \frac{\delta}{3} + \frac{\Delta}{3} \end{bmatrix} \quad (3.6)$$

and

$$H_2 = \begin{bmatrix} 0 & -\bar{2}^{1/2}(k_x + ik_y)P & 0 & \bar{2}^{1/2}(k_x - ik_y)P \\ \bar{2}^{1/2}(k_x + ik_y)P & 0 & 0 & 0 \\ 0 & 0 & 0 & 0 \\ \bar{2}^{1/2}(k_x - ik_y)P & 0 & 0 & 0 \end{bmatrix} \quad (3.7)$$

Here E_s and E_p are the eigenvalues of the unperturbed Hamiltonian, referring to respectively the two-fold degenerate conduction band and the six-fold degenerate valence band. We further have defined the quantities

$$P = -i \frac{\hbar}{m} \langle S | p_z | Z \rangle \quad (3.8)$$

with

$$\langle S | p_z | Z \rangle = \langle S | p_x | X \rangle = \langle S | p_y | Y \rangle ;$$

$$\Delta = \frac{3\hbar^2}{4m^2 c^2} \langle X | \frac{\partial V_0}{\partial x} p_y - \frac{\partial V_0}{\partial y} p_x | Y \rangle \quad (3.9)$$

with

$$\begin{aligned} \langle X | \frac{\partial V_0}{\partial x} p_y - \frac{\partial V_0}{\partial y} p_x | Y \rangle &= \langle X | \frac{\partial V_0}{\partial x} p_z - \frac{\partial V_0}{\partial z} p_x | Z \rangle \\ &= \langle Y | \frac{\partial V_0}{\partial y} p_z - \frac{\partial V_0}{\partial z} p_y | Z \rangle ; \end{aligned}$$

and

$$\left. \begin{aligned} \langle X | V_{cr} | X \rangle &= \langle S | V_{cr} | S \rangle + \frac{\delta}{3} \\ \langle Z | V_{cr} | Z \rangle &= \langle S | V_{cr} | S \rangle - \frac{2\delta}{3} \end{aligned} \right\} \quad (3.10)$$

We have not included the term $\langle S | V_{cr} | S \rangle$ in Eq. (3.6) since it only shifts the eigenvalues by a constant. To determine the level splitting near $k = 0$ to first order in H' because of the spin-orbit coupling Δ and the crystal field splitting δ , we diagonalize the matrix in Eq. (3.5). We find that the conduction band remains two-fold degenerate while the valence band splits into three doubly degenerate levels. The four doubly degenerate eigenvalues are determined by the

secular equation:

$$E \left\{ (E - E_s) \left[E^2 + (\delta + \Delta)E + \frac{2\Delta\delta}{3} \right] - (k_z P)^2 \left(E + \frac{2\Delta}{3} \right) \right\} - (k_x^2 + k_y^2) P^2 \left[E^2 + \left(\frac{2\Delta}{3} + \delta \right) E + \frac{8\Delta}{3} \right] = 0, \quad (3.11)$$

where $E = E_k - (\hbar^2 k^2 / 2m)$. We have fixed the zero on the energy scale in Eq. (3.11), by letting $E_p + \delta/3 + \Delta/3 = 0$. At $k = 0$ the eigenvalues are E_s , E_1 , 0, and E_2 with

$$E_{1,2} = -\frac{1}{2}(\Delta + \delta) \pm \frac{1}{2} \sqrt{(\delta + \Delta)^2 - \frac{8\Delta\delta}{3}}. \quad (3.12)$$

In the chalcopyrites we have $\Delta > 0$ and $\delta < 0$ ¹⁷ which means that $E_1 > 0$ and $E_2 < 0$. E_1 is therefore the energy of the highest lying valence band and the bandgap energy is $E_G = E_s - E_1$. We use this together with Eq. (3.12) to rewrite Eq. (3.11). We find that

$$E(E - E_1 - E_G)(E - E_1)(E - E_2) = (k_z P)^2 E \left(E + \frac{2\Delta}{3} \right) + (k_x^2 + k_y^2) P^2 \left[(E - E_1)(E - E_2) - \frac{\Delta}{3}(E + \delta) \right]. \quad (3.13)$$

For small k^2 , the solutions of Eq. (3.13) give parabolic energy bands. Including the $(\hbar^2 k^2 / 2m)$ term from Eq. (3.2), we obtain

to second order in k that the energies of the conduction and valence bands are

$$\begin{aligned}
 E_c &= E_G + E_1 + \frac{\hbar^2 k^2}{2m} + \frac{(k_z P)^2 (E_G + E_1 + 2\Delta/3)}{E_G (E_G + E_1 - E_2)} \\
 &\quad + \frac{(k_x^2 + k_y^2) P^2}{E_G + E_1} \left[1 - \frac{(\Delta/3) (E_G + E_1 + \delta)}{E_G (E_G + E_1 - E_2)} \right] \\
 E_{v_1} &= E_1 + \frac{\hbar^2 k^2}{2m} - \frac{(k_z P)^2 (E_1 + 2\Delta/3)}{E_G (E_1 - E_2)} + \frac{(k_x^2 + k_y^2) P^2 (E_1 + \delta) \Delta}{3E_1 E_G (E_1 - E_2)} \\
 E_{v_2} &= \frac{\hbar^2 k^2}{2m} - \frac{1}{2} \frac{(k_x^2 + k_y^2) P^2}{E_G + E_1} \\
 E_{v_3} &= E_2 + \frac{\hbar^2 k^2}{2m} + \frac{(k_z P)^2 (E_2 + 2\Delta/3)}{(E_1 - E_2) (E_G + E_1 - E_2)} - \frac{(k_x^2 + k_y^2) P^2 (E_2 + \delta) \Delta}{3E_2 (E_G + E_1 - E_2) (E_1 - E_2)}
 \end{aligned} \tag{3.14}$$

The above equations give the energy splittings and the effective masses of the four bands excluding the effect of higher lying bands. It is worth noting that the expressions for E_{v_1} and E_{v_2} are not valid in the limit $\delta \rightarrow 0$. We now proceed to calculate the wave functions. The lattice periodic functions $|u_m\rangle$ are given by a linear combination of the eight basis functions $|n\rangle$. We have

$$|u_m\rangle = \sum_n a_{mn} |n\rangle, \tag{3.15}$$

and we determine the coefficients a_{mn} by solving the eight homogeneous equations

$$\sum_n a_{mn} (H_{sn} - E_m \delta_{sn}) = 0 ; \quad s = 1 \text{ to } 8 \quad (3.16)$$

for each eigenvalue E_m of the Hamiltonian matrix H_{sn} in Eq. (3.5).

We then obtain Eqs. (3.17) and (3.18)

$$\begin{aligned} |u_c^A\rangle = & \left\{ |1s\rangle + \frac{1}{E_G(E_G + E_1 - E_2)} \left(k_z P \left[\frac{2^{\frac{1}{2}}}{3} \Delta |2^{-\frac{1}{2}}(X - iY)\rangle + \left(E_G + E_1 + \frac{2\Delta}{3} \right) |Z\rangle \right] \right. \right. \\ & - 2^{-\frac{1}{2}}(k_x - ik_y) P \left[\left(E_G + E_1 + \delta + \frac{\Delta}{3} \right) |2^{-\frac{1}{2}}(X + iY)\rangle + \frac{2^{\frac{1}{2}}}{3} \Delta |Z\rangle \right] \Bigg) \\ & \left. + \frac{2^{-\frac{1}{2}}(k_x + ik_y) P}{E_G + E_1} |2^{-\frac{1}{2}}(X - iY)\rangle \right\} \quad (3.17) \end{aligned}$$

$$\begin{aligned} |u_c^B\rangle = & \left\{ |1s\rangle + \frac{1}{E_G(E_G + E_1 - E_2)} \left(k_z P \left[\frac{2^{\frac{1}{2}}}{3} \Delta |2^{-\frac{1}{2}}(X + iY)\rangle + \left(E_G + E_1 + \frac{2\Delta}{3} \right) |Z\rangle \right] \right. \right. \\ & + 2^{-\frac{1}{2}}(k_x + ik_y) P \left[\left(E_G + E_1 + \delta + \frac{\Delta}{3} \right) |2^{-\frac{1}{2}}(X - iY)\rangle + \frac{2^{\frac{1}{2}}}{3} \Delta |Z\rangle \right] \Bigg) \\ & \left. + \frac{2^{-\frac{1}{2}}(k_x - ik_y) P}{E_G + E_1} |2^{-\frac{1}{2}}(X + iY)\rangle \right\} \end{aligned}$$

$$\begin{aligned}
|u_{v_1}^A\rangle &= \left[1 + \frac{1}{2} \left(\frac{2\Delta}{2\Delta + 3E_1} \right)^2 \right]^{-\frac{1}{2}} \left\{ \frac{(2^{\frac{1}{2}}/3)\Delta}{E_1 + (2\Delta/3)} |2^{-\frac{1}{2}}(X - iY)\rangle + |Z\rangle \right. \\
&\quad \left. - \frac{k_z P}{E_0} |1s\rangle - \frac{(k_x - ik_y)P\Delta}{3E_0[E_1 + (2\Delta/3)]} |1s\rangle \right\} \\
|u_{v_1}^B\rangle &= \left[1 + \frac{1}{2} \left(\frac{2\Delta}{2\Delta + 3E_1} \right)^2 \right]^{-\frac{1}{2}} \left\{ \frac{(2^{\frac{1}{2}}/3)\Delta}{E_1 + (2\Delta/3)} |2^{-\frac{1}{2}}(X + iY)\rangle + |Z\rangle \right. \\
&\quad \left. - \frac{k_z P}{E_0} |1s\rangle + \frac{(k_x + ik_y)P\Delta}{3E_0[E_1 + (2\Delta/3)]} |1s\rangle \right\} \\
|u_{v_2}^A\rangle &= \left\{ |2^{-\frac{1}{2}}(X + iY)\rangle - \frac{2^{-\frac{1}{2}}(k_x + ik_y)P}{E_0 + E_1} |1s\rangle \right\} \\
|u_{v_2}^B\rangle &= \left\{ |2^{-\frac{1}{2}}(X - iY)\rangle - \frac{2^{-\frac{1}{2}}(k_x - ik_y)P}{E_0 + E_1} |1s\rangle \right\} \\
|u_{v_3}^A\rangle &= \left[1 + \frac{1}{2} \left(\frac{2\Delta}{2\Delta + 3E_2} \right)^2 \right]^{-\frac{1}{2}} \left\{ \frac{(2^{\frac{1}{2}}/3)\Delta}{E_2 + (2\Delta/3)} |2^{-\frac{1}{2}}(X - iY)\rangle + |Z\rangle \right. \\
&\quad \left. - \frac{k_z P}{E_0 + E_1 - E_2} |1s\rangle - \frac{(k_x - ik_y)P\Delta}{3(E_0 + E_1 - E_2)[E_2 + (2\Delta/3)]} |1s\rangle \right\} \\
|u_{v_3}^B\rangle &= \left[1 + \frac{1}{2} \left(\frac{2\Delta}{2\Delta + 3E_2} \right)^2 \right]^{-\frac{1}{2}} \left\{ \frac{(2^{\frac{1}{2}}/3)\Delta}{E_2 + (2\Delta/3)} |2^{-\frac{1}{2}}(X + iY)\rangle + |Z\rangle \right. \\
&\quad \left. - \frac{k_z P}{E_0 + E_1 - E_2} |1s\rangle + \frac{(k_x + ik_y)P\Delta}{3(E_0 + E_1 - E_2)[E_2 + (2\Delta/3)]} |1s\rangle \right\}
\end{aligned} \tag{3.18}$$

In Eqs. (3.17) and (3.18) A and B distinguish between the two wave functions of each doubly degenerate band. The Eqs. (3.14), (3.17), and (3.18) are the main results of this chapter. With these equations we can calculate energy splittings, effective masses, and optical transition probabilities between the bands. The equations depend only on the following four parameters: the bandgap energy E_G , the spin-orbit splitting energy Δ , the crystal field splitting parameter δ , and finally the matrix element P . For the bandgap energy we use the measured value. The spin-orbit coupling and crystal field splitting energies have been measured for four of the II-IV-V₂ compounds: CdGeP₂, CdSnP₂, ZnSiAs₂, and CdSiAs₂.¹⁶ For the other chalcopyrites we estimate the spin-orbit coupling from the III-V compounds by averaging the experimental values for the III-V analogs.²² For the crystal field splitting we use the results of a pseudopotential calculation,²¹ noting that with our definition of the crystal field splitting parameter it assumes negative values in the chalcopyrites.¹⁷ It is also possible to estimate the crystal field splitting by considering the chalcopyrites as stressed versions of the III-V compounds as suggested by Shay et al.^{17,23} A comparison with Pollak et al.²⁴ yields

$$\delta = -\frac{3}{2} \delta E_{001} = -3b(\epsilon_{zz} - \epsilon_{xx}) = \frac{3}{2} b\tau, \quad (3.19)$$

where b is the deformation potential of the III-V analogs for stress in the [001] direction. For GaAs $b = -1.75$ eV.²⁵ Since we do not

know b for InAs, we use this value to estimate $\delta = -0.29$ eV for CdGeAs₂ which is close to -0.25 eV predicted by the pseudopotential calculation.

The matrix element P is nearly constant for all the III-V compounds that can be described by Kane's theory.²⁶ Within 20% we have

$$P^2 = \frac{\hbar^2}{2m} \times 20 \text{ eV} \quad (3.20)$$

for the III-V compounds, and we assume this value for the chalcopyrites.

Close to $k = 0$ the energy bands are of the form

$$E = E_0 \pm \frac{\hbar^2}{2} \left[\frac{k_x^2 + k_y^2}{m_T} + \frac{k_z^2}{m_L} \right], \quad (3.21)$$

with the plus and minus sign referring to respectively the conduction and valence bands. In Eq. (3.21) m_T and m_L define the transverse and the longitudinal effective masses. We can use these to define a density of states effective mass m_{de}

$$m_{de}^3 = m_L m_T^2, \quad (3.22)$$

and a conductivity effective mass m_σ

$$\frac{1}{m_\sigma} = \frac{1}{3} \left(\frac{1}{m_L} + \frac{2}{m_T} \right), \quad (3.23)$$

(cf. reference 27). Table II gives the calculated effective masses for CdGeAs₂ and CdGeP₂ together with the values for E_G , Δ and δ

TABLE II

CALCULATED VALENCE BAND SPLITTING ENERGIES AND EFFECTIVE
MASSES FOR THE CONDUCTION AND VALENCE BANDS

	CdGeAs ₂				CdGeP ₂			
E _G	0.53				1.72			
Δ	0.38				0.11			
δ	- 0.25				- 0.20			
E ₁	0.20				0.17			
E ₂	- 0.32				- 0.08			
	m _T	m _L	m _{de}	m _σ	m _T	m _L	m _{de}	m _σ
c	0.039	0.028	0.035	0.034	0.088	0.079	0.085	0.085
v ₁	0.77	0.031	0.26	0.087	—	0.097		
v ₂	0.079	—			0.23	—		
v ₃	0.14	0.69	0.24	0.19	0.24	—		

All energies are in eV and the effective masses are in units of the free electron mass.

used in the calculation. The table also lists the splitting energies E_1 and E_2 of the valence band. We have assumed direct bandgaps, setting E_G equal to the measured bandgap energy. There is, however, some uncertainty concerning CdGeAs_2 . Early reports of a direct bandgap²⁸ have been questioned recently,²⁹ although the fact that both of the III-V analogs GaAs and InAs have direct bandgaps tends to support the notion of a direct bandgap. With this qualification in mind, Fig. 3 shows the expected bandstructure of CdGeAs_2 near $k = 0$. The highest valence band has a smaller longitudinal, but a larger transverse effective mass than the v_2 -band. A few of the effective masses of the valence bands are not listed in Table II. These can only be determined accurately by considering the effect of higher bands since they receive very little contribution from the conduction band interaction. No measured effective masses have been reported for CdGeP_2 . In CdGeAs_2 , however, infrared plasma reflection³⁰ and thermoelectric power measurements^{28,31} have been used to determine the electron mass. The effective mass depends on the carrier concentration. Extrapolation to small carrier concentrations results in an effective mass of 0.02 to 0.03 times the free electron mass. This is in reasonably good agreement with the calculated effective mass of 0.035 in Table II. There is only one reported measurement of the effective hole mass in CdGeAs_2 .³¹ The mass was deduced from measurements of the thermoelectric power. This gave a density of state effective mass of 0.3 which agrees surprisingly well with our

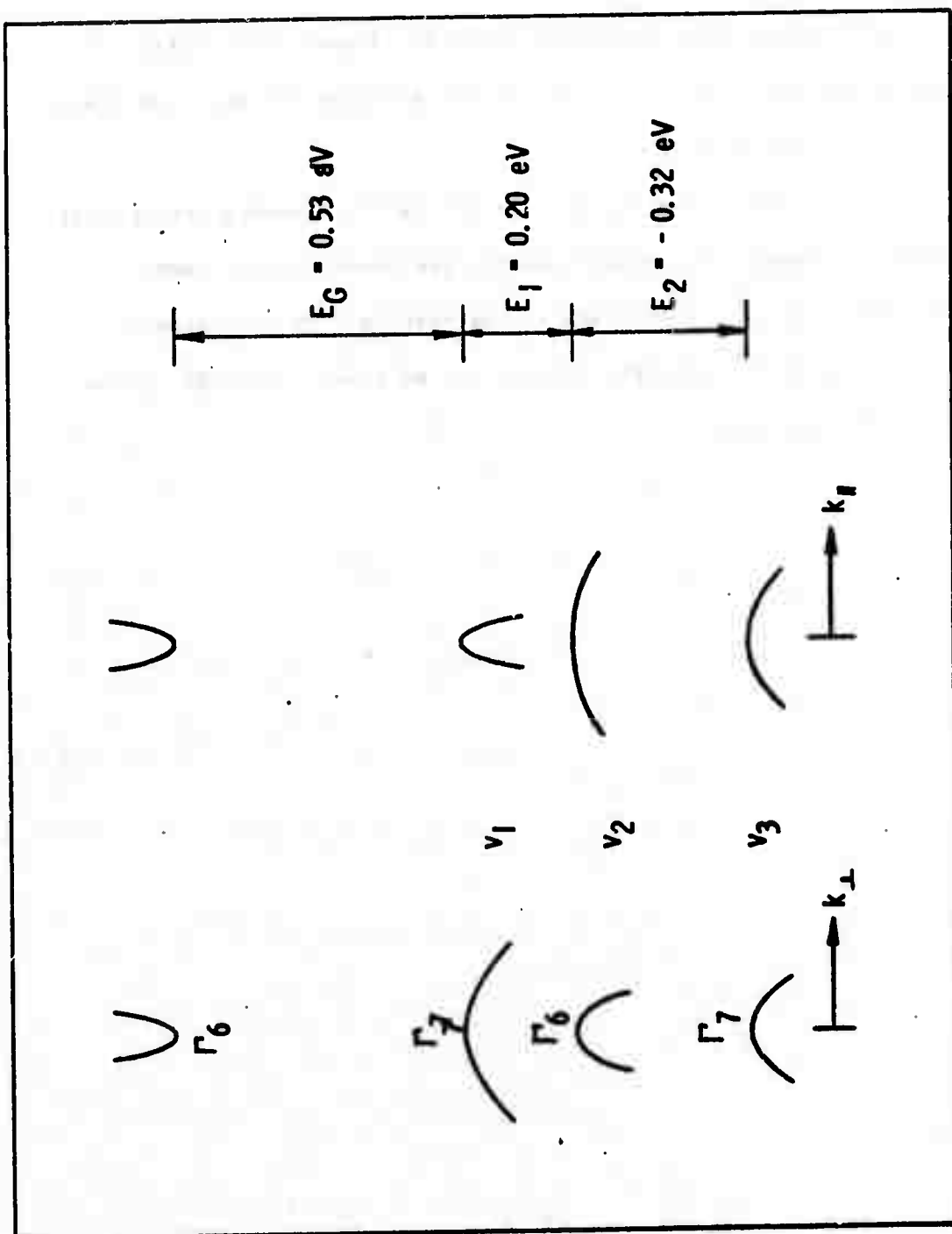


FIG. 3--CdGeAs₂ band structure near $k = 0$

calculated value of 0.26. We therefore conclude that the generalized Kane model that we have described, gives an adequate description of the bandstructure near $k \approx 0$ in CdGeAs_2 and probably works well also for the other chalcopyrites.

Finally in this chapter, we list the matrix elements for optical transitions between the highest and the two lower valence bands. In Chapter VI we will refer back to the results when we estimate the magnitude of the absorption in p-type material. (See Eq. (3.24) on the following page).

$$\langle u_{v_1}^A | \hat{e} \cdot \vec{p} | u_{v_2}^A \rangle = -c_{v_1} 2^{-1/2} (k_x + ik_y) \frac{P_m^2}{\hbar} \frac{\Delta}{3(E_1 + 2\Delta/3)} \frac{2E_G + E_1}{E_G(E_G + E_1)} (e_x + ie_y)$$

$$\langle u_{v_1}^A | \hat{e} \cdot \vec{p} | u_{v_2}^B \rangle = -c_{v_1} 2^{-1/2} \frac{P_m^2}{\hbar} \left\{ \frac{k_x}{E_G} (e_x - ie_y) + \frac{k_x - ik_y}{E_G + E_1} e_z \right\}$$

$$\begin{aligned} \langle u_{v_1}^A | \hat{e} \cdot \vec{p} | u_{v_3}^A \rangle = & -c_{v_1} c_{v_3} \frac{P_m^2}{\hbar} \left\{ \left(\frac{1}{E_G} + \frac{1}{E_G + E_1 - E_2} \right) k_z e_z \right. \\ & + \frac{\Delta^2}{9(E_1 + 2\Delta/3)(E_2 + 2\Delta/3)} \left[\frac{k_x + ik_y}{E_G} (e_x - ie_y) \right. \\ & \left. \left. + \frac{k_x - ik_y}{E_G + E_1 - E_2} (e_x + ie_y) \right] \right\} \end{aligned}$$

$$\begin{aligned} \langle u_{v_1}^A | \hat{e} \cdot \vec{p} | u_{v_3}^B \rangle = & -c_{v_1} c_{v_3} \frac{\Delta P_m^2}{3\hbar} \left\{ \left[\frac{1}{E_G(E_1 + 2\Delta/3)} \right. \right. \\ & \left. \left. - \frac{1}{(E_G + E_1 - E_2)(E_2 + 2\Delta/3)} \right] (k_y + ik_x) e_z \right. \\ & \left. + \left[\frac{1}{(E_1 + 2\Delta/3)(E_G + E_1 - E_2)} - \frac{1}{(E_2 + 2\Delta/3)E_G} \right] k_z (e_x + ie_y) \right\} \end{aligned}$$

with

$$c_{v_1} = \left[1 + \frac{1}{2} \left(\frac{2\Delta}{2\Delta + 3E_1} \right)^2 \right]^{-1/2}$$

$$c_{v_3} = \left[1 + \frac{1}{2} \left(\frac{2\Delta}{2\Delta + 3E_2} \right)^2 \right]^{-1/2}$$

(3.24)

CHAPTER IV

ELECTRIC PROPERTIES AND LINEAR EXPANSION COEFFICIENT OF CdGeAs_2

Several absorption mechanisms in the chalcopyrites are related to the semiconductor properties. Therefore knowledge of the electric transport properties is necessary for a full evaluation of the material. It is well known that controlled doping may improve the optical quality of semiconductors. As an example, doping GaAs by chromium introduces deep acceptor levels that remove all the free electrons. This results in high resistivity material of good optical quality. Another example is CdSe where Se compensation reduces the carrier concentration. Besides causing scattering leading to absorption, the presence of free carriers perturbs the indices of refraction and thereby the phasematching angle for nonlinear optical interactions. An additional absorption mechanism exists in p-type material due to intraband transitions between the split valence bands. This absorption mechanism has a magnitude proportional to the free hole concentration. Another common cause of optical absorption in semiconductors is impurity absorption. From the temperature dependence of the Hall coefficient we can derive information about the position and concentration of the impurity levels, and by combining the Hall coefficient with the measured conductivity we can calculate the carrier mobility. The mobility is sensitive to the general crystal quality and increases with a smaller number of crystal imperfections.

In this chapter we discuss the electrical transport equations necessary to interpret the experimental results and then present the results for p-type CdGeAs_2 . We will also discuss the measurements of the linear thermal expansion coefficient for CdGeAs_2 . The expansion coefficient is strongly anisotropic and explains at least partially the crystal cracking during growth.

A. ELECTRIC TRANSPORT PROPERTIES

1. Theory

Introducing an electron mobility μ_c and a hole mobility μ_v , we have that the electric conductivity is given by

$$\sigma = e(n\mu_c + p\mu_v) \quad , \quad (4.1)$$

when there are n electrons in the conduction band and p holes in the valence band. The mobility depends on the collision time of the carriers and the effective mass. For holes we have

$$\mu_v = \frac{e\langle\tau\rangle}{m_v} \quad , \quad (4.2)$$

and a similar expression holds for the electrons. $\langle\tau\rangle$ is the collision time averaged over the carrier velocity since τ in general is velocity dependent.

In the case of an anisotropic valence or conduction band, σ is a tensor. From band structure calculations near the Brillouin zone center we have shown that the chalcopyrites have a nearly

isotropic conduction band, but that the valence band is strongly anisotropic. It is convenient to define a longitudinal and a transverse conductivity for conduction parallel and perpendicular to the c-axis direction. For p-type material we have according to Eqs. (4.1) and (4.2) that

$$\frac{\sigma_L}{\sigma_T} = \frac{\mu_{v1,L}}{\mu_{v1,T}} = \frac{m_{v1,T}}{m_{v1,L}}, \quad (4.3)$$

where v_1 refers to the top valence band. Using the effective masses in Table II, we obtain $\sigma_L/\sigma_T = 25$ for CdGeAs_2 . The ratio between the electron and hole mobility depends on which scattering mechanism limits the collision time. The average collision time is in general different for electrons and holes. Pure acoustic scattering is most important at high temperatures due to the $T^{-3/2}$ temperature dependence. In that case the ratio between the longitudinal components of the mobility tensor is²⁷

$$\frac{\mu_{c,L}}{\mu_{v1,L}} = \frac{m_{v1,L}}{m_{c,L}} \left(\frac{m_{v1,de}}{m_{c,de}} \right)^{\frac{3}{2}}, \quad (4.4)$$

and we obtain a similar expression for the transverse components. The subscript de in Eq. (4.4) refers to the density of states effective mass. Applying Eq. (4.4) to CdGeAs_2 we obtain $\mu_{c,L}/\mu_{v1,L} = 22$ and $\mu_{c,T}/\mu_{v1,T} = 400$.

By a slight extension of the results in reference 27, we obtain expressions for the Hall constant R in crystals such as CdGeAs_2 with spheroidal constant energy surfaces and a direct bandgap at $k = 0$. For the magnetic field applied along the c -axis we find

$$R_{B\parallel C} = \frac{E_y}{j_x B_z} = \frac{r}{|e|} \frac{p\mu_{v,T}^2 - n\mu_{c,T}^2}{(p\mu_{v,T} + n\mu_{c,T})^2}, \quad (4.5)$$

and for the magnetic field perpendicular to the c -axis we have

$$R_{B\perp C} = \frac{E_z}{j_y B_x} = \frac{r}{|e|} \frac{p\mu_{v,T}\mu_{v,L} - n\mu_{c,T}\mu_{c,L}}{(p\mu_{v,T} + n\mu_{c,T})(p\mu_{v,L} + n\mu_{c,L})}. \quad (4.6)$$

In the above equations $r = \langle \tau^2 \rangle / \langle \tau \rangle^2$ is a constant close to unity, i.e. $r = 1.18$ for pure acoustic scattering and $r = 1.93$ for ionized impurity scattering.²⁷ With only one type of carrier the equations simplify. For p -type material we have

$$R_{B\parallel C} = R_{B\perp C} = \frac{r}{|e|p}. \quad (4.7)$$

and in this case the Hall constant is a direct measure of the carrier concentration.

In intrinsic semiconductors the number of holes equals the number of electrons. With the definitions

$$N_c = 2 \left(\frac{2\pi k T m_{c,de}}{h^2} \right)^{\frac{3}{2}} \quad (4.8)$$

and

$$N_v = 2 \left(\frac{2\pi k T m_{c,de}}{h^2} \right)^{\frac{3}{2}} \quad (4.9)$$

we calculate the intrinsic carrier concentration n_i by the equation

$$n_i^2 = N_c N_v \exp \left(- \frac{E_G}{kT} \right) . \quad (4.10)$$

Using the effective masses $m_{c,de} = 0.035 m$ and $m_{v,de} = 0.26 m$, we obtain for CdGeAs₂ that

$$n_i = 1.42 \times 10^{14} T^{3/2} \exp \left(- \frac{3000}{T} \right) ; \left(\frac{1}{\text{cm}^3} \right) . \quad (4.11)$$

Figure 4 shows the temperature dependence of the intrinsic carrier concentration. At 300°K we have $N_c = 1.64 \times 10^{17} \text{ cm}^{-3}$ and $N_{v1} = 3.32 \times 10^{18} \text{ cm}^{-3}$.

For extrinsic semiconductors assuming nondegenerate bands, the product np of the electron and hole concentration is constant independent of the impurity concentration and it is given by

$$np = n_i^2 . \quad (4.12)$$

The semiconductor is nondegenerate when the Fermi level is in the forbidden energy gap and is separated from the valence and the conduction band by an energy of more than kT . For p-type material this condition implies that $p/N_v < 1/e$ with $e = 2.718$. This condition can be rewritten such that for a carrier concentration p the semiconductor

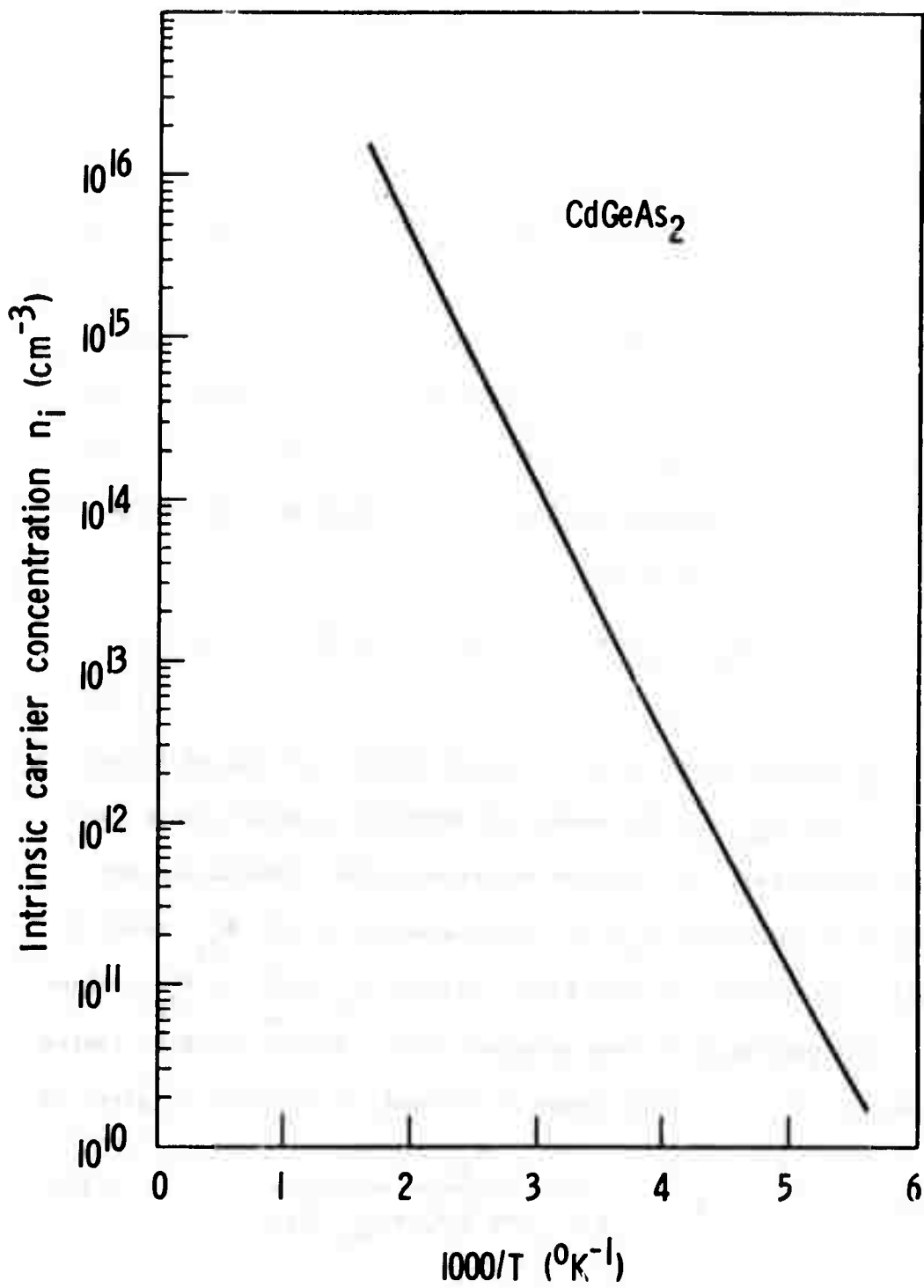


FIG. 4--Calculated intrinsic carrier concentration in CdGeAs_2 .

is nondegenerate at temperatures larger than the degeneracy temperature T_D defined by the equation

$$T_D = 1.23 \frac{h^2}{2\pi k m_{v,de}} p^{2/3} . \quad (4.13)$$

For a hole concentration of 10^{16} cm^{-3} in CdGeAs_2 the degeneracy temperature is as low as 12°K .

Finally in this section, we discuss the temperature variation of the carrier concentration in a material with N_d donors and two acceptor levels of concentration N_{a1} and N_{a2} respectively. The results apply to the measured p-type CdGeAs_2 samples. The charge balance leads to the equation

$$n + (N_{a1} - n_{a1}) + (N_{a2} - n_{a2}) = p + (N_d - n_d) , \quad (4.14)$$

where n_d is the number of filled donor levels (un-ionized donors) and n_{a1} and n_{a2} are the number of unfilled acceptor levels (un-ionized acceptors). We consider p-type material. The donors are then ionized such that $n_d = 0$. Furthermore, we let N_{a1} refer to a shallow acceptor level also fully ionized ($n_{a1} = 0$). N_{a2} refers to a deeper partially ionized acceptor level. For an acceptor ionization energy of ϵ_{a2} , the number of un-ionized acceptors is given by

$$n_{a2} = \frac{N_{a2}}{1 + \frac{1}{2} \exp [(E_F - \epsilon_{a2})/kT]} . \quad (4.15)$$

Here the Fermi energy is measured from the top of the valence band and the factor of two is the spin degeneracy. For simplicity we also neglect n in Eq. (4.14). This is allowed as long as the hole concentration is much larger than the intrinsic carrier density. For a nondegenerate semiconductor, the concentration of holes in the valence band is given by

$$p = N_v e^{-E_F/kT}, \quad (4.16)$$

which substituted into Eq. (4.15) yields

$$n_{a2} = \frac{N_{a2}}{1 + \frac{1}{2} (N_v/p) \exp(-\epsilon_{a2}/kT)}. \quad (4.17)$$

This eliminates the Fermi energy from Eq. (4.14) and we can solve for the hole concentration. We obtain

$$p = \frac{1}{2} (N_{a1} - N_d - \frac{1}{2} N_v e^{-\epsilon_{a2}/kT}) + \frac{1}{2} \left[(N_{a1} - N_d - \frac{1}{2} N_v e^{-\epsilon_{a2}/kT})^2 + 2(N_{a1} + N_{a2} - N_d) N_v e^{-\epsilon_{a2}/kT} \right]^{\frac{1}{2}} \quad (4.18)$$

with the asymptotic solutions $p = N_{a1} - N_d$ at low temperatures and $p = N_{a1} + N_{a2} - N_d$ at high temperatures. The donors partially compensate the hole concentration. At intermediate temperatures there is an approximate solution provided the condition

$$N_{a1} - N_d \ll p \ll N_{a1} + N_{a2} - N_d \quad (4.19)$$

can be satisfied which is only possible when $N_{a2} \gg N_{a1} - N_d$. With Eq. (4.19) satisfied, the approximate carrier concentration is given by

$$p \approx \sqrt{\frac{1}{2} N_{a2} N_v} e^{-\epsilon_{a2}/2kT} \quad (4.20)$$

2. Experiment

We have measured the resistivity and Hall constant between 77°K and 400°K for p-type CdGeAs₂. The samples came from boules grown from stoichiometric melt. For most samples we used the van der Pauw method.^{32,33} We did not orient the samples. They consisted of one or a few crystallites and the sample diameter to thickness ratio was about 10. It would have been desirable to use oriented rectangular bar shaped samples since this would have allowed us to measure the individual components of the conductivity tensor. However, due to the extensive cracking it was not possible to obtain sufficiently large oriented single crystal samples. We used indium to form ohmic contacts. The contacts worked well down to liquid nitrogen. Small balls of indium were squeezed onto the sample by a teflon coated tweezer and then alloyed in an H₂ atmosphere for 5 to 10 minutes at 350°C.

Figure 5 shows the temperature dependence of the Hall constant. We used a current of 0.5 mA and a magnetic field of 2000 Gauss. This gave a Hall voltage of about 100 μV. The Hall constant is almost independent of temperature between 77°K and 250°K. At

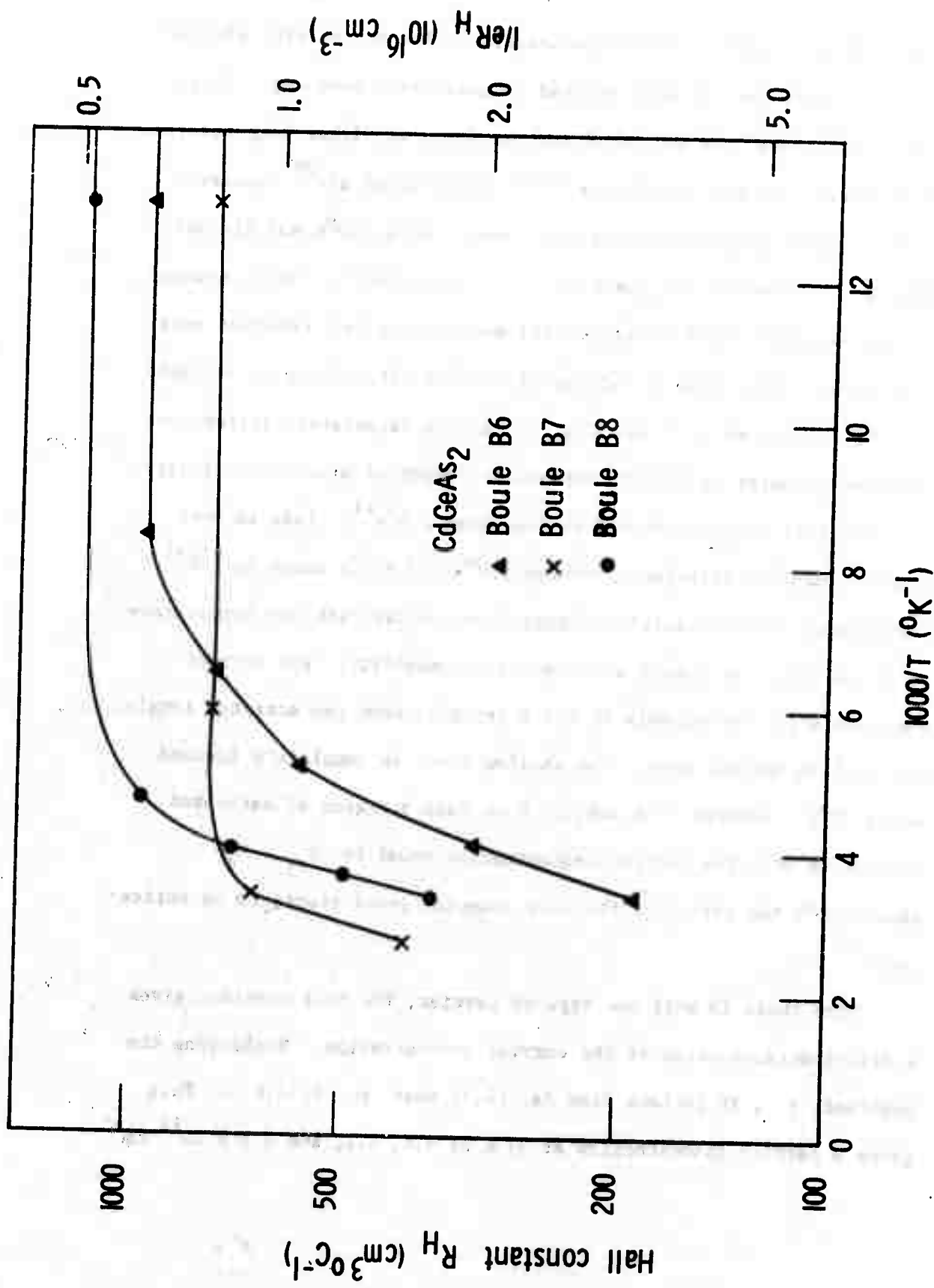


FIG. 5--Temperature dependence of the Hall constant for p-type CdGeAs₂

higher temperatures it starts to decrease. The resistivity plotted in Fig. 6 also has the same general temperature dependence. It is constant between 77°K and 250°K and decreases at higher temperatures. This agrees with published data.^{28,34} Vaipolin et al.²⁸ observed that the Hall constant started to decrease above 200°K and claimed that this was due to the onset of mixed conductivity. This, however, is not compatible with their results showing the Hall constant goes to zero at 500°K . With a bandgap of 0.53 eV , it is easy to estimate from Eqs. (4.5) or (4.6) and Fig. 4 that the temperature difference, measured in units of $1000/T$, between the onset of mixed conductivity and zero Hall constant should be less than 0.5°K^{-1} . This is much smaller than the difference between 200°K and 500°K which is 3°K^{-1} . Furthermore, the resistivity changes too quickly with the temperature to be explained by purely a change in the mobility. The correct interpretation is probably that the crystals have two acceptor levels, one shallow and one deep. The shallow level is completely ionized above 77°K . Between 77°K and 250°K we have a region of saturated conduction with the carrier concentration equal to $N_{a1} - N_d$. Above 250°K the effect of the deep acceptor level starts to be noticeable.

When there is only one type of carrier, the Hall constant gives a direct determination of the carrier concentration. Neglecting the constant r , it follows from Eq. (4.7) that $p = 1/|e|R$. This gives a carrier concentration at 77°K of 6.6, 8.1, and $5.3 \times 10^{15}\text{ cm}^{-3}$.

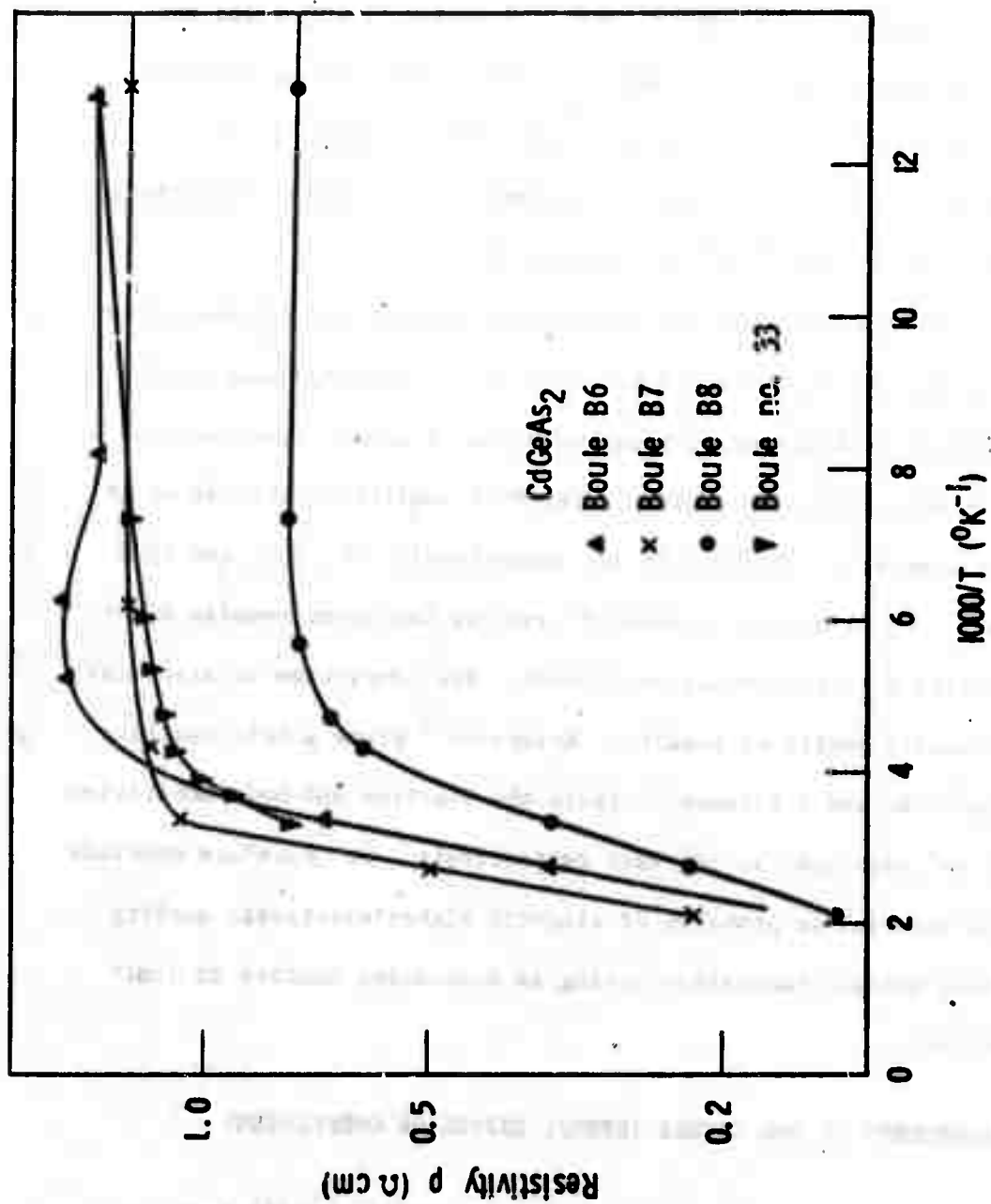


FIG. 6--Temperature dependence of the resistivity for p-type CdGeAs₂ .

respectively for the samples from boules B6, B7, and B8. Since the samples have a nondegenerate carrier concentration, we can use Eq. (4.20) to obtain a rough estimate of the impurity concentration that gives rise to the deep acceptor level. Equation (4.20) gives the carrier concentration at intermediate temperatures and we determine the ionization energy of the deep levels from the slope in Fig. 5. This gives $\epsilon_{a2} \approx 0.2$ eV, and we estimate the impurity concentration to be $N_{a2} \approx 4 \times 10^{17} \text{ cm}^{-3}$ for sample B8.

The Hall constant and the resistivity allow us to determine the Hall mobility which is defined by $\mu_H = R/\rho$. For our samples the Hall mobility is temperature independent up to almost room temperature. It then starts decreasing. The Hall mobilities calculated at 77°K for samples B6, B7, and B8 are respectively 676, 606, and 1540 cm^2/Vsec . The difference between B8 and the two other samples might be partially due to orientation effects. For comparison we also list the previously published results. Reference²⁸ gives a hole mobility of 20 cm^2/Vsec and reference 34 lists the electron and hole mobilities as 1000 cm^2/Vsec and 240 cm^2/Vsec respectively. We therefore conclude that our material is probably of slightly higher electronic quality with fewer ionized impurities acting as scattering centers to limit the mobility.

B. MEASUREMENT OF THE LINEAR THERMAL EXPANSION COEFFICIENT

We have measured the linear thermal expansion coefficient for CdGeAs_2 in the temperature range 80°C to 170°C, using an optical

interference technique. Figure 7 shows the experimental setup. To avoid vibrations the experiment should be performed on a stable table. A small tilt between the microscope slides gives rise to fringes, and the fringe spacing on the screen decreases with increasing tilt angle. The microscope slides were coated to obtain good fringe contrast. At times the contrast could be improved by a wedge blocking the zero order reflection. We had regular air in the furnace. Above 200°C it is necessary to use an inert atmosphere or vacuum to avoid growth of an oxide layer. A vacuum has the additional advantage that it is otherwise necessary to correct for the change in the index of refraction with the temperature of the gas between the microscope slides.

Let l be the sample thickness and n the index of refraction for air. The phase difference associated with one double reflection between the microscope slides is then given by $\phi = (4\pi/\lambda)nl$. Here $\lambda = 6328 \text{ \AA}$ is the wavelength of the He-Ne laser. A temperature change ΔT changes the phase difference by

$$\Delta\phi = \frac{4\pi}{\lambda} \left(\frac{dl}{dT} n + l \frac{dn}{dT} \right) \Delta T . \quad (4.21)$$

We measure $\Delta\phi$ by observing the fringe movement on the screen. For s fringes passing through a reference point, we have $\Delta\phi = 2\pi s$. By substituting this into Eq. (4.21) we determine the linear thermal coefficient α . We find

$$\alpha = \frac{1}{l} \frac{dl}{dT} = \frac{\lambda}{2nl} \frac{s}{\Delta T} - \frac{1}{n} \frac{dn}{dT} . \quad (4.22)$$

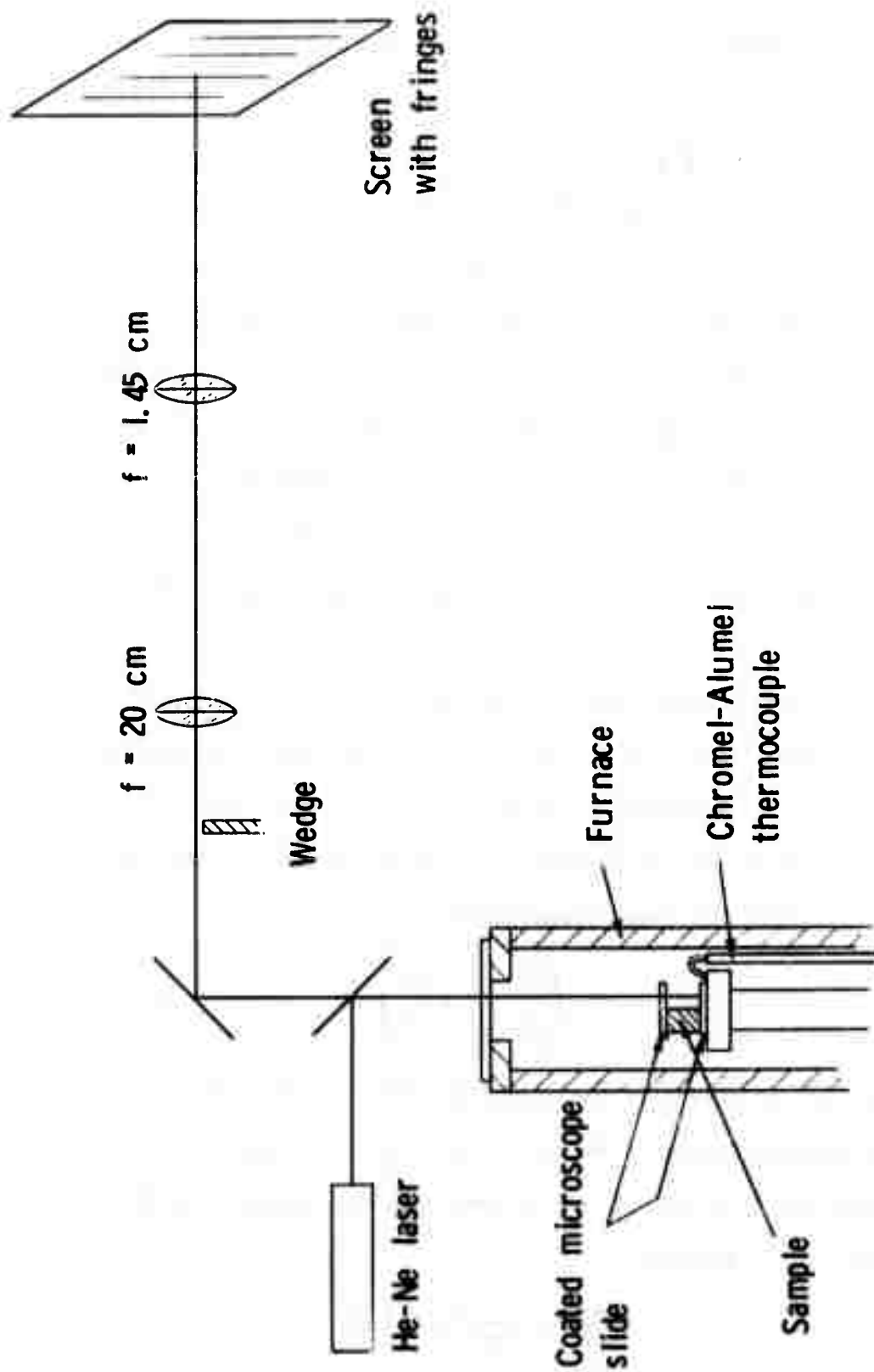


FIG. 7--Experimental setup for measuring the linear thermal expansion coefficient.

We see from Eq. (4.22) that we need to know dn/dT for air. The index of refraction for air can be written as $n = 1 + \frac{1}{2} \chi$ with the susceptibility χ proportional to the density $N/V = p/kT$. From this it follows that

$$\frac{n_{T_0} - 1}{n_T - 1} = \frac{p_0}{p} \frac{T}{T_0} \quad (4.23)$$

For $p = p_0$ and defining $\beta = 1/T_0$, we can rewrite this equation as

$$\frac{n_{T_0} - 1}{n_T - 1} = 1 + \beta(T - T_0) \quad (4.24)$$

Letting $T_0 = 273^\circ\text{K}$, we should theoretically have $\beta = 0.00367$. Experimentally β is found to be equal to 0.003679 for $\lambda = 6328 \text{ \AA}$ and $T_0 = 273^\circ\text{K}$.³⁵ For the same wavelength and temperature and a pressure of 760 mm Hg the index of refraction for dry air is $n_{T_0} = 1.0002921$. The temperature dependence is obtained by differentiating Eq. (4.24). We obtain

$$\frac{dn_T}{dT} = -\beta \frac{n_T - 1}{1 + \beta(T - T_0)} \quad (4.25)$$

The calculated dn_T/dT is plotted in Fig. 8.

In order to test the method we first measured a crystal with a known expansion coefficient. We used a single crystal of silicon 3.99 mm thick. The results are listed in Table III. In Fig. 9 we compare the results with the data for polycrystalline silicon from reference 36. The agreement is good.

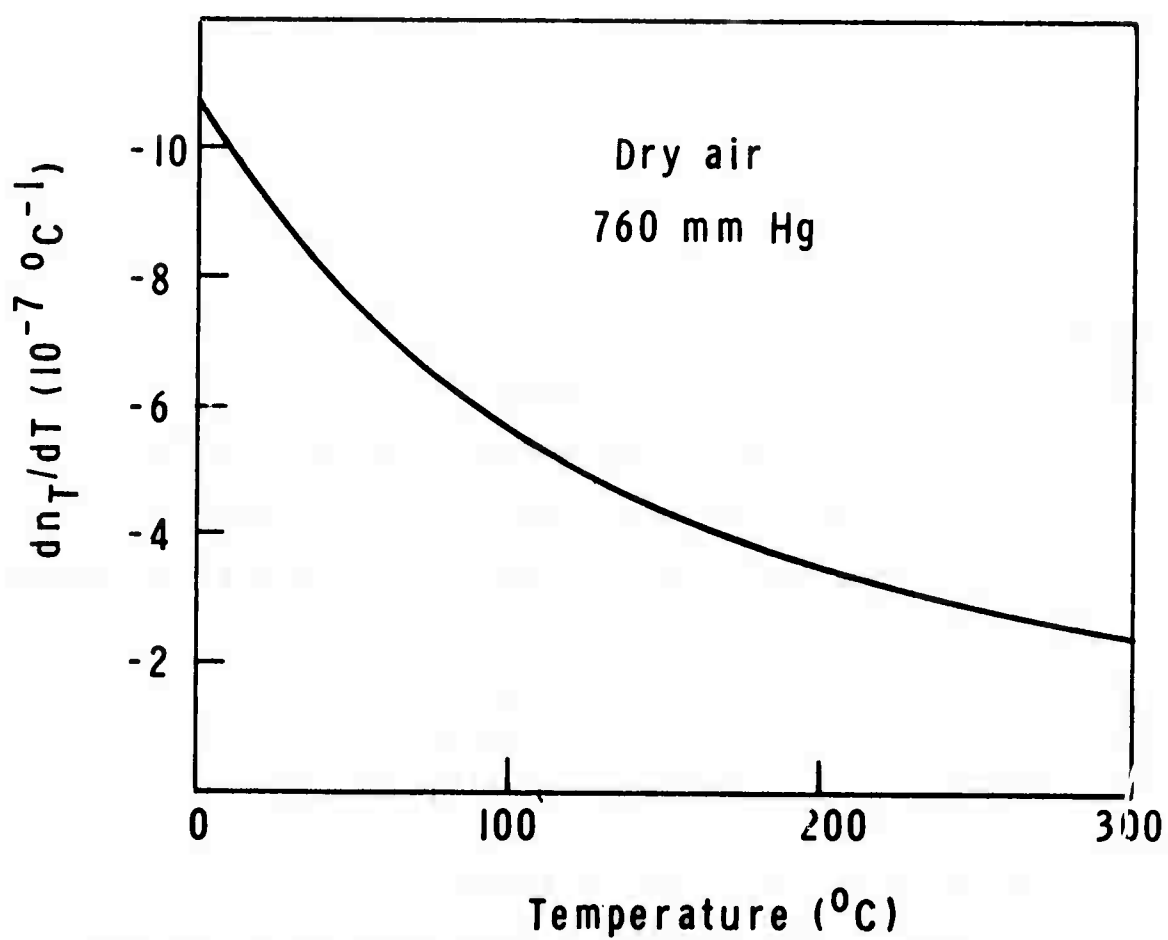


FIG. 8-- $-dn_T/dT$ for dry air at 760 mm Hg.

TABLE III

LINEAR THERMAL EXPANSION COEFFICIENT FOR SILICON

T	$\frac{\lambda}{2\pi l} \frac{s}{\Delta T}$	$\left(\frac{1}{n} \frac{dn}{dT}\right)_{\text{air}}$	α
$^{\circ}\text{C}$	$(10^{-6} \text{ }^{\circ}\text{K}^{-1})$	$(10^{-6} \text{ }^{\circ}\text{K}^{-1})$	$(10^{-6} \text{ }^{\circ}\text{K}^{-1})$
82.5	1.85	- 0.64	2.49
113	2.17	- 0.53	2.70
147	2.29	- 0.46	2.75

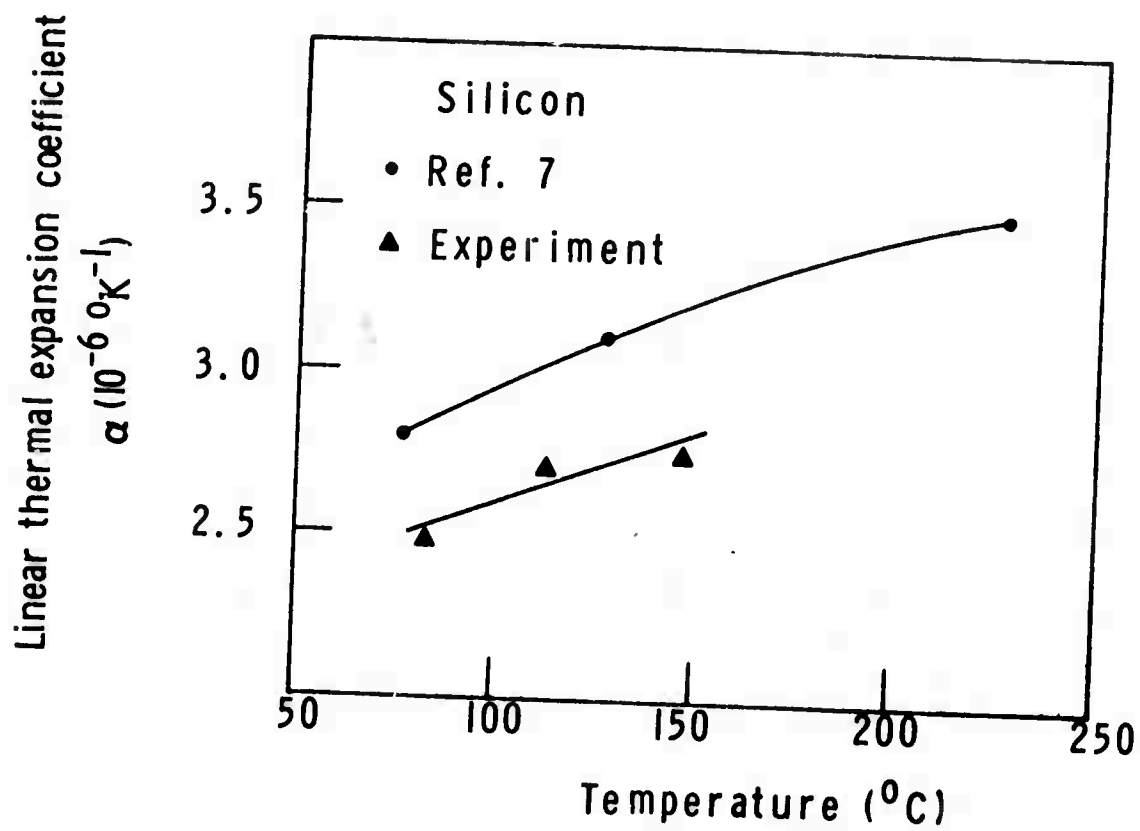


FIG. 9--Linear thermal expansion coefficient for silicon.

We had two crystals of CdGeAs_2 , one c-axis cut 4.01 mm thick and one a-axis cut 2.96 mm thick. CdGeAs_2 proved to have a very anisotropic linear thermal expansion coefficient with α_{\perp} more than ten times larger than α_{\parallel} . The results for a-axis expansion are listed in Table IV. For the c-axis expansion we did not obtain equally accurate measurements because α_{\parallel} was of the same order as dn/dT for air, but of opposite sign, such that the fringe movement was almost zero. The results are in Table V. In Fig. 10 we plot the temperature dependence of the expansion coefficients. The expansion coefficients increase slightly with the temperature.

TABLE IV
 LINEAR THERMAL a-AXIS EXPANSION COEFFICIENT FOR CdGeAs₂

T (°C)	$\frac{\lambda}{2n} \frac{s}{\Delta T}$ (10 ⁻⁶ °K ⁻¹)	$\left(\frac{1}{n} \frac{dn}{dT}\right)_{\text{air}}$ (10 ⁻⁶ °K ⁻¹)	α_{\perp} (10 ⁻⁶ °K ⁻¹)
79.3	7.64	-0.64	8.28
110	7.93	-0.54	8.47
142	8.18	-0.46	8.64
171	8.47	-0.40	8.87

TABLE V

LINEAR THERMAL c-AXIS EXPANSION COEFFICIENT FOR CdGeAs_2

T (°C)	$\frac{\lambda}{2\pi l} \frac{s}{\Delta T}$ ($10^{-6} \text{ }^\circ\text{K}^{-1}$)	$\left(\frac{1}{n} \frac{dn}{dT}\right)_{\text{air}}$ ($10^{-6} \text{ }^\circ\text{K}^{-1}$)	α_{\parallel} ($10^{-6} \text{ }^\circ\text{K}^{-1}$)
128	-0.14	-0.49	0.35
245	0.34	-0.30	0.64
288	0.50	-0.25	0.75

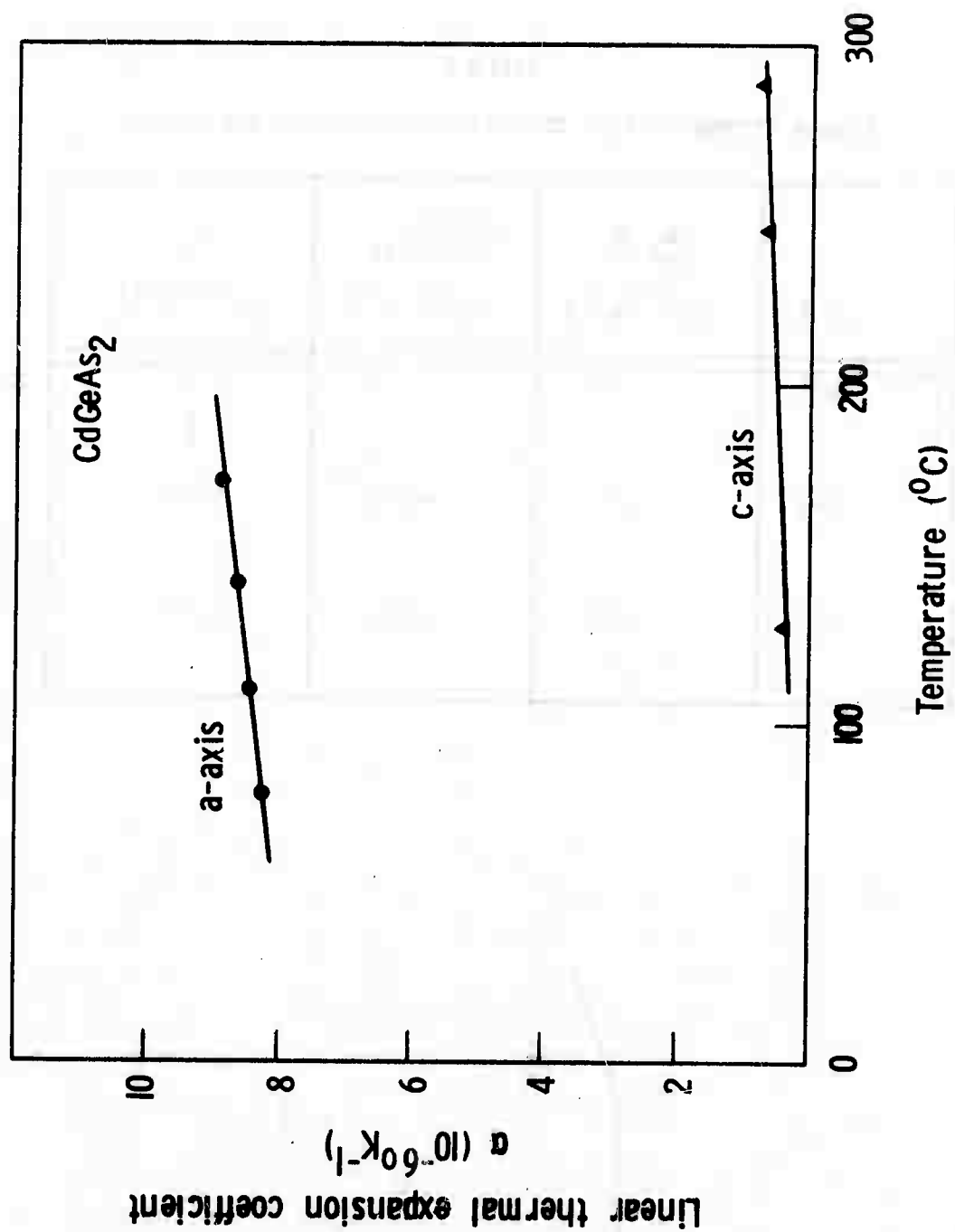


FIG. 10--Linear thermal expansion coefficient for CdGeAs₂.

CRYSTAL GROWTH AND MATERIAL EVALUATION

In this chapter we briefly describe the growth technique and then the testing procedures used to evaluate chalcopyrite crystals. The problems of main concern are the optical transmission and crystal cracking. Fortunately, the necessary crystal size for most nonlinear optic applications is only a few millimeters so samples can be cut from the best sections of the boules. The crystals are grown at the Center for Materials Research (CMR) at Stanford.

A. GROWTH METHOD

1. CdGeAs₂

References 37 and 38 discuss the equilibrium phase diagram of CdGeAs₂. The crystal melts congruently at 670°C. The homogeneity region is believed to be very narrow. It probably extends only a fraction of a percent away from the stoichiometric composition which is helpful in obtaining uniform single crystals. All our measurements have been on samples grown by the vertical Bridgman-Stockbarger technique.

Stoichiometric proportions of the elements (6N) are placed in a quartz tube which then is sealed under vacuum. The material is reacted for 16 hours at a temperature of 730 to 740°C. The temperature is raised slowly since the arsenic vapor pressure is about 10 atm at 730°C. After complete reaction, the material is ready for Bridgman growth. The furnace is vertical with a temperature profile as illustrated in Fig. 11. The quartz crucible is placed near the top of the

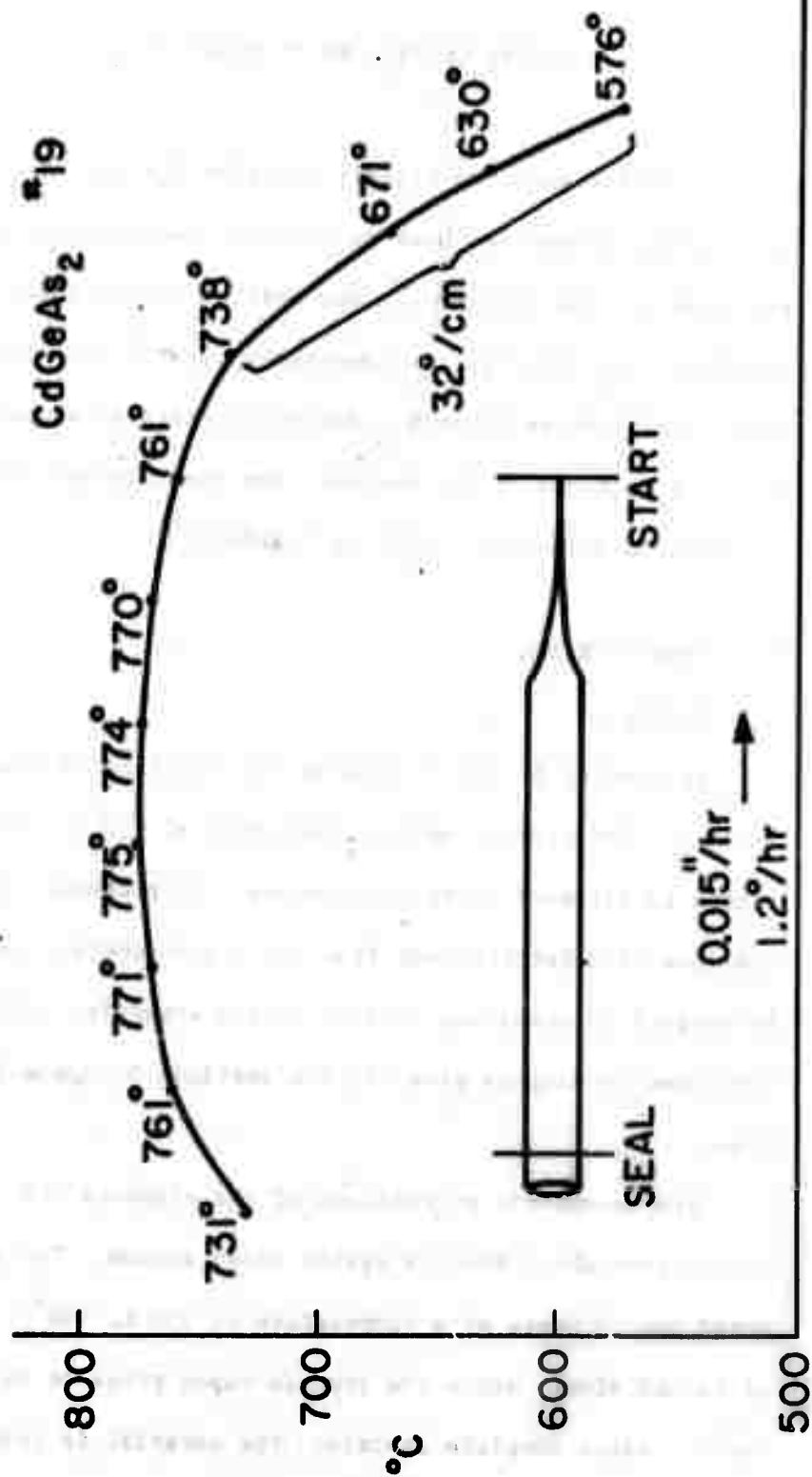


FIG. 11--Oven gradient and quartz crucible for Bridgman-Stockbarger growth of CdGeAs_2 .

furnace and is lowered slowly through the temperature gradient. To aid formation of a single crystal, the crucible has a 1 to $1\frac{1}{2}$ inch long capillary at the bottom. The synthesis and growth can be done in one or two steps. The two step procedure has the disadvantage that some vapor in the crucible deposits on the walls when the synthesized material is quenched, and it is not possible to retrieve this deposit. The one step process assures that no material is lost. However, there is a problem of obtaining uniform mixing and achieving fully reacted material in the crucible as well as in the capillary before the growth starts. An ultrasonic vibrator aids the mixing process. To prevent reaction of the melt with the crucible walls a carbon layer is used to coat the inside of the quartz crucible. Boules grown without the carbon layer did not show any noticeable change in the optical transmission.

Figure 12 shows a photograph of a boule. The boules are usually 2.5 cm long and 1.3 cm in diameter with the general properties fairly repeatable from run to run. There is, however, a secondary nucleation problem. The boules start as single crystals, but after 0.5 to 1 cm of growth the melt becomes unstable and numerous small crystals form from nucleation sites. In trying to eliminate this problem, the growth conditions have been varied over a wide range. The lowering rate of the crucible has been changed between 0.25 and 27 mm/hour and the temperature gradient between 11.8 and $34^{\circ}\text{C}/\text{cm}$, this has not resulted in any improvement. Another problem is extensive crystal cracking which occurs at all investigated growth conditions.



FIG. 12--CdGeAs₂ boule grown by the Bridgman method.

2. CdGeP₂

The melting point of CdGeP₂ is at 790°C. Because of the high phosphorus vapor pressure, CdP₂ is synthesized first and then reacted with Ge to form CdGeP₂ at a temperature above the melting point of Ge. The fully reacted material is then used to grow single crystals by the Bridgman-Stockbarger technique similar to the growth of CdGeAs₂. Due to observed Si vitrification, a carbon crucible is used to synthesize the CdGeP₂. The resulting crystals show the same cracking pattern as observed for CdGeAs₂.

B. INITIAL TESTING

1. Polishing and Etching

Both CdGeAs₂ and CdGeP₂ polish well. Since the crystals are anisotropic, the grain boundaries and the twin lines can be seen on a polished surface using a microscope and partially crossed polarizers. Without polarizers it is necessary to use a suitable etch to reveal the structure. A good etch for CdGeAs₂ is 1H₂O₂: 2NH₄OH: 4H₂O and etching for 30 sec. For CdGeP₂ etching for 15 sec in a 10% Br₂ solution in ethyl alcohol gives good results. The best section of the boule is usually the region within 0.5 to 1 cm from the capillary. This section most often consists of two or three crystallites. For growth from stoichiometric melt there is no evidence of inclusions except near the top of the boules.

2. Cracking

Due to the extensive cracking, the largest single crystals of CdGeAs₂ useful for nonlinear optics have to date been limited to

approximately 4 mm^3 . It has been suggested that the cracking in CdGeAs_2 is due to a sphalerite to chalcopyrite phase transition at 630°C .^{3,39} We have, however, some doubt about the phase transition since we have not been able to verify the sphalerite phase in samples quenched from temperatures above 630°C . The large anisotropy in the thermal expansion (cf. Chapter IV) may also give rise to cracking. There is a definite correlation between the cracking and the grain boundaries. Large single crystal regions usually have few cracks, and it is hoped that the cracking will reduce with improved growth techniques. Finally, the cracking may be related to the constraints imposed by the walls of the quartz crucible.

3. Growth Direction

We have taken Laue photographs of several boules to determine the preferred growth direction. In a few boules strain caused blurring of the Laue spots. The orientation of large single crystal regions is usually with the chalcopyrite unit cell [111] direction within 10° of the boule axis. This agrees with the literature which reports the [111] direction as the fastest growth direction for the chalcopyrites.

The impurity segregation coefficient and the density of stoichiometric imperfections may depend on the growth direction. Boule number 31 had two twins with a large disparity in the optical transmission. The smaller piece was transparent. It grew in a direction of 17° off the c-axis in the [100] plane. The larger piece, however, which was completely opaque, grew close to the [221] direction. To see if there was any significant difference in the impurity concentration between the two samples, they were sent out for impurity analysis. The results,

however, were not conclusive. They are summarized in Table X.

4. Optical Transmission

The property of the greatest concern is the optical transmission. Since the bandgap of CdGeAs_2 is at $2.3 \mu\text{m}$, visual inspection is not possible. Slices 1 mm thick are therefore cut from several sections of the boule. They are polished and the optical transmission is measured on a 621 Perkin-Elmer spectrophotometer. Most boules have a very non-uniform transmission with the best transmission usually at the bottom. Uniform transmission exists only over very limited regions. The transmission including reflection losses through one of our best samples of p-type CdGeAs_2 is shown in Fig. 13. More often the best transmission in a boule is between 20 to 30% for a 1 mm thick sample. The bandgap at $2.3 \mu\text{m}$ and the two phonon absorption at $18 \mu\text{m}$ determine the transmission range. Some weak three phonon absorption exists between 12 to $13 \mu\text{m}$. There is no free carrier absorption in p-type samples. For most samples, however, significant absorption occurs between the bandgap and 5 to $6 \mu\text{m}$. This absorption is not seen in n-type samples which in return have a shorter infrared cutoff wavelength due to free electron absorption. Due to the larger bandgap the quality of CdGeP_2 can be studied using an infrared microscope which makes evaluation easier than for CdGeAs_2 . The boundary between transparent and opaque regions usually follows sharp lines and there is often a correlation between crack lines and opaque regions (cf. Fig. 14). The cracking is concentrated on the boundary between single crystal regions. The optical transmission range for n-type CdGeP_2 is 0.8μ to $12.5 \mu\text{m}$ as shown in Fig. 15. There is some

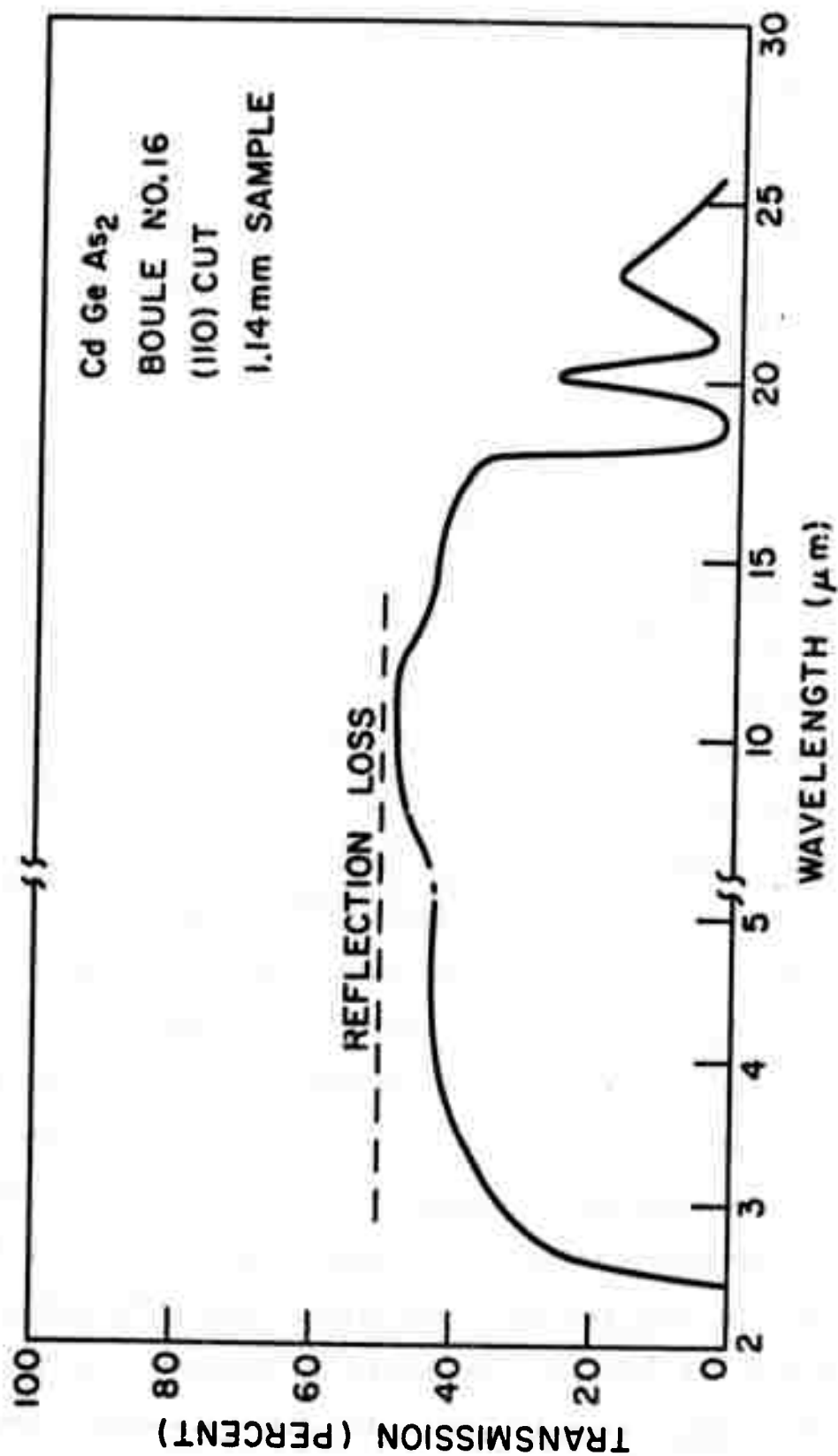


FIG. 13--Transmittance of a single crystal of p-type CdGeAs₂.



FIG. 14--Transmission through CdGeP_2 photographed through an IR microscope.

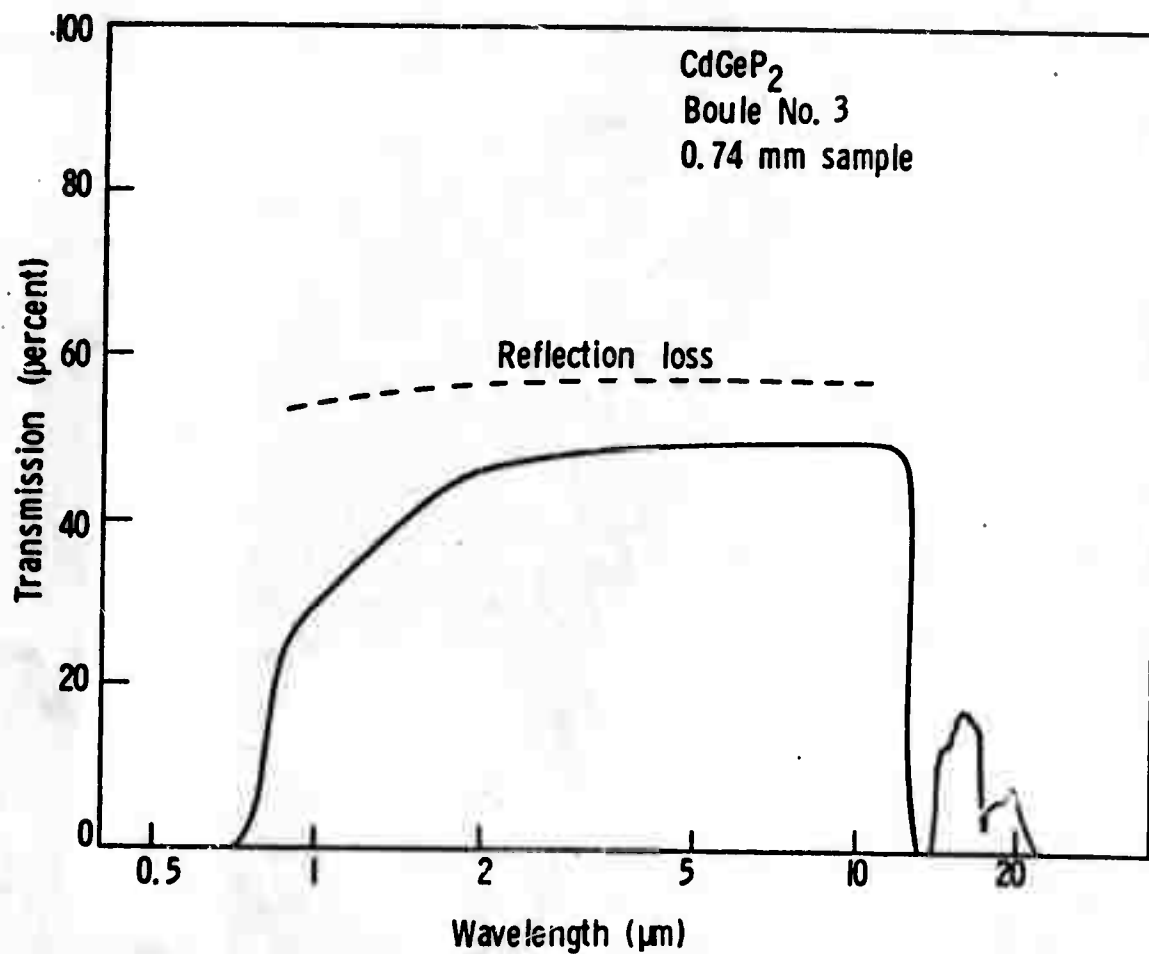


FIG. 15--Measured transmission range for n-type CdGeP_2 .

absorption at short wavelengths close to the bandgap frequency. Similar absorption is seen in several of the II-VI semiconductor compounds.

5. Measurement of the Resistivity and the Sign of the Majority Carrier

After the samples have been tested for optical transmission, they are etched and the resistivity is measured by the four point probe method. In addition, a hot probe is used to determine the sign of the majority carriers. Growth of CdGeAs_2 from stoichiometric melt gives p-type material except for a region close to the capillary where there may be a small n-type region. Crystals have been grown from melt with 0.5 to 1% excess arsenic, and one boule was grown with 2% excess germanium. These boules were also p-type. The optical transmission and resistivity of boules grown from arsenic rich melt are about the same as for stoichiometric grown boules. Electron probe microanalysis revealed arsenic inclusions near the top, and in that region the material was n-type. The germanium rich boule had very nonuniform transmission due to germanium precipitates.

The resistivity correlates with the optical transmission. For p-type CdGeAs_2 the resistivity at room temperature is between $0.5 \Omega \text{ cm}$ and $15 \Omega \text{ cm}$ with the largest resistivity resulting in the best optical transmission. An exception was boule number 28 which had a resistivity of about $100 \Omega \text{ cm}$. This high resistivity was probably due to a reduced mobility because of strain since this boule was quenched from 480°C . The presence of strain was confirmed by measuring second harmonic generation in a wedged sample.

The resistivity sometimes varies significantly across the boule cross section. This is also reflected in the nonuniform optical transmission. The variation in resistivity can be by a factor of five or more. For example, for boule number 31 which consisted of two single crystals, one transparent and one opaque, the resistivity was 7.5 to 15 Ω cm and 2.4 Ω cm respectively.

In n-type CdGeAs_2 the resistivity is usually much smaller than 1 Ω cm and the crystal is opaque.

Only a few boules have been grown of CdGeP_2 . The boules were n-type with a resistivity of 10^4 to 10^5 Ω cm.

C. OTHER TESTS

1. Electron Probe Microanalysis

We have made extensive microprobe analysis of several boules to investigate possible deviations from stoichiometric composition. The absolute accuracy of microprobe measurements are between 2 and 5 weight percent. For absolute calibration we use Cd, CdS, Ge, and GaAs as standards and determine the weight fraction W_u of the elements in the unknown (CdGeAs_2) using the expression

$$W_u = W_s \frac{F_s}{F_u} \frac{I_s}{I_u} \quad (5.1)$$

where W_s is the weight fraction of the element in the standard, I_s and I_u are the x-ray intensities from the standard and the unknown, and F_s and F_u corrects for the matrix absorption in the standard and the unknown.

We have determined F_s/F_u from tables in Birks⁴⁰ for an accelerating voltage of 25 kV, electrons incident at 62.5° , and a takeoff angle Ψ of 38.5° . Table VI gives the product $W_s F_s/F_u$. Equation (5.1) does not include any matrix enhancement factor since at 25 kV there is negligible enhancement in the x-ray intensity because of excitation by the characteristic fluorescence from the other elements in the matrix.

Figure 16 shows an etched boule cross section of CdGeAs_2 containing several grains. The left side of the cross section was transparent and p-type and the right side opaque and n-type. Table VII gives the results of the microprobe analysis. No variation in stoichiometry over the cross section or irregularities at the grain boundaries could be observed within the experimental resolution.

The relative accuracy of the microprobe analysis can be as good as a few tenths of one percent. Table VIII lists some experimental results for different boules of CdGeAs_2 . Within the experimental error excess As does not perturb the stoichiometric composition. The results agree with the previous phase diagram studies, that CdGeAs_2 exists only in a narrow homogeneity region.

2. Impurity Analysis

The purification of compound semiconductors is far more difficult than for the element semiconductors. It is not sufficient to remove foreign atoms. The stoichiometric composition must also be controlled. The observed carrier concentration is probably related to both impurities and stoichiometric variations. Since there are approximately 10^{22} atoms/cm³ a carrier concentration of 10^{16} cm⁻³ corresponds to only 1 ppm of

TABLE VI

MAGNITUDE OF $W_s F_s / F_u$ FOR MICROPROBE ANALYSIS OF CdGeAs_2

Standard	$\text{Cd}_{L\alpha}$	$\text{Ge}_{K\alpha}$	$\text{As}_{K\alpha}$
Cd	115.26	101.99	49.37
CdS	82.23		
Ge			
GaAs			

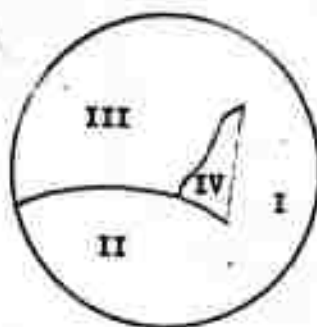


FIGURE 16

TABLE VII

MICROPROBE ANALYSIS OF SLICE No. 9 FROM BOULE No. 34 of CdGeAs_2

Area	W_{Cd}	W_{Ge}	W_{As}
I	32.11	21.94	45.95
II	31.97	21.96	46.07
III	31.97	21.93	46.11
IV	32.30	21.78	45.92



(cf. Fig. 16)

TABLE VIII

MICROPROBE ANALYSIS OF CdGeAs_2

Boule Number	W_{Cd}	W_{Ge}	W_{As}	Growth Condition	Optical Transmission
16	31.33	22.21	46.46	0.5 Wt % excess As	Opaque
26A (top of boule)	31.33	22.12	46.55	Stoichiometric	Max 40%
26C	31.34	22.29	46.36	Stoichiometric	Max 15%
31	31.64	22.03	46.34	0.5 Wt % excess As	Max 10%
33	31.38	22.36	46.26	0.5 Wt % excess As	Max 25%
CdGeAs_2	33.57	21.68	44.75		

electrically active impurities or lattice vacancies. A considerable amount of self compensation probably occurs in CdGeAs_2 and CdGeP_2 .

Table IX shows the results of an impurity analysis of three slices from boule number 33. The slices were from different sections of the boule and they had different resistivity and optical transmission. The impurity analysis was performed by the Bell and Howell Electronic Materials Division in Pasadena using spark source mass spectrometry. There appears to be very little correlation between the impurity analysis and the optical transmission. A possible explanation is that only a small fraction of the boule cross section was probed and homogeneity problems may have obscured the results. The probed area was less than one mm^2 and only a few tenths of a milligram was analyzed. The usually large oxygen and carbon concentrations are most probably due to hydrocarbons and possibly an oxide layer on the surface.

The analysis of the transparent and the opaque twin in Boule number 31 is listed in Table X. Here also there is very little correlation between impurities and transparency. Besides oxygen and carbon, only silicon and sulfur impurities are present at a significant level.

Most of the crystal growth effort has centered on the Bridgman method. We decided to investigate this method since it is a relatively simple method which usually provides good results. In addition, the method had already been used by others to grow chalcopyrites. The Bridgman growth program is now near completion. We have been unable to solve the cracking problem and the optical transmission is very nonuniform throughout the boules. Fortunately, however, the necessary crystal size for efficient nonlinear interactions is only 2 to 5 mm

and from some sections of the boules we have obtained crystals of sufficient quality to demonstrate efficient second harmonic generation of a CO₂ laser. The absorption, however, is still too large for parametric oscillators. We have tried to link the absorption to the impurities or stoichiometric variations using mass spectrometric and electron microprobe analysis, but we have not seen any significant correlation. This does not exclude stoichiometric variations, however, since the microprobe at best has a relative accuracy of only 0.1%. Much smaller variations in the stoichiometry can have significant influence on the absorption and carrier concentration. With reproducible growth results the next obvious step is to examine how compensation and also doping affect the optical transmission. Alternative growth methods which allow seeding and avoid the constraints set by the crucible wall should also be explored. With a large anisotropic thermal expansion coefficient c-axis growth is probably best for reducing cracks. It also helps to grow single crystals. In the Bridgman boules the large strain building up at the grain boundaries leads to cracking.

Recently we have tried a new growth technique with very encouraging results. By growth from a bismuth solution we have obtained single crystals with almost no cracks. The optical absorption is still too high, but the elimination of cracks is a significant step in the right direction.

TABLE IX

IMPURITY CONCENTRATIONS IN CADMIUM GERMANIUM ARSENIDE
(IN PARTS PER MILLION ATOMIC)

Element ^(a)	Detection Limit ^(b)	Opaque	Max T = 20%	Max T = 5%
Li	0.007	0.012	0.083	0.017
C	0.03	4.6-25	3,200 (75-10,000)	19
N	0.03	0.18	0.51	0.28
O	0.03	76	900	3,600
F	0.07	0.27	0.48	0.22
Na	0.01	0.35	8.3	0.73
Mg	0.3	N.D.	0.49	N.D.
Al	0.1	0.37	3.9	0.80
Si	1	6.7	N.D.	N.D.
S	0.03	1.5	1.1	4.5
K	0.01	0.052	0.51 (6.6*)	0.19
Ca	0.03	0.065	0.25 (3.3*)	0.074

(a) No analysis was made for hydrogen. Analyses for gold are not given since the samples were sparked against high purity gold counter-electrodes. Background lines of the matrix interfere with the analyses for Cl, Mn, and Fe. Other impurities not listed were not detected and have concentrations less than 0.3 ppma.

(b) Determined for 3×10^{-7} coulomb exposure.

* Seen on one exposure only.

N.D. Not detected.

TABLE X

IMPURITY CONCENTRATIONS IN CADMIUM GERMANIUM ARSENIDE

(IN PARTS PER MILLION ATOMIC)

Boule Number 31

Element ^(a)	Detection Limit ^(b)	Transparent Sample	Opaque Sample
Li	0.007	0.077	0.021
B	0.02	0.046	0.075
C	0.03	31	110
N	0.03	1.7	2.0
O	0.03	27	120
F	0.07	0.1	0.1
Na	0.01	1.8	5.4
Mg	1	N.D.	N.D.
Al	0.1	1.8	3.3
Si	0.3	3.1	16
P	0.03	0.094	0.19
S	0.03	4.5	1.8
Cl	300	N.D.	N.D.
K	0.01	1.5	4.7
Ca	0.03	0.78	1.5
V	0.05	0.20	0.33
Cu	0.07	0.45	0.93
Zn	0.07	0.2	0.78
Ga	0.1	0.1	0.29
Sn	0.1	0.65	1.9
I	0.07	0.39	0.24

(a) No analysis was made for hydrogen. Background lines of the matrix interfere with the analyses for manganese and iron. Other impurities not listed were not detected and have concentrations less than 0.3 ppma.

(b) Determined for 3×10^{-7} coulomb exposure.
N.D. Not detected.

CHAPTER VI

LINEAR AND NONLINEAR OPTICAL PROPERTIES

A. THEORY

In this chapter we briefly review some nonlinear optical theory as a necessary background and then present our experimental results. We also discuss the optical absorption mechanisms in chalcopyrite crystals.

1. Second Order Nonlinear Interactions

(a) Effective nonlinear coefficient

The symmetry restrictions on the second order nonlinear coefficient are the same as for the piezoelectric tensor. For the chalcopyrites which have $\bar{4}2m$ symmetry, the generated nonlinear polarizations along the principal axes in terms of the electric field amplitudes are therefore⁶

$$\begin{aligned} P_x &= 2d_{14}E_yE_z \\ P_y &= 2d_{14}E_zE_x \\ P_z &= 2d_{36}E_xE_y \end{aligned} \quad (6.1)$$

Since $d_{14} = d_{36}$ according to the Kleinman symmetry condition, the chalcopyrites have only one independent nonlinear coefficient. The polarization tensor, which is the same as that for KDP, allows both type I and type II phasematching. The phasematching or conservation of momentum conditions for the type I and type II phasematching

in a positive birefringent crystal are respectively

$$\omega_p n_p^o = \omega_s n_s^e + \omega_i n_i^e \quad (6.2)$$

and

$$\omega_p n_p^o = \omega_s n_s^e + \omega_i n_i^o, \quad (6.3)$$

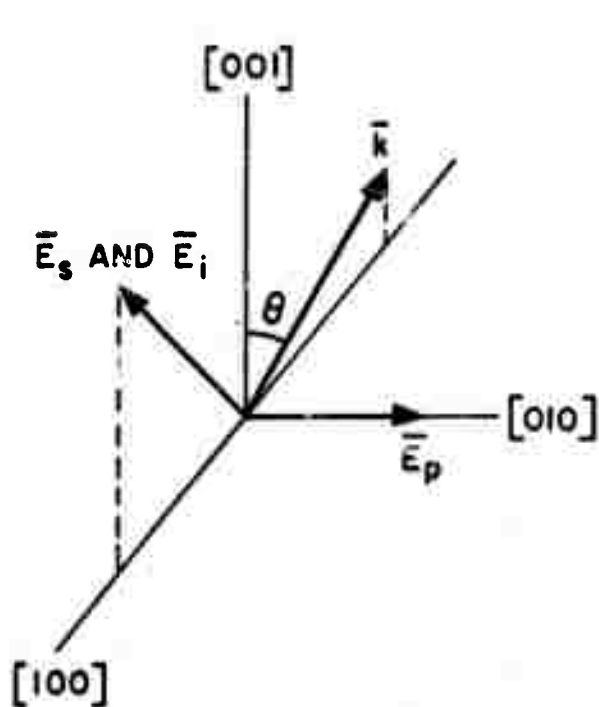
where the superscripts *e* and *o* denote extraordinary and ordinary waves and *p*, *s*, and *i* refer to the pump, signal, and idler fields. In addition, conservation of energy requires $\omega_p = \omega_s + \omega_i$.

For type I phasematching the effective nonlinear coefficient is $d_{14} \sin 2\theta$ where θ is the angle between the direction of propagation and the *c*-axis. The signal and idler are extraordinary waves polarized in the (010) plane and the perpendicular pump wave is ordinary. Maximum nonlinear interaction occurs at $\theta = 45^\circ$. Only type II phasematching allows interaction in the 90° direction. The effective nonlinear coefficient for type II phasematching is $d_{14} \sin \theta$ with the signal polarized as an extraordinary wave in the (110) plane and the idler polarized parallel to the pump as an ordinary wave. Figure 17 shows how the fields are polarized for the two phasematching conditions.

For second harmonic generation (SHG) the Eqs. (6.1) reduce to

$$\begin{aligned} P_2 &= d_{14} \sin 2\theta E_1^2 \\ P_1 &= 2d_{14} \sin 2\theta E_1 E_2 \end{aligned} \quad (6.4)$$

for type I phasematching where the subscripts 1 and 2 refer to the fundamental and the second harmonic waves. The fundamental wave is



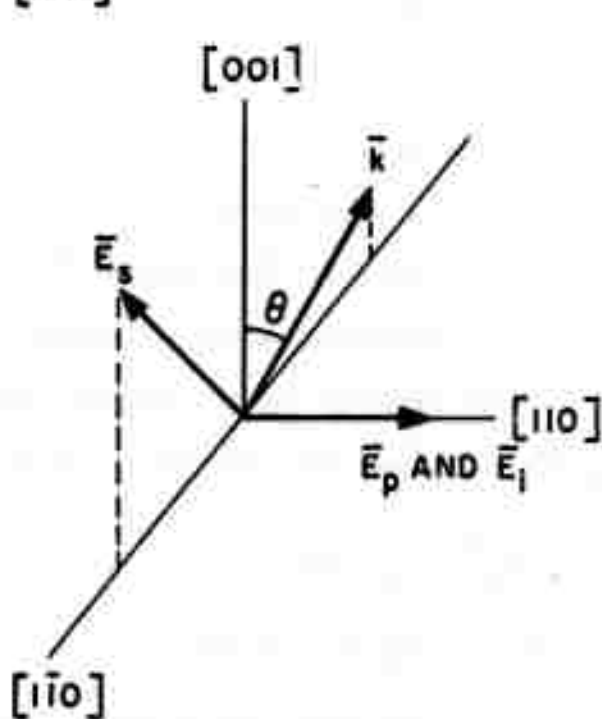
$$\underline{\underline{A}}$$

$$n_p^e \omega_p = n_s^e(\theta) \omega_s + n_i^e(\theta) \omega_i$$

$$P_p = 2d_{14} \sin 2\theta E_s E_i$$

$$P_s = 2d_{14} \sin 2\theta E_i E_p$$

$$P_i = 2d_{14} \sin 2\theta E_s E_p$$



$$\underline{\underline{B}}$$

$$n_p^o \omega_p = n_s^o(\theta) \omega_s + n_i^o \omega_i$$

$$P_p = 2d_{14} \sin \theta E_s E_i$$

$$P_s = 2d_{14} \sin \theta E_i E_p$$

$$P_i = 2d_{14} \sin \theta E_s E_p$$

FIG. 17--Type I and type II phasematching in a positive birefringent crystal of $\bar{4}2m$ symmetry.

polarized along \bar{E}_s or \bar{E}_i in Fig. 19(a) and the second harmonic in the \bar{E}_p direction. For type II phasematching we have

$$\begin{aligned} P_2 &= d_{14} \sin \theta E_1^2 \\ P_1 &= 2d_{14} \sin \theta E_1 E_2 \end{aligned} \quad (6.5)$$

Referring to Fig. 19(b) the fundamental wave is now polarized in the (\bar{E}_s, \bar{E}_p) plane 45° to the \bar{E}_p direction and the second harmonic along \bar{E}_p or \bar{E}_i .

(b) Second harmonic conversion efficiency

Starting from Maxwell's equations we can determine the second harmonic conversion efficiency. This is a standard calculation, and reference 4 gives an excellent treatment of the subject. For reference, we therefore only state the results. Introducing an effective non-linear coefficient d such that $P_2 = dE_1^2$, we have that the second harmonic power P_2 is given by the equation⁴

$$P_2 = \kappa P_1^2 l k_1 h, \quad (6.6)$$

where P_1 is the laser power at the fundamental frequency and the constant κ in mks units is given by

$$\kappa = \frac{2\eta_0^3 \omega_1^2 d^2}{n_1^2 n_2 \pi} \quad (6.7)$$

The dimensionless quantity h in Eq. (6.6) includes the effects of double refraction and focusing. It is tabulated in reference 4 and

is of the order of unity or smaller. Further l is the crystal length, n_1 and n_2 are the indices of refraction at the fundamental and second harmonic frequencies, $k_1 = n_1 \omega_1 / c$ is the wavevector, and finally $\eta_0 = 377 \Omega$ is the free space impedance. In order to compare nonlinear materials, a figure of merit is often defined given by

$$M_1 = \frac{d^2}{n_1^2 n_2} \quad (6.8)$$

This definition, however, neglects the limitations set by double refraction for phasematching at other angles than 90° . To correctly account for this, we introduce two other figure of merits which apply to the cases of maximizing the total SHG power and the SHG power in the Gaussian mode. We first define a few parameters. The fundamental wave has a spot size w_1 located at the center of the crystal and the confocal parameter is

$$b = \frac{2\pi n_1 w_1^2}{\lambda_1} \quad (6.9)$$

The parameters ξ and B describe the focusing and the double refraction. They are given by

$$\xi = l/b \quad \text{and} \quad B = \frac{1}{2} \rho(\ell k_1)^{1/2}, \quad (6.10)$$

where ρ is the double refraction angle defined in Appendix A. We consider first the case of total SHG power. For optimum focusing ($\xi_m = 1.392$) and $B > 2$ we have that h in Eq. (6.6) reduces

to the approximate expression

$$h_{mm} = 0.714/B \quad (6.11)$$

From Eqs. (6.6), (6.10), and (6.11) it follows that under these conditions the SHG power improves only with the square root of the crystal length and the appropriate crystal figure of merit is given by expression

$$M_{SHG \text{ tot}} = \frac{d^2}{n_1^{3/2} n_2 \rho} \quad (6.12)$$

For convenience we write the condition $B > 2$ in terms of the aperture length l_a which is defined by

$$l_a = \frac{\pi^{1/2} w_1}{\rho} \quad (6.13)$$

since sometimes this parameter is used instead of B . The aperture length should be longer than the crystal length in order for the SHG power not to be limited by the double refraction. With $B = (\pi^{1/2}/2) (l/l_a) k_m^{-1/2} > 2$ we obtain $l_a < 0.3 l$.

For many applications diffraction limited beams are of importance. The maximum SHG power in the Gaussian mode is obtained by substituting the expression

$$\bar{h}_{mm}(B) \approx \frac{\bar{h}_{mm}(0)}{1 + (4B^2/\pi) \bar{h}_{mm}(0)} \quad (6.14)$$

into Eq. (6.6). Here $\bar{h}_{mm}(0)$ is equal to 1.068. Equation (6.14) holds

to within 10% for all B . It is clear from Eqs. (6.6) and (6.14) that the Gaussian SHG power saturates for $(4B^2/\pi)\bar{h}_{mm}(0) > 1$, and we use this to define a maximum useful crystal length l_{max} given by

$$l_{max} \approx \frac{\lambda_1}{2n_1\rho^2\bar{h}_{mm}(0)} \quad (6.15)$$

For l greater than l_{max} the SHG power is

$$P_2 \approx \kappa P_1^2 \frac{\pi}{\rho^2} \quad (6.16)$$

and in this case the figure of merit is given by

$$M_{SHG \text{ Gaus}} = \frac{d^2}{n_1^2 n_2 \rho^2} \quad (6.17)$$

We later use the figure of merit expressions to compare the chalcopyrites with other existing infrared nonlinear materials.

For weak focusing ($F < 1$) and negligible walk-off ($B < 0.5$), we have $h \approx F$ and Eq. (6.6) reduces to

$$P_2 = \kappa \left(\frac{P_1 l}{v_1} \right)^2 \quad (6.18)$$

This equation is valid for small conversion efficiencies. It assumes that the phasematching condition is satisfied and neglects absorption.

For large conversion efficiencies the exact expression given by

$$P_2 = P_1 \tanh^2 \left[\kappa P_1 \left(\frac{l}{v_1} \right)^2 \right]^{1/2} \quad (6.19)$$

must be used. If the phasematching condition is not satisfied, Eq. (6.18) modifies to

$$P_2 = \kappa \left\{ P_1 \frac{l}{w_1} \text{sinc} (\Delta k l / 2) \right\}^2, \quad (6.20)$$

where Δk represents the momentum mismatch. In the above equations P_2 and P_1 are the powers inside the crystal. For an un-coated crystal we have to take into account surface reflections. Using the transformations $P_{2 \text{ out}} = P_2 [4n_2 / (n_2 + 1)^2]$ and $P_{1 \text{ out}} = P_1 [(n_1 + 1)^2 / 4n_1]$ where $P_{2 \text{ out}}$ and $P_{1 \text{ out}}$ are the powers outside the crystal, we obtain from the Eqs. (6.7) and (6.20) that

$$P_{2 \text{ out}} = \frac{128 \eta_0^3 \omega_1^2 d^2 P_{1 \text{ out}}}{(n_2 + 1)^2 (n_1 + 1)^4 \pi w_1^2} \frac{(e^{-\alpha_2 l / 2} - e^{-\alpha_1 l})^2 + 4e^{-(\alpha_2 / 2 + \alpha_1)l} \sin^2 \Delta k l / 2}{(\Delta k)^2 + (\alpha_2 / 2 - \alpha_1)^2} \quad (6.21)$$

In this last equation we have also included the optical absorption at the two frequencies. The only assumptions in Eq. (6.21) are weak focusing and moderate conversion efficiency.

(c) Second harmonic angular half-width

Provided that the absorption is not too large, the SHG output power from a crystal follows a sinc curve when the crystal rotates through the phasematching position [cf. Eqs. (6.20) and (6.21)]. Since the angular half-width depends on the crystal length, we can

use the observed width to determine an effective phasematching length which for a high quality crystal is equal to the crystal length. Variations in the indices of refraction, however, may make it impossible to satisfy the phasematching condition over the total crystal length, leading to a shorter phasematching length. Since $\text{sinc}^2 80^\circ \approx 0.5$, it follows that the angular half-width at the half power point is determined by

$$\frac{\Delta k(\theta)l}{2} = \frac{80 \times \pi}{180} . \quad (6.22)$$

Writing $\Delta k(\theta) = [\partial \Delta k(\theta) / \partial \theta] \Delta \theta$, we find that

$$\Delta k(\theta) = - \frac{4\pi}{\lambda_1} \frac{\partial n_1^e}{\partial \theta} \Delta \theta \quad (6.23)$$

for type I and

$$\Delta k(\theta) = - \frac{2\pi}{\lambda_1} \frac{\partial n_1^e}{\partial \theta} \Delta \theta \quad (6.24)$$

for type II phasematching in a positive birefringent crystal. We determine $\partial n_1^e / \partial \theta$ by differentiating Eq. (A.1) in Appendix A and find

$$\frac{\partial n^e(\theta)}{\partial \theta} = - n^e(\theta) \tan \rho . \quad (6.25)$$

By combining the Eqs. (6.22) to (6.25) we determine the internal angular half-width $\Delta \theta_{\text{int}}$. This must be related to the measured external half-width $\Delta \theta_{\text{ext}}$. When the laser is incident on the crystal at an

angle α to the normal, the internal angle β follows from the relation

$$n_1 \sin \beta = \sin \alpha . \quad (6.26)$$

If the crystal phasematches at this position, we immediately obtain by differentiation that

$$\frac{\Delta\theta_{\text{ext}}}{\Delta\theta_{\text{int}}} = n_1 \frac{\cos \beta}{\cos \alpha} . \quad (6.27)$$

For close to normal incidence this equation reduces to $\Delta\theta_{\text{ext}} = n_1 \Delta\theta_{\text{int}}$ and with this we find

$$\Delta\theta_{\text{I,ext}} = \frac{\lambda_1}{4.5l \tan \rho} \quad (6.28)$$

and

$$\Delta\theta_{\text{II,ext}} = \frac{\lambda_1}{2.25l \tan \rho} \frac{n_1^o + n_1^e(\theta)}{2n_1^e(\theta)} \quad (6.29)$$

for the two phasematching conditions. The half-widths are calculated in radians and we see that the type II phasematching half-width is twice the type I half-width.

In our experiments we have mixed $5.3 \mu\text{m}$ with $10.6 \mu\text{m}$ to generate $3.53 \mu\text{m}$ using type I phasematching. For this experiment the angular half-width is given by

$$\Delta\theta_{\text{I,ext}}^{5.3+10.6} = \frac{\lambda_1 [n_1^e(\theta) + n_2^e(\theta)]}{9l [n_2^e(\theta) \tan \rho_2 + 1/2 n_1^e(\theta) \tan \rho_1]} . \quad (6.30)$$

(d) Parametric oscillator threshold and bandwidth

When available, CdGeAs_2 is very useful as the nonlinear element in an infrared parametric oscillator because of the extensive tuning range and large nonlinear coefficient. In this section we list the equations which allow us to estimate the parametric oscillator threshold for doubly and singly resonant oscillators. In a doubly resonant oscillator (DRO) there is low loss both at the signal and the idler wave, whereas for a singly resonant oscillator (SRO) only one of the waves is resonant. The single pass gain of a degenerate parametric amplifier $\omega_s = \omega_i = \omega_p/2$ is equal to the second harmonic conversion efficiency P_2/P_1 into a Gaussian mode when the fundamental frequency is at $\omega_p/2$. We follow reference 5 and define $\omega_0 = \omega_p/2$, $\omega_s = \omega_0(1 + \delta)$, and $\omega_i = \omega_0(1 - \delta)$. For maximum parametric gain both the pump, signal, and idler wave should have the same confocal parameter such that $b_p = b_s = b_i$. This leads to a small signal gain G given by⁵

$$G = (\Gamma l)^2 = \kappa P_p l k_0 \bar{h} (1 - \delta^2)^2, \quad (6.31)$$

where κ is defined in Eq. (6.7) with $\omega_1 = \omega_0$. Further P is the pump power and the parameter δ tells how close the oscillator is to degenerate operation. The bar expresses that only the coupling into the Gaussian signal and idler mode should be included in the gain expression and at optimum focusing Eq. (6.14) gives a good approximation for \bar{h} . It is clear from Eq. (6.31) that the gain decreases when the

oscillator tunes away from degeneracy, leading to an increased pump threshold. With single pass power losses α_s and α_i at the signal and idler frequency the necessary pump power to reach DRO threshold is given by

$$G = \alpha_s \alpha_i, \quad (6.32)$$

and for SRO operation with no idler feedback ($\alpha_i = 1$) we have

$$G = 2\alpha_s. \quad (6.33)$$

These equations are strictly valid only for cw operation. For a Q-switched pump laser the threshold must be reached within a finite number of passes, and this requires some excess gain. Assuming a square pump pulse of length t_p and a cavity transit time t_0 the maximum number of available passes is $n = t_p/t_0$. Under these conditions it is easy to show that the DRO cw threshold condition modifies to⁴¹

$$\sqrt{G} = \alpha + \frac{\ln 10}{2n} \lg \left(\frac{P_n}{P_0} \right), \quad (6.34)$$

when the signal and idler wave has the same single pass power loss α . This equation gives the necessary gain for the oscillator to build up from the parametric fluorescence noise power P_0 at the signal or idler wavelength to a power P_n after n passes. We require some pump depletion and take P_n to be 10% of the pump power. Because of the logarithmic dependence the exact value of P_n/P_0 is not critical. As an example, for $P_n/P_0 \approx 10^{12}$, $t_p = 200$ nsec, and $t_0 = 0.2$ nsec

which corresponds to an effective cavity length of 6 cm, the equivalent loss due to buildup is 1.4%. Similarly for pulsed SRO operation we modify Eq. (6.33). Resonating the signal wave leads to⁴²

$$\lg(1 + G - 2\alpha_s) = \frac{1}{n} \lg \left(\frac{P_n}{P_0} \right), \quad (6.35)$$

assuming no loss in the crystal at the idler wavelength and also that $G - 2\alpha_s \ll 1$. The equation reduces to

$$G = 2\alpha_s + \frac{\ln 10}{n} \lg \left(\frac{P_n}{P_0} \right). \quad (6.36)$$

Using the same numerical example as before the necessary excess gain is 2.4%.

The frequency output of a parametric oscillator follows a sinc^2 ($\Delta k l / 2$) dependence where $\Delta k = k_p - k_s - k_i$ is the momentum mismatch. Assuming a single frequency pump, a change $\delta\omega_s (= -\delta\omega_i)$ in the signal frequency away from the phasematching solution leads to a momentum mismatch of⁴¹

$$\Delta k = b\delta\omega_s + \frac{1}{2} b_1 \delta\omega_s^2, \quad (6.37)$$

where

$$b = - \left(\frac{\partial k_s}{\partial \omega_s} - \frac{\partial k_i}{\partial \omega_i} \right) = - \frac{1}{c} \left\{ n_s - n_i - \lambda_s \frac{\partial n_s}{\partial \lambda_s} + \lambda_i \frac{\partial n_i}{\partial \lambda_i} \right\} \quad (6.38)$$

and

$$b_1 = \frac{\partial b}{\partial \omega_s} = - \frac{1}{2\pi c^2} \left\{ \lambda_s^3 \frac{\partial^2 n_s}{\partial \lambda_s^2} + \lambda_1^3 \frac{\partial^2 n_1}{\partial \lambda_1^2} \right\}. \quad (6.39)$$

We define the bandwidth by setting $|\Delta k l / 2| = \pi$. Except for operation close to the degeneracy point for type I phasematching or near the turning points of the angular tuning curves for type II phasematching we have $|4\pi b_1 / L b^2| < 1$ and by solving Eq. (6.37) for $\delta \omega_s$ we determine the full bandwidth $\Delta \omega_s$ at the base line. We find

$$\Delta \omega_s = \frac{1}{2} \left| \left(\frac{b}{b_1} \right) \left\{ \sqrt{1 + \frac{4\pi b_1}{L b^2}} - \sqrt{1 - \frac{4\pi b_1}{L b^2}} \right\} \right| \approx \left| \frac{4\pi}{L b} \right|. \quad (6.40)$$

For the special case that $|4\pi b_1 / L b^2| > 1$, the bandwidth is given by

$$\Delta \omega_s = \left| \frac{b}{b_1} \right| \sqrt{1 + \left| \frac{4\pi b_1}{L b^2} \right|} \approx \sqrt{\left| \frac{4\pi}{L b_1} \right|}. \quad (6.41)$$

2. Third Harmonic Generation

For an electron concentration of $5 \times 10^6 \text{ cm}^{-3}$ the III-V compounds InSb and InAs have very large third order nonlinear coefficients⁴³ with the main contribution to the nonlinearity arising from the non-parabolicity of the conduction band.⁴⁴ The magnitude is inversely proportional to the bandgap frequency and the effective mass squared and proportional to the carrier concentration. This makes CdGeAs₂

interesting because in addition to the small bandgap frequency and the small effective mass it has sufficient birefringence for phase-matching leading to the possibility of reasonably efficient THG. A determination of the various components of the susceptibility tensor may also provide an interesting check on the bandstructure calculation near $k = 0$. In this section we discuss phasematching and derive expressions for the effective nonlinear coefficient, conversion efficiency, and angular bandwidth for third harmonic generation (THG).

(a) THG phasematching and effective nonlinear coefficient

There are three possible ways to phasematch THG. For a crystal with positive birefringence the phasematching conditions can be written as⁴⁵

$$\begin{aligned} n_3^o &= n_1^e(\theta) \\ n_3^o &= \frac{1}{3} [2n_1^e(\theta) + n_1^o] \\ n_3^o &= \frac{1}{3} [n_1^e(\theta) + 2n_1^o] \end{aligned} \quad (6.42)$$

and we refer to them as respectively type I, II, and III phasematching. Type III requires the largest birefringence.

We use c_{ijkl} for the third order nonlinear coefficient. The definition follows from the equation

$$P_i = c_{ijkl} E_j E_k E_l \quad (6.43)$$

with summation over repeated indices and where as usual P and E stand for the generated nonlinear polarization and the electric field

amplitudes. The permutation symmetry between the last three indices suggests introduction of a contracted notation. The matrix c_{ijk} has 81 elements while the compact form c_{im} has only 30. The definition of m follows from Table XI.⁴⁵ For the $\bar{4}2m$ chalcopyrite symmetry the tensor c_{im} is given by

$$c_{im} = \begin{vmatrix} c_{11} & 0 & 0 & 0 & 0 & c_{16} & 0 & c_{18} & 0 & 0 \\ 0 & c_{11} & 0 & c_{16} & 0 & 0 & 0 & 0 & c_{18} & 0 \\ 0 & 0 & c_{33} & 0 & c_{35} & 0 & c_{35} & 0 & 0 & 0 \end{vmatrix} \quad (6.44)$$

The tensor has 5 independent elements or 4 when we use the Kleinman symmetry condition¹⁴ which gives $c_{35} = c_{16}$. In contracted form the Eq. (6.43) reduces to

$$P_i = c_{im} \epsilon_m, \quad (6.45)$$

where the vector ϵ_m is given by⁴⁵

$$\epsilon_m = \begin{vmatrix} \epsilon_{111} \\ \epsilon_{222} \\ \epsilon_{333} \\ \epsilon_{233} + \epsilon_{323} + \epsilon_{332} \\ \epsilon_{223} + \epsilon_{232} + \epsilon_{322} \\ \epsilon_{133} + \epsilon_{313} + \epsilon_{331} \\ \epsilon_{113} + \epsilon_{131} + \epsilon_{311} \\ \epsilon_{122} + \epsilon_{212} + \epsilon_{221} \\ \epsilon_{112} + \epsilon_{121} + \epsilon_{211} \\ \epsilon_{123} + \epsilon_{132} + \epsilon_{213} + \epsilon_{231} + \epsilon_{312} + \epsilon_{321} \end{vmatrix}, \quad (6.46)$$

TABLE XI

CONTRACTED NOTATION FOR THE THIRD ORDER NONLINEAR COEFFICIENT

ijk	1.1	222	333	233	223	133	113	122	112	123
m	1	2	3	4	5	6	7	8	9	0

and $\mathcal{L}_{ijk} = E_i(\omega_3)E_j(\omega_2)E_k(\omega_1)$. We use Eq. (6.45) together with the Eqs. (6.44) and (6.46) to determine the effective nonlinear coefficient for the three phasematching conditions. Let θ be the angle between the wavevector \bar{k}_1 and the z axis, φ the angle between the projection of \bar{k}_1 in the (x,y) plane and the x axis, and α the angle between the electric field \bar{E}_1 at the fundamental frequency and the normal to \bar{k}_1 in the (\bar{k}_1, z) plane (cf. Fig. 18). The effective nonlinear coefficient depends on the angles and we find

$$\left. \begin{aligned} \text{I: } P_3 &= -\frac{1}{4} (c_{11} - 3c_{18}) \sin(4\varphi) \cos^3 \theta E_1^3 \\ \text{II: } P_3 &= \left[\frac{1}{2} (c_{11} - 3c_{18}) \sin^2 2\varphi \cos^2 \theta + c_{16} \sin^2 \theta \right. \\ &\quad \left. + c_{18} \cos^2 \theta \right] \sin \alpha \cos^2 \alpha E_1^3 \\ \text{III: } P_3 &= \frac{1}{4} (c_{11} - 3c_{18}) \sin(4\varphi) \cos \theta \sin^2 \alpha \cos \alpha E_1^3 \end{aligned} \right\} \quad (6.47)$$

for the three phasematching conditions. In Eqs. (6.47) θ is fixed by the phasematching conditions in Eqs. (6.42). The two other angles, however, can be chosen to maximize the nonlinear interaction. The optimum values for φ and α are listed in Table XII together with the maximized effective nonlinear coefficient c as defined by $P_3 = cE_1^3$. Considering only the nonparabolic band contribution to the nonlinear coefficient we have for spherical bands that

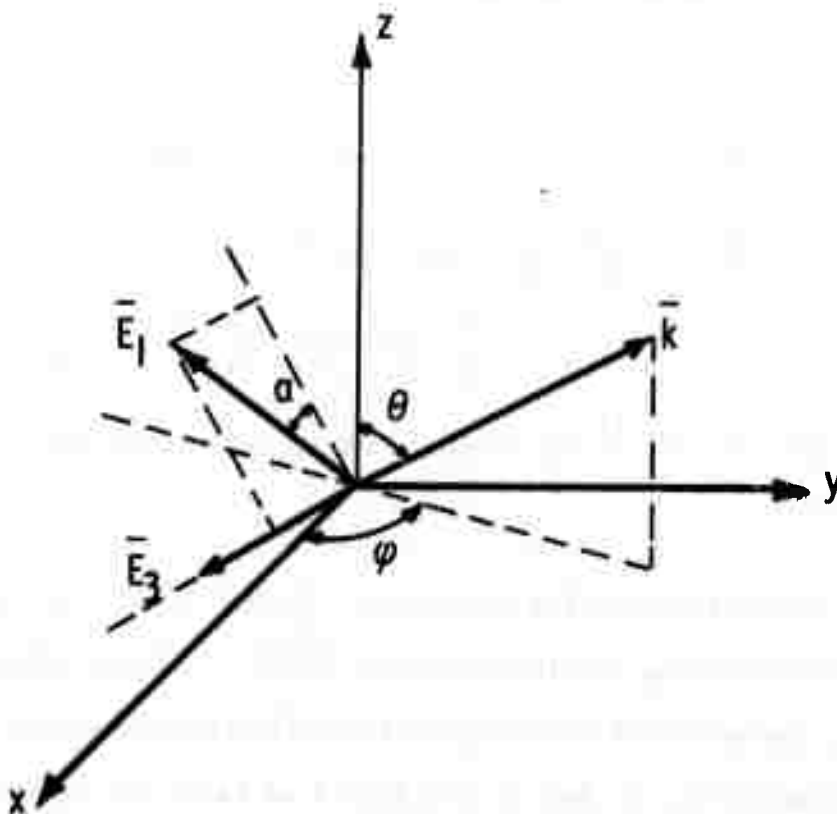


FIG. 18--Definition of the angles θ , φ , and α for third order optical interactions.

TABLE XII

MAXIMUM EFFECTIVE THIRD ORDER NONLINEAR COEFFICIENT

Phasematching condition	φ	α	Maximum effective nonlinear coefficient
Type I	$22.5^\circ + n \times 45^\circ$	0	$-\frac{1}{4} (c_{11} - 3c_{18}) \cos^2 \theta$
Type II	$45^\circ + n \times 90^\circ$	35.2°	$\frac{2}{3\sqrt{3}} \left[\frac{1}{2} (c_{11} - c_{18}) \cos^2 \theta + c_{16} \sin^2 \theta \right]$
Type III	$22.5^\circ + n \times 45^\circ$	54.8°	$\frac{1}{6\sqrt{3}} (c_{11} - 3c_{18}) \cos \theta$

$\frac{1}{3} c_{11} = c_{16} = c_{18}$. With this assumption the effective nonlinear coefficients in Table XII reduce to $c_I = c_{III} = 0$ and $c_{II} = (2/3\sqrt{3})c_{16}$. Since the chalcopyrites have fairly isotropic conduction bands, the most efficient third order interaction in n-type material probably occurs for type II phasematching.

(b) THG conversion efficiency and angular bandwidth

For weak focusing such that the crystal length l is smaller than the confocal parameter b_1 , the third harmonic conversion efficiency P_3/P_1 is given by

$$\frac{P_3}{P_1} = \frac{3}{n_3 n_1^3} (\eta_0^2 \omega_1 c l)^2 \left(\frac{P_1}{A_1} \right)^2 \text{sinc}^2 \left(\frac{\Delta k l}{2} \right), \quad (6.48)$$

where c is the effective nonlinear coefficient and $A_1 = \pi w_1^2/2 = \lambda_1 b_1/4n_1$ is the beam area. Equation (6.48) does not include reflection losses.

The sinc curve determines the angular half-width. Similar to the treatment of SHG we find that the angular half-widths at the half power point are given by

$$\left. \begin{aligned} \Delta\theta_{I,\text{ext}} &= \frac{\lambda_1}{6.75l \tan \rho} \\ \Delta\theta_{II,\text{ext}} &= \frac{\lambda_1}{4.5l \tan \rho} \frac{n_3^0}{n_1^e(\theta)} \\ \Delta\theta_{III,\text{ext}} &= \frac{\lambda_1}{2.25l \tan \rho} \frac{n_3^0}{n_1^e(\theta)} \end{aligned} \right\}. \quad (6.49)$$

3. Determination of Indices of Refraction

In order to determine accurately the phasematching conditions for a material, the dispersion and the birefringence must be known to better than one part in the third place. We measure the indices of refraction using a prism set of minimum deviation.⁴⁶ This is the best method when sufficiently large single crystals are available.

Figure 19 shows a diagram of the index of refraction measurement apparatus. The light source is either a laser or a globar for measurements at wavelengths longer than one micron. The detector is PbS out to three microns, and then a thermocouple at longer wavelengths. The crystal is mounted on a Gurley Unisec table which measures angles to one second of arc. In practice, diffraction effects due to the finite prism size limit the accuracy of the measured angles. With the collimated light filling a prism of length L , Fraunhofer diffraction limits the angular width of the focused beam at the detector to

$$\Delta\varphi = 2 \frac{\lambda f}{LR}, \quad (6.50)$$

where λ is the wavelength, R is the distance from the center of the table to the detector, and f is the focal length of the focusing optics. For our system we have $R = 23$ cm and $f = 15$ cm. Assuming the detector can be set to the maximum within five percent of the full angular width, we have for a 0.5 cm prism and a wavelength of $5 \mu\text{m}$ that the diffraction limits the accuracy of the measured angles to approximately 14 seconds of arc.

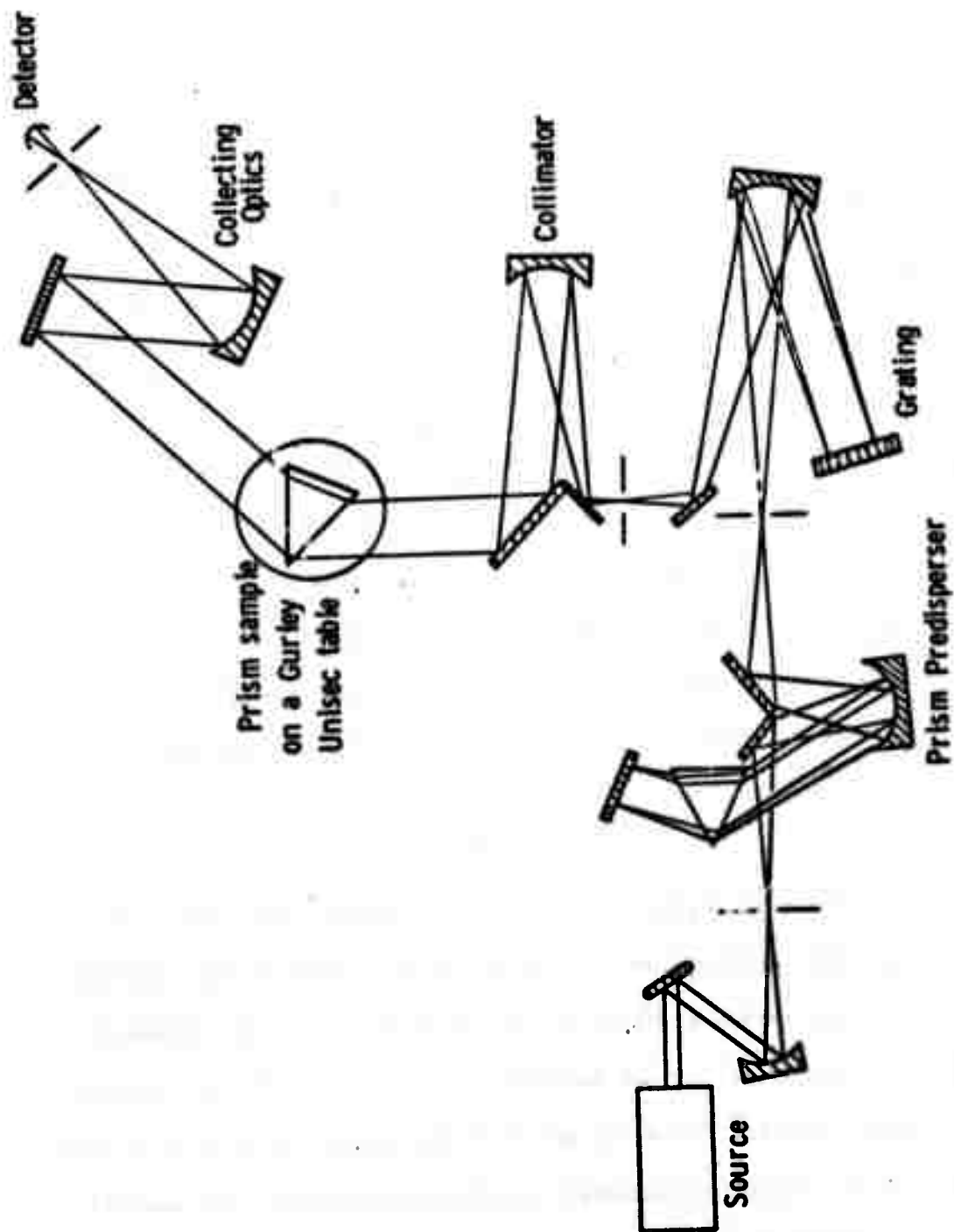


FIG. 19--Index of refraction measurement apparatus.

We calculate the indices of refraction from the equation

$$\frac{n}{n_{\text{air}}} = \frac{\sin\left(\frac{\alpha + \delta}{2}\right)}{\sin(\alpha/2)}, \quad (6.51)$$

where δ is the minimum deviation angle and α is the apex angle.

By differentiating Eq. (6.51) we obtain

$$\frac{\Delta n}{n} = \frac{1}{2} \cot \alpha \left(\frac{\alpha + \delta}{2} \right) \Delta \delta - \frac{1}{2} \frac{\sin(\delta/2)}{\sin(\alpha/2) \sin((\alpha + \delta)/2)} \Delta \alpha. \quad (6.52)$$

For our CdGeAs_2 and CdGeP_2 prisms we have $\delta \approx 35^\circ$ and $\alpha \approx 13^\circ$.

Substitution into Eq. (6.52) yields

$$\frac{\Delta n}{n} \approx 1.1 \Delta \delta - 3.3 \Delta \alpha, \quad (6.53)$$

where $\Delta \delta$ and $\Delta \alpha$ are in radians, and the uncertainty in the measured index values is

$$\Delta n = n \sqrt{(1.1 \Delta \delta)^2 + (3.3 \Delta \alpha)^2}. \quad (6.54)$$

Taking $\Delta \delta = \pm 1'$ and $\Delta \alpha = \pm 1'$ the uncertainty is $\Delta n = \pm 0.004$.

The absolute accuracy of the measured indices is probably not better than this since we worked with very small prisms. More important, however, is the relative accuracy which depends only on $\Delta \delta$. We expect this to be better than one part in the third place.

The sample temperature must be kept constant during the measurements. For CdGeAs_2 $dn/dt \sim 5 \times 10^{-4} \text{ } ^\circ\text{C}^{-1}$ at $3.39 \text{ } \mu\text{m}$. This means that a temperature rise of 2°C changes the indices by as much as one

part in the third place. The growth method and carrier concentration must also be specified. In semiconductors carrier concentration variations may change the indices of refraction significantly.⁴⁷

If large enough single crystals are not available for prism fabrication, other methods can be used to determine the birefringence of a crystal. One way is to use a laser to probe a wedged platelet between crossed polarizers. The laser beam is normal to the crystal and polarized 45° to the "effective" c-axis in the platelet plane. By translating the wedge a distance x across the beam, the power P at the detector is given by

$$P \sim \epsilon n^2 \left(\frac{\Gamma_e - \Gamma_o}{2} \right)^2, \quad (6.55)$$

where $\Gamma_e - \Gamma_o = (2\pi/\lambda)[n_e(\theta) - n_o] \times \tan \alpha$ is the phase difference between the extraordinary and the ordinary wave. Here θ as usual is the angle between the c-axis and the propagation direction and α is the wedge angle. If the distance between two power minima is x_o , then the equation

$$n_e(\theta) - n_o = \frac{\lambda}{x_o \tan \alpha} \quad (6.56)$$

determines the birefringence.

For very small samples not larger than 1 mm, the birefringence can be measured by rotating a platelet. This method, however, is not so reliable. With crossed polarizers and the laser polarized at 45°

to the "effective" c-axis, Eq. (6.55) still holds, and the phase difference is given by

$$\Gamma_e - \Gamma_o = \frac{2\pi l}{\lambda} [n_e(\theta) \cos \varphi_e - n_o \cos \varphi_o] , \quad (6.57)$$

where l is the plate thickness and Fig. 20 defines the angles.

Equation (6.57) can be written as

$$\Gamma_e - \Gamma_o = \frac{2\pi l}{\lambda} \left[\sqrt{n_e(\theta)^2 - \sin^2 \varphi} - \sqrt{n_o^2 - \sin^2 \varphi} \right]. \quad (6.58)$$

To obtain an approximate expression we use Eq. (A.2) in Appendix A and take $n_o^2 \gg \sin^2 \varphi$. This gives

$$\Gamma_e - \Gamma_o \approx \frac{2\pi l}{\lambda} \Delta n \sin^2 \theta \left(1 + \frac{1}{2} \frac{\sin^2 \varphi}{n_o^2} \right) , \quad (6.59)$$

where Δn is the birefringence. When the rotation is around the axis normal to the "effective" c-axis, θ is related to the external angle φ by $\theta = \pi/2 + \varphi - \eta$ where η is the angle between the c-axis and the platelet plane. By measuring the external angle difference between two power minima, we use Eq. (6.55) together with Eq. (6.58) or (6.59) to calculate the birefringence.

The measured index data can be fit to a classical Sellmeier equation of the form

$$n^2 = A + \frac{B}{1 - (D/\lambda)^2} + \frac{C}{1 - (E/\lambda)^2} , \quad (6.60)$$

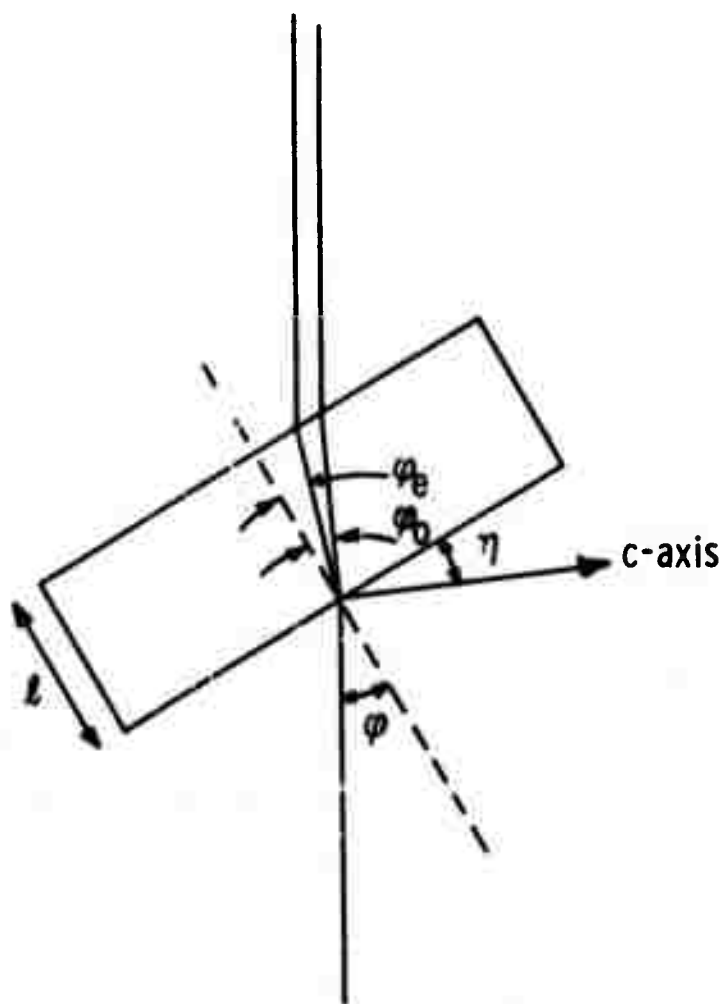


FIG. 20--Determination of the birefringence by the platelet method.

which holds in the transparent region of the crystal not too close to the absorption bands. In this equation E is approximately the reststrahl wavelength and D corresponds to an average electronic bandgap wavelength. From Eq. (6.60) we estimate the DC dielectric constant by letting $\lambda \rightarrow \infty$. This gives

$$\epsilon_{DC} = A + B + C \quad . \quad (6.61)$$

4. Measurement Technique for the Optical Nonlinear Coefficient

There are several ways to measure the optical nonlinear coefficients.⁴⁸ We have used the wedged sample technique¹¹ which is most convenient for relative measurements. Translation of the wedged nonlinear crystal across the laser beam results in oscillations in the SHG output power. Taking s as integer, maxima occur every time the effective crystal thickness is equal to $2s + 1$ times the coherence length l_c which for SHG is defined as

$$l_c = \frac{\pi}{\Delta k} = \frac{\lambda_1}{4(n_2 - n_1)} \quad . \quad (6.62)$$

The wedge method is very similar to the Maker's fringe technique,⁴⁹ but it has some advantages. The Maker's fringe technique is only useful when the crystal length $l > (2n)^2 l_c$, and the method therefore requires large samples of materials with large indices of refraction and a large coherence length when only small samples are available. The wedge technique does not have this limitation.

Thin samples may be used and the absorption can therefore most often be neglected. The wedge technique also avoids problems of multiple reflections and resonance. The fraction of the SHG power that suffers multiple reflections is transmitted in different directions and can be stopped by proper aperturing. By mounting the wedge such that the incident laser beam is normal to the crystal surface, there is no mode distortion due to refraction as it will be with the Maker's fringe technique.

Equation (B.5) in Appendix B gives the SHG output power generated in a wedged sample. Neglecting the absorption the equation reduces to

$$P_{2out} = \frac{128 \eta_0^3 \omega_1^2 d^2 P_{1out}^2}{(n_2 + 1)^2 (n_1 + 1)^4 \pi w_1^2} \left\{ \frac{1 - \cos(\Delta k l_0) \exp \left[- \left(\frac{w_1 \Delta k \tan \alpha}{4} \right)^2 \right]}{(\Delta k)^2 / 2} \right\} \quad (6.63)$$

which agrees with reference 50. We determine the coherence length

$l_c = \pi / \Delta k$ by translating the crystal a distance y_0 between two SHG minima. This gives

$$l_c = \frac{1}{2} y_0 \tan \alpha \quad . \quad (6.64)$$

The expression inside the parenthesis in Eq. (6.63) reduces to the standard

$$\left\{ l_0 \operatorname{sinc} \left(\frac{\Delta k l_0}{2} \right) \right\}^2$$

form when

$$\left(\frac{w_1 \Delta k \tan \alpha}{4} \right)^2 = \left(\frac{\pi w_1}{2y_0} \right)^2 \ll 1.$$

This condition is never difficult to satisfy and neglecting the exponential we have

$$P_{2out} = \frac{128 \eta_0^3 \omega_1^2 d_1^2 P_{1out}^2}{(n_2 + 1)^2 (n_1 + 1)^4 \pi w_1^2} \left\{ \frac{2}{\pi} l_c \sin \frac{\pi}{2} \frac{l_0}{l_c} \right\}^2. \quad (6.65)$$

We measure the relative effective nonlinear coefficient by using a reference sample and comparing the coherence lengths and the maximum SHG output powers for a given input power.

5. Absorption Mechanisms

A maximum optical power density in the material eventually limits the efficiency of nonlinear optical processes. Different mechanisms may be responsible such as nonlinear absorption, broken phasematching condition due to induced index of refraction inhomogeneities, or permanent crystal damage. Both the broken phasematching condition and the crystal damage are often caused by the local heating due to the optical absorption, and it is therefore important to reduce the absorption to a minimum. Some of the most common absorption mechanisms are:

- 1) Bandgap absorption,
- 2) Two-phonon absorption,

- 3) Three-phonon absorption,
 - 4) Free electron scattering; in n-type semiconductors,
 - 5) Free hole scattering
 - 6) Intra band absorption
- } in p-type semiconductors,
- 7) Impurity and defect absorption,
 - 8) Free carrier absorption generated by impurity or defect absorption,
 - 9) Two-photon absorption,
 - 10) Free carrier absorption generated by two-photon absorption.

As discussed earlier the direct or indirect bandgap absorption determine the short wavelength cutoff and two-phonon absorption limits the transmission at long wavelengths. In CdGeAs_2 the two-phonon absorption is approximately 20 cm^{-1} . Some weak three-phonon absorption exists at wavelengths roughly two thirds of the two-phonon cutoff and in CdGeAs_2 the magnitude is approximately 0.3 cm^{-1} at $12 \mu\text{m}$.

The free carriers in a semiconductor affect both the indices of refraction and the absorption. According to classical Drude-Zener theory the free carrier contribution to the relative dielectric constant ϵ at frequency ω is given by.⁵¹

$$\epsilon = \epsilon_{\infty} \left[1 - i \frac{\omega_p}{\omega} \frac{\omega_p \tau}{1 + i\omega\tau} \right], \quad (6.66)$$

where ϵ_{∞} is the optical relative dielectric constant without the carrier contribution, ω_p the plasma frequency, and τ the carrier collision time. For a carrier density N and an effective mass m^* ,

the plasma frequency is given by

$$\omega_p = \sqrt{\frac{N_0^2}{m \epsilon_0 \epsilon_\infty}} . \quad (6.67)$$

In the visible and near infrared where $\omega \gg \omega_p$ and $1/\tau$, it follows from Eq. (6.66) that the indices of refraction n and the free carrier absorption constant a can be written as

$$n = n_\infty \left[1 - \frac{1}{2} (\omega_p/\omega)^2 \right] \quad (6.68)$$

and

$$a = \frac{n_\infty^2 \omega_p^2}{c \tau \omega^2} . \quad (6.69)$$

In crystals with an anisotropic effective mass tensor, the presence of carriers changes the birefringence. Assuming a single band extrema at $k = 0$, the free carrier induced change in the birefringence is found from Eqs. (6.67) and (6.68) to be

$$n_{\parallel} - n_{\perp} = n_{\parallel,\infty} - n_{\perp,\infty} - \frac{Ne^2}{2\epsilon_0 \omega^2} \left[\frac{1}{n_{\parallel,\infty} m_{\parallel}} - \frac{1}{n_{\perp,\infty} m_{\perp}} \right] . \quad (6.70)$$

We refer to this expression in Section A.6 of this chapter and discuss how to use this effect in CdGeAs_2 to construct a modulator.

According to Eq. (6.69), the free carrier absorption increases with the square of the wavelength. This result assumes an energy independent collision time which often is not the case. More generally,

we can write $a \propto \lambda^n$ where the exponent depends on which scattering mechanism limits the collision time. Scattering by acoustical phonons gives 1.5,⁵² and scattering by optical phonons gives 2.5.⁵³ For ionized impurity scattering, the exponent is between 3.0 and 3.5,⁵⁴ depending on which approximation is used. For CdGeAs₂ we have measured a 3.5 dependence for n-type material (cf. CH. VI.B.5). The absorption is therefore determined by ionized impurity scattering and the absorption cross section σ_{abs} follows from the equation⁵⁴

$$\sigma_{abs} = a/N_{el} = \frac{16\sqrt{2}\pi^2}{3} \left(\frac{ze^2}{4\pi\epsilon_0\epsilon_{DC}} \right)^2 \frac{e^2 N_i \hbar^2}{4\pi\epsilon_0 n_{\infty} c(m^*)^{3/2}} \left(\frac{1}{\hbar\omega} \right)^{3.5}, \quad (6.71)$$

where N_i is the density of ionized impurities. The derivation of Eq. (6.71) assumes an isotropic effective mass, but the expression still can be used to estimate the ionized impurity density in CdGeAs₂ since the conduction band is not too anisotropic.

In p-type CdGeAs₂ we see no evidence of free hole absorption. The absorption has a more complicated wavelength dependence due to intra band transitions between the split valence bands. This absorption also occurs in p-type germanium⁵⁵ and the III-V compounds.⁵¹ We refer to the results of Chapter III to determine the magnitude and spectral dependence of the intra band absorption in p-type CdGeAs₂. The absorption constant at the frequency ω for transitions between the v_1 band to the v_2 or v_3 band is^{55,56}

$$a_{i,1} = \frac{e^2}{4\pi\epsilon_0 m^2 c} \frac{1}{n_{\infty} \omega \pi} \frac{p}{N_{v_1}} (1 - e^{-\hbar\omega/kT}) \int |M|^2 e^{E_i/kT} \delta(E_1 - E_i - \hbar\omega) d^3k, \quad (6.72)$$

where $i = 2$ or 3 refers to the two lower valence bands, m is the free electron mass, p is the hole density, and N_{v1} is defined in Eq. (4.9). The integration is over the crystal momentum with $k = k_1 = k_i$. Further the matrix element M is given by

$$|M|^2 = |\langle \psi_{v1}^A | \hat{e} \cdot \vec{p} | \psi_{v1}^A \rangle|^2 + |\langle \psi_{v1}^A | \hat{e} \cdot \vec{p} | \psi_{v1}^B \rangle|^2, \quad (6.73)$$

and the energy E_1 of the v_1 band is measured relative to the band extrema such that

$$E_1 = -\frac{\hbar^2}{2} \left[\frac{k_{\perp}^2}{m_{1,\perp}} + \frac{k_{\parallel}^2}{m_{1,\parallel}} \right]. \quad (6.74)$$

We evaluate the integral in Eq. (6.72) in Appendix C. Equation (3.24) gives the matrix elements for the intra band transitions. By combining Eq. (3.24) with Eqs. (C.3), (C.12), (C.13), and (6.72) we calculate the absorption constant letting $e_x^2 = e_y^2 = e_z^2 = \frac{1}{3}$. The expression for the absorption constant depends on only four parameters: the band-gap energy, the spin-orbit coupling, the crystal field splitting, and the matrix element P . With the values in Table II and Eq. (3.20), the absorption constants for CdGeAs_2 at a carrier concentration of $2 \times 10^{16} \text{ cm}^{-3}$ can be written

$$a_{2,1} = \frac{1}{\hbar\omega} [1 - \exp(-\hbar\omega/kT)] (0.616 - 0.936 \text{ eV}/kT) \exp(0.088 \text{ eV}/kT) \quad (6.75)$$

$$a_{3,1} = \frac{1}{\hbar\omega} [1 - \exp(-\hbar\omega/kT)] (1.85 - 2.62 \text{ eV}/kT) \exp(0.171 \text{ eV}/kT) \quad (6.76)$$

where $\epsilon = \Delta E - \hbar\omega < 0$ and ΔE is the band splitting energy. For the $v_1 - v_2$ transition we have $\Delta E = 0.20$ eV and for the $v_1 - v_3$ transition $\Delta E = 0.52$ eV. Similarly, when $\epsilon > 0$ we obtain

$$a'_{2,1} = \frac{4.54}{\hbar\omega} [1 - \exp(-\hbar\omega/kT)] \sqrt{300 \epsilon/T} \exp(-\epsilon/kT) + a_{2,1} [1 - \operatorname{erf}(\sqrt{1.11 \epsilon/kT})] \quad (6.77)$$

and

$$a'_{3,1} = \frac{13.6}{\hbar\omega} [1 - \exp(-\hbar\omega/kT)] \sqrt{300 \epsilon/T} \exp(-1.05 \epsilon/kT) + a_{3,1} [1 - \operatorname{erf}(\sqrt{1.09 \epsilon/kT})] \quad (6.78)$$

where $a_{2,1}$ and $a_{3,1}$ are given by the same expressions as the $\epsilon < 0$ absorption constants in Eqs. (6.75) and (6.76). Figure 21 shows the wavelength dependence of the combined absorption constants for the two intra band transitions at three different temperatures. For a carrier concentration of $2 \times 10^{16} \text{ cm}^{-3}$ there is significant absorption within the normally transparent frequency range. The long wavelength cutoff of 0.20 eV corresponds to the calculated splitting energy between the v_1 and v_2 band. In the experimental section of this chapter we compare measured and calculated absorption. The observed absorption cut-off provides an experimental value for band splitting energy.

Absorption also occurs due to impurities and defects and the structure of the intraband absorption is therefore often obscured. Defects such as lattice vacancies have an effect similar to impurities. They give rise to acceptor and donor levels and optical absorption

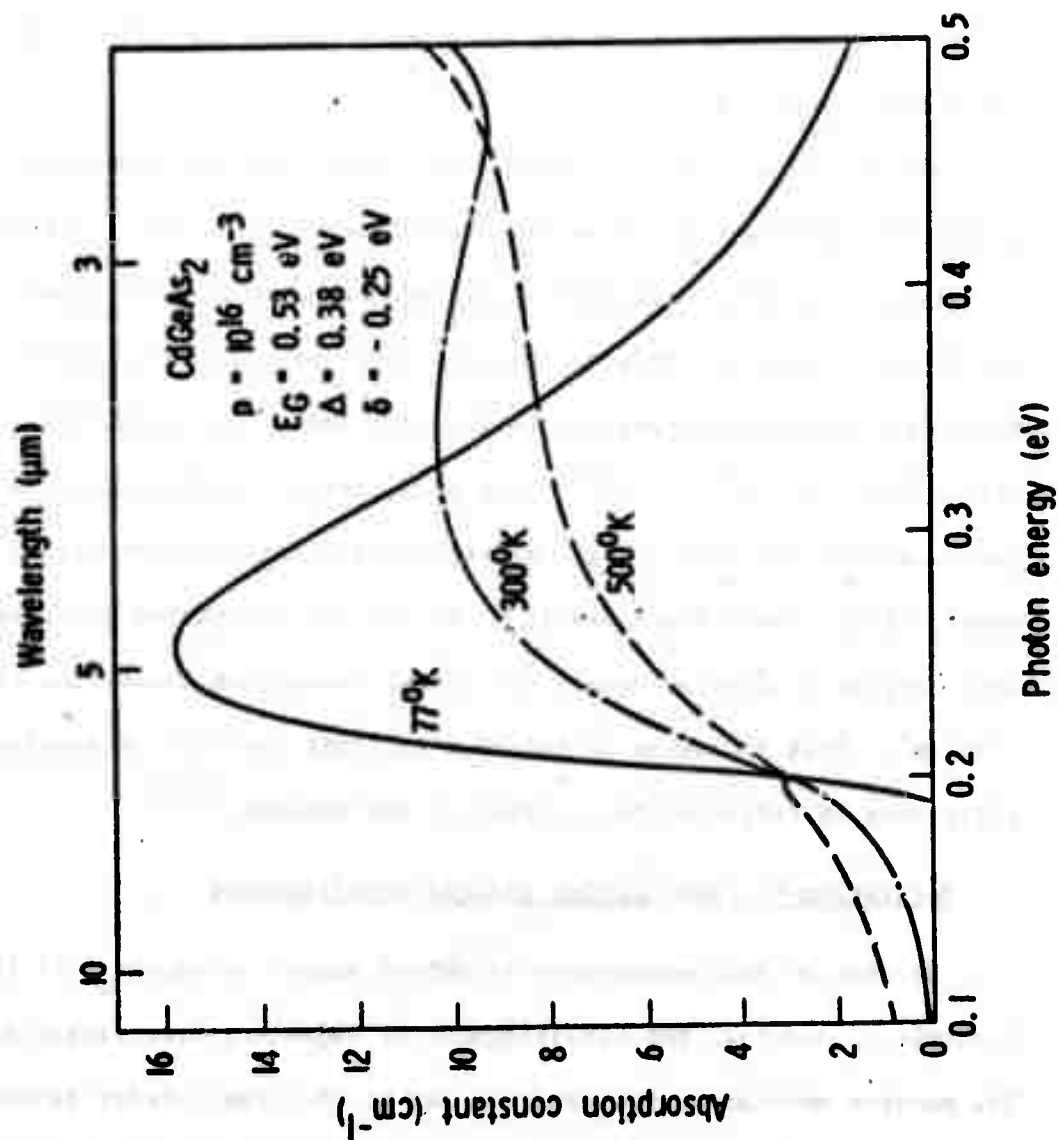


FIG. 21--Calculated total absorption coefficient for transistors between the split valence bands in p-type CdGeAs_2 at three different temperatures but assuming a constant carrier concentration.

is possible between these levels and the valence or conduction band. If the impurity levels are ionized by photon absorption, the resulting carriers lead to additional free carrier absorption. This is a nonlinear absorption mechanism which is important at high optical power densities. In some materials nonlinear absorption leads to saturation in the nonlinear conversion efficiency before the optical damage threshold is reached.

Two-photon absorption between the valence and the conduction band is another important nonlinear absorption mechanism. For a parametric oscillator, the pump frequency should be chosen to be less than half the bandgap frequency to avoid two-photon absorption. The measured two-photon absorption constant in GaAs and InP is approximately $0.1 \text{ cm}^{-1}/\text{MW cm}^{-2}$ at $1.06 \text{ }\mu\text{m}$.⁵⁷ The free carriers generated by two-photon absorption lead to an absorption constant proportional to the square of the laser power density. In InP the two-photon generated free carrier absorption equals the normal two-photon absorption at 2 MW/cm^2 . This mechanism is believed to limit the $10.6 \text{ }\mu\text{m}$ doubling efficiency in tellurium to, at best, a few percent.^{58,59}

6. Modulation by Free Carrier Induced Birefringence

Because of the anisotropic effective masses in CdGeAs_2 , it is possible to modulate the birefringence by injecting free carriers. The maximum modulation frequency is set by the free carrier recombination time. Increasing the carrier concentration by ΔN changes the birefringence by $\delta(\Delta n)$ which, according to Eq. (6.70), may be

written as

$$\delta(\Delta n) = - \frac{\Delta N e^2}{2\epsilon_0 \omega^2} \left[\left(\frac{1}{m_{\parallel,c}} + \frac{1}{m_{\parallel,v_1}} \right) \frac{1}{n_{\parallel,\infty}} - \left(\frac{1}{m_{\perp,c}} + \frac{1}{m_{\perp,v_1}} \right) \frac{1}{n_{\perp,\infty}} \right], \quad (6.79)$$

assuming the injection generates equal numbers of holes and electrons. We consider modulation at the 10.6 μm CO_2 laser wavelength. At this wavelength the CdGeAs_2 crystal is transparent without any absorption due to intraband transitions between the valence bands. With the values for the effective masses in Table II, we find

$$\delta(\Delta n) = - \Delta N \times 5.5 \times 10^{-19} \text{ (cm}^3\text{)}. \quad (6.80)$$

The necessary change in the birefringence to change the electric field polarization by 90° in a crystal with length l is given by

$$\delta(\Delta n) = \frac{\lambda}{2l}. \quad (6.81)$$

This corresponds to 100% modulation when the crystal is inserted between crossed polarizers. For a 2 mm crystal the necessary injected carrier concentration is $\Delta N = 5 \times 10^{15} \text{ cm}^{-3}$. This technique is a novel way to modulate a CO_2 laser. It requires a material with light and anisotropic effective masses such as CdGeAs_2 .

B. EXPERIMENTAL RESULTS

1. Indices of Refraction and Tuning Curves

(a) CdGeAs₂

We have measured the indices of refraction out to 10.6 μm using a 4 mm long by 3 mm high prism with an apex angle of 13 degrees. The prism was cut from boule No. 16. This boule was grown with 0.5 Wt% excess arsenic. Table XIII lists the indices of refraction for p-type material. CdGeAs₂ has a positive birefringence of about 0.1. For the 3.39 μm and the 10.6 μm points we used laser sources. The other points were taken with a globar light source. Because of the small prism size, the amount of refracted light from the globar was too small for the thermocouple detector at wavelengths longer than five microns.

A computer fit to the Sellmeier expression in Eq. (6.60) gives the results

$$n_o^2 = 4 + \frac{8.891}{1 - \left(\frac{0.5524}{\lambda}\right)^2} + \frac{1.886}{1 - \left(\frac{36}{\lambda}\right)^2} \quad (6.82)$$

and

$$n_e^2 = 4 + \frac{9.521}{1 - \left(\frac{0.6847}{\lambda}\right)^2} + \frac{1.909}{1 - \left(\frac{36}{\lambda}\right)^2} \quad (6.83)$$

for the ordinary and extraordinary indices. In these expressions the

TABLE XIII

MEASURED INDICES OF REFRACTION FOR CdGeAs_2

λ [μm]	n_e	n_o	$n_e - n_o$
2.88	3.7525	3.6358	0.1167
3.39	3.7285	3.6208	0.1077
4.0	3.7134	3.6124	0.1010
4.43	3.7053	3.6062	0.0991
5.06	3.6953	3.5992	0.0961
10.6	3.6578	3.5688	0.0890

long wavelength resonance was fixed at $36 \mu\text{m}$ which is the measured reststrahlen frequency. Figure 22 shows a plot of the indices of refraction. We estimate the low frequency dielectric constant from Eq. (6.61) and find

$$\left. \begin{aligned} \epsilon_{\perp} &= 14.8 \\ \epsilon_{\parallel} &= 15.4 \end{aligned} \right\} \quad (6.84)$$

It is also important to know the temperature dependence of the dispersion and the birefringence. If the phasematching condition is temperature sensitive, it is possible to tune without crystal rotation avoiding annoying alignment problems. For some applications the temperature sensitivity may prove a disadvantage. When the crystal has a slight absorption, the resulting nonuniform temperature distribution may make it impossible to satisfy the phasematching condition over the whole crystal length. We have measured the temperature dependence of the birefringence of CdGeAs_2 at $3.39 \mu\text{m}$ and $10.6 \mu\text{m}$. The crystal was inserted into an oven between crossed polarizers, and the incident light was polarized at 45° to the c-axis. By counting the fringes in the detected signal we determined the temperature dependence of the birefringence. With a temperature raise ΔT resulting in m fringes, we obtain

$$\frac{d(\Delta n)}{dT} = \frac{\lambda m}{l \Delta T} - \Delta n \alpha, \quad (6.85)$$

where $\Delta n = n_e - n_o$ is the birefringence, l is the crystal length,

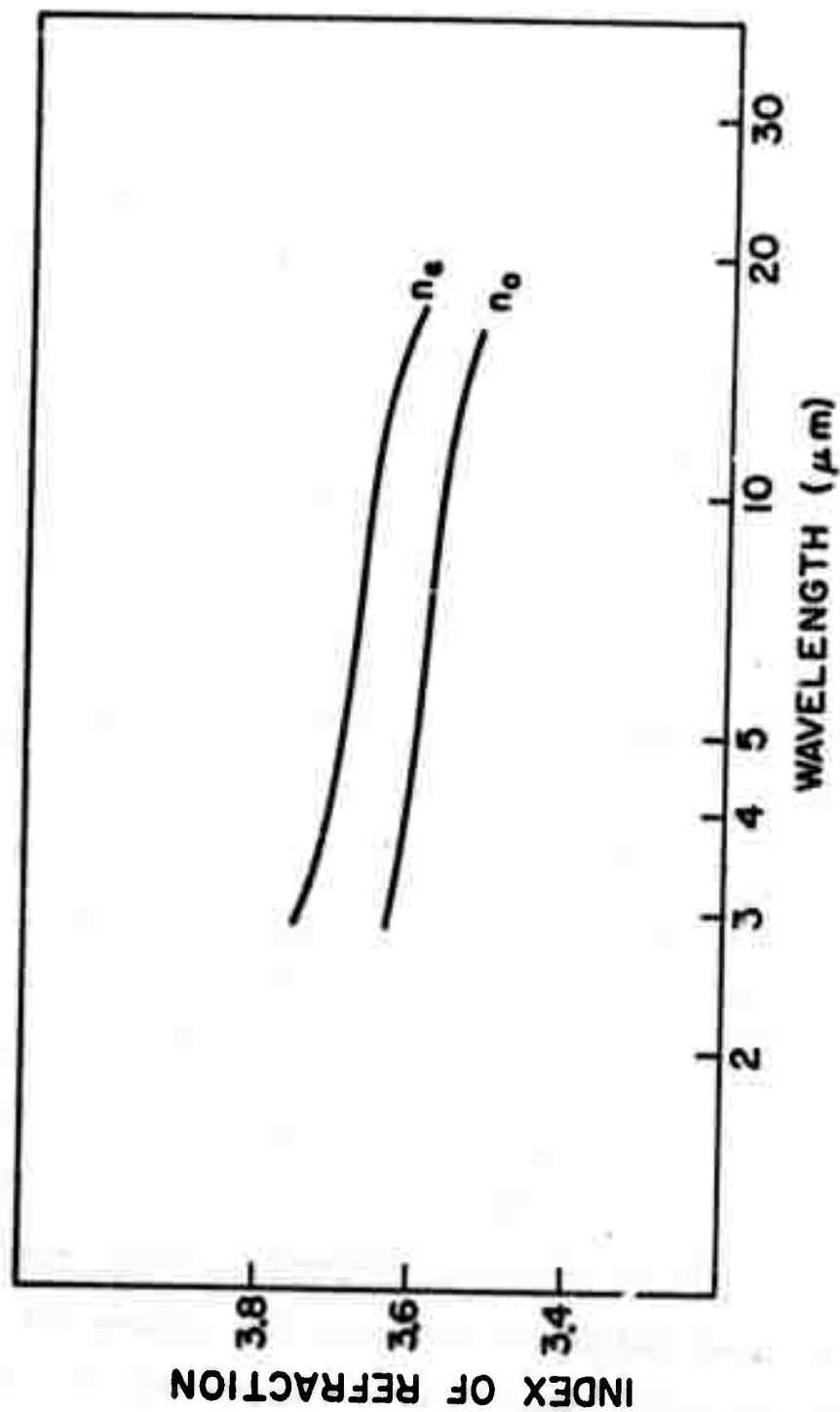


FIG. 22--Index of refraction for CdGeAs₂

and α is the a-axis linear thermal expansion coefficient (cf. Fig. 10). At 10.6 μm α gives approximately a 2% correction. The crystal we used was 2.96 mm long and it was cut from boule No. 28. Table XIV lists the measured $\frac{d(\Delta n)}{dT}$ results and Fig. 23 shows how the birefringence changes with temperature at 3.39 μm . We have also measured the temperature dependence of the absolute indices of refraction at 3.39 μm . We heated the prism slightly above room temperature and measured the change in the indices as the prism cooled off. These results are also listed in Table XIV. We see from the table, that the temperature dependence of the birefringence is very large for CdGeAs_2 and it comparable to the values for LiNbO_3 .⁶⁰

TABLE XIV
TEMPERATURE DEPENDENCE OF THE INDICES OF REFRACTION FOR CdGeAs_2

λ (μm)	T ($^{\circ}\text{C}$)	dn_e/dT ($10^{-4} \text{ }^{\circ}\text{C}^{-1}$)	dn_o/dT ($10^{-4} \text{ }^{\circ}\text{C}^{-1}$)	$d(\Delta n)/dT$ ($10^{-4} \text{ }^{\circ}\text{C}^{-1}$)	Method
10.6	~125			0.389	fringes
3.39	100			0.772	fringes
3.39	170			0.833	fringes
3.39	35	5.3	4.3	~ 1	prism

As discussed earlier, the presence of free carriers perturbs the indices of refraction. The prism we used for the indices of refraction measurements was p-type, but we did not measure the carrier concentration.

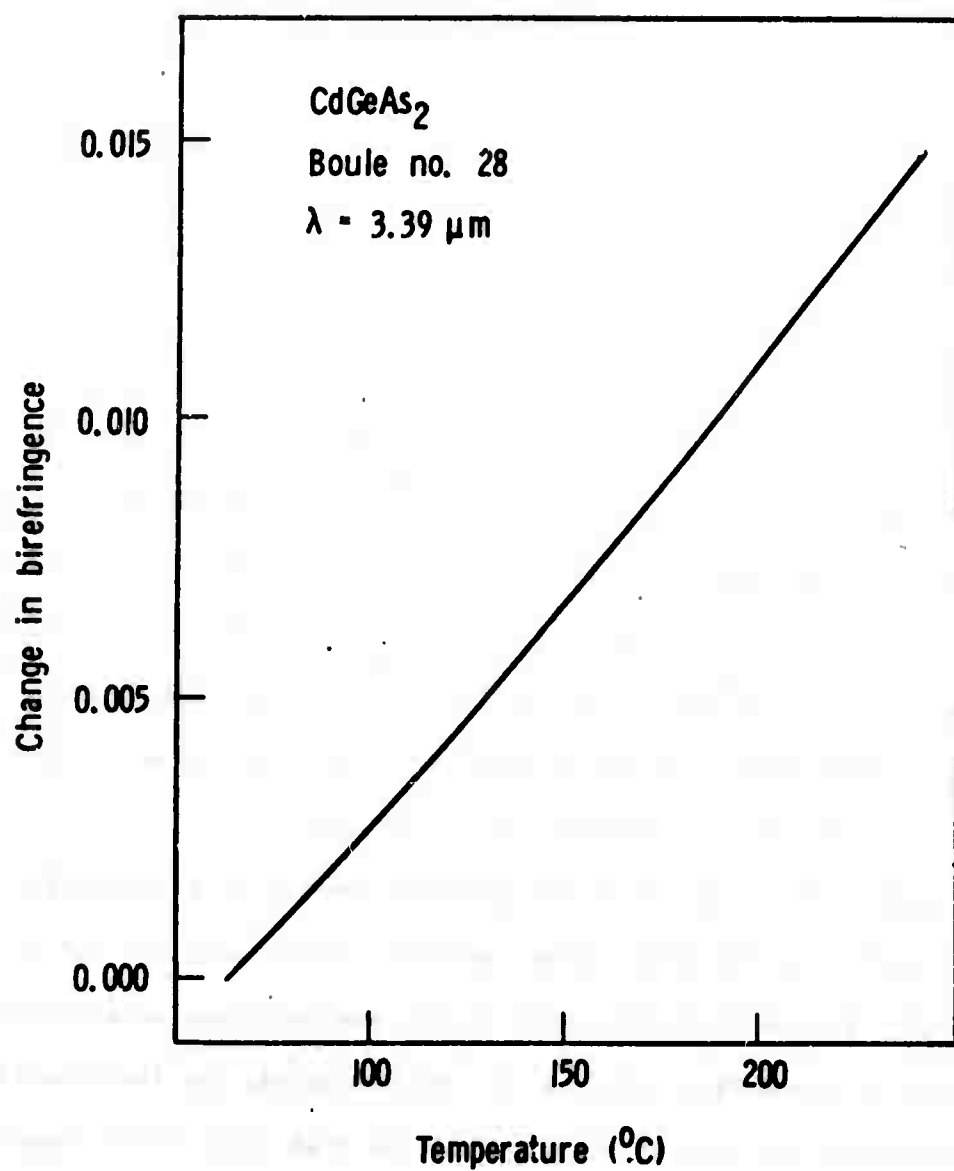


FIG. 23--Temperature dependence of the birefringence in CdGeAs₂ at 3.39 μm .

It was probably between 10^{15} and 10^{16} cm^{-3} . Equation (6.70) gives the induced birefringence due to free carriers. With

$$r_0 = \frac{e^2}{4\pi\epsilon_0 mc^2} = 2.818 \times 10^{-13} \text{ cm}$$

we find

$$\Delta n_{\text{carrier}} = - \frac{N \lambda^2 m r_0}{2\pi} \left(\frac{1}{n_{\parallel, \infty}^{m_{\parallel}}} - \frac{1}{n_{\perp, \infty}^{m_{\perp}}} \right). \quad (6.86)$$

Since $m_{\perp} > m_{\parallel}$ both for the conduction band and the top valence band, the birefringence decreases with increasing carrier concentration both in n- and p-type material. For a hole concentration of 10^{16} cm^{-3} we have $\Delta n_{\text{carrier}} = -0.004$ at $10.6 \text{ } \mu\text{m}$. The indices are also affected by the intraband transitions between the valence bands, and it is important to keep these effects in mind when comparing the measured indices of refraction of different CdGeAs_2 crystals.

In CdGeAs_2 phase-matched second harmonic generation is possible between 5 and $18 \text{ } \mu\text{m}$ for type I phase matching and between 5.4 and $13 \text{ } \mu\text{m}$ for type II. Figure 24 shows a plot of the phase-matching angle versus wavelength. For doubling with the SHG crystal inside the laser cavity, type I phase-matching is most useful since, in that case, the fundamental wave is polarized along one of the optical axis. For type II this is not possible and the crystal birefringence causes polarization rotation.

Since the walk-off angle limits the maximum useful interaction length, [cf. Eq. (6.15)], the most attractive parametric oscillator

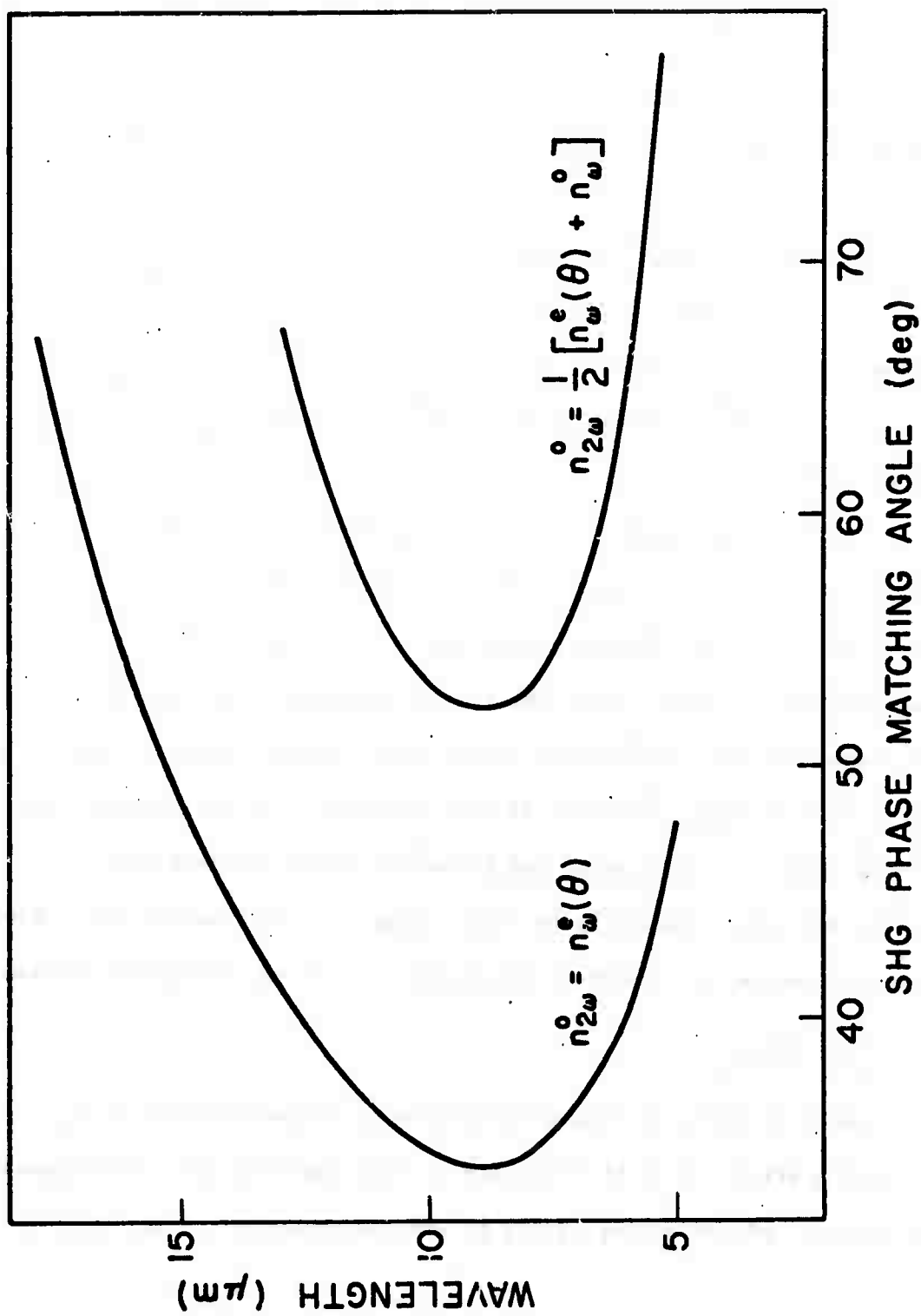


FIG. 24--Type I and type II phasematching angles for SHG in CdGeAs₂

construction would be a 90° phasematched oscillator with a tunable pump. Figure 25 shows the calculated tuning curve for such a device.

Parametric tuning by crystal rotation is possible over almost the whole transmission range of CdGeAs_2 . Figures 26(a) and 26(b) show tuning curves for several pump wavelengths. A single crystal can scan approximately 20 degrees. The walk-off angle for the extraordinary wave is typically about one degree. The curve for $\lambda_p = 4 \mu\text{m}$ in Fig. 26(a) represents an interesting special case where parametric tuning is possible between 6 and $13 \mu\text{m}$ without changing the crystal position. The large phasematching bandwidth might be useful in short pulse work.

A doubled CO_2 laser is a useful pump source for CdGeAs_2 since the $5.3 \mu\text{m}$ wavelength is slightly less than half the bandgap frequency and therefore avoids two-photon absorption. Figures 27(a) and 27(b) show the calculated tuning curves for the two phasematching conditions. The bandwidth over most of the tuning range varies between 10 and 20 cm^{-1} for a 1 cm crystal. For type II phasematching it is possible to tune through the degeneracy point and to make a choice between fast tuning and large bandwidths or slow tuning and small bandwidths. Note that the curves cover the very important 8 to $13 \mu\text{m}$ atmospheric window.

(b) CdGeP_2

Table XV lists the measured indices of refraction for CdGeP_2 . We used a prism 3.5 mm by 2 mm with an apex angle of 14° . The crystal was n-type and had a resistivity of approximately $10^5 \Omega\text{-cm}$. We

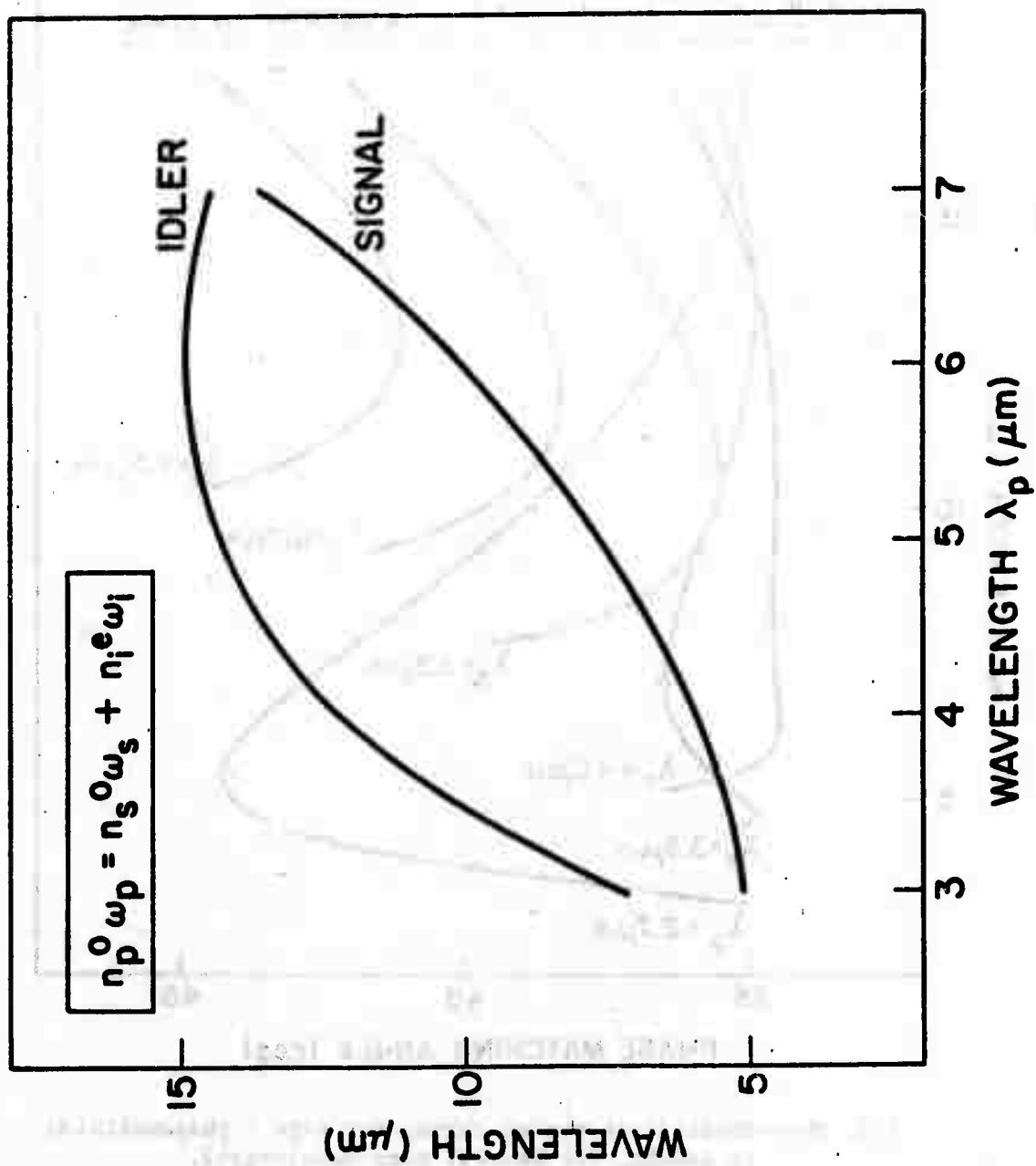


FIG. 25--Theoretical tuning curves for CdGeAs₂ for 90° type II phase matching.

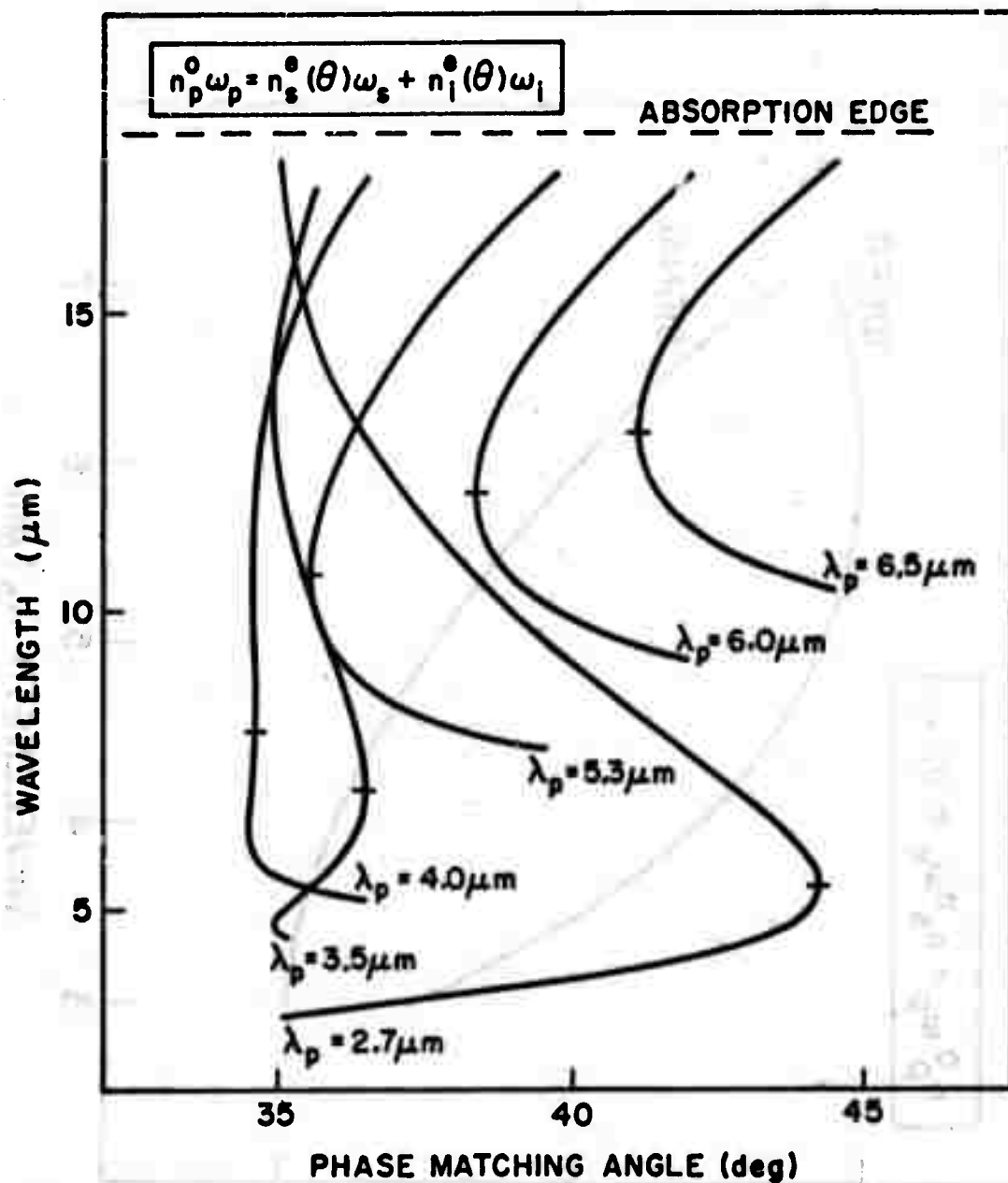


FIG. 26a--Theoretical tuning curves for type I phasematching in CdGeHs_2 for several pump wavelengths.

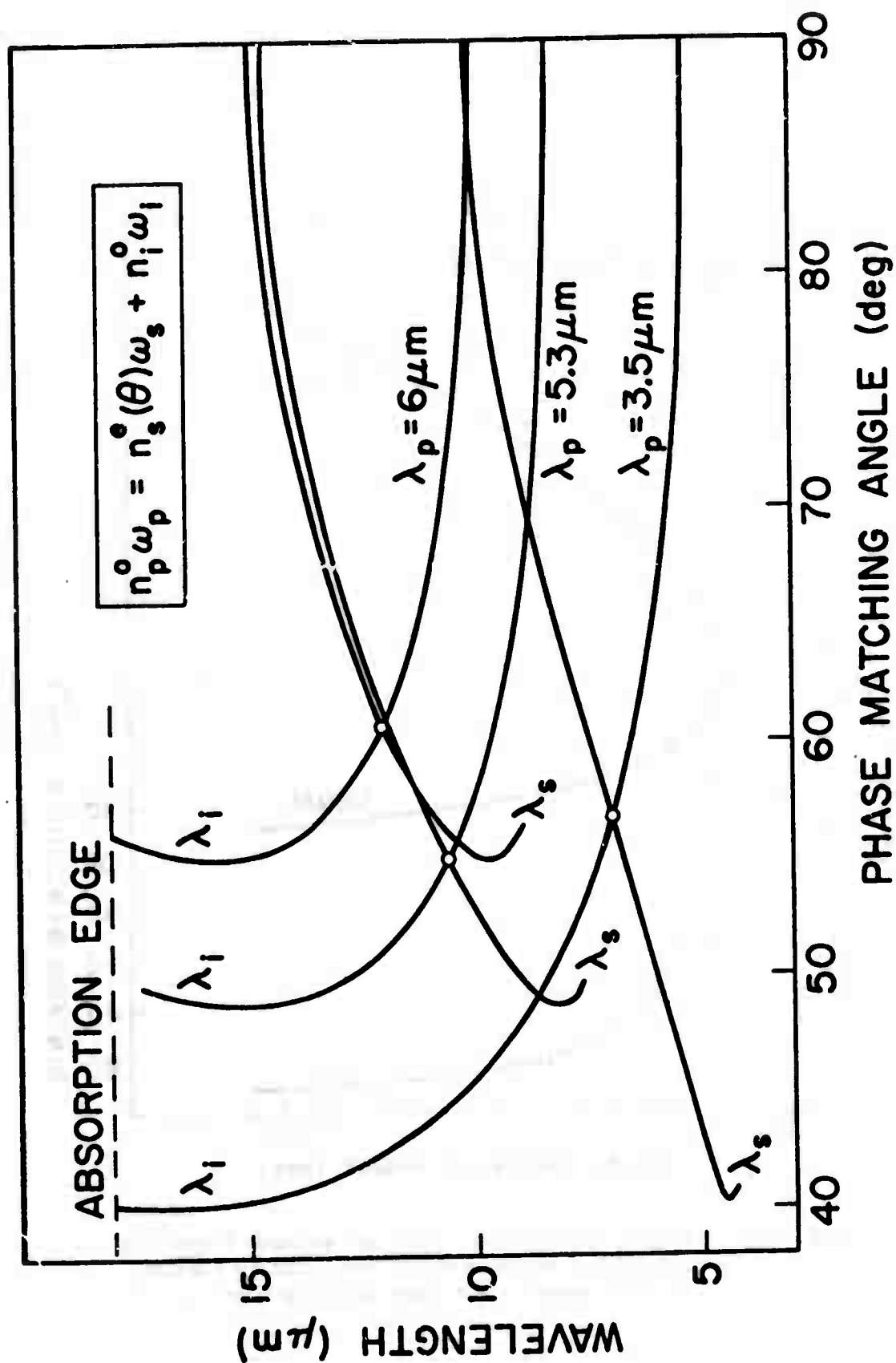


FIG. 26b--Theoretical tuning curves for type II phasematching in CdGeAs₂ for several pump wavelengths.

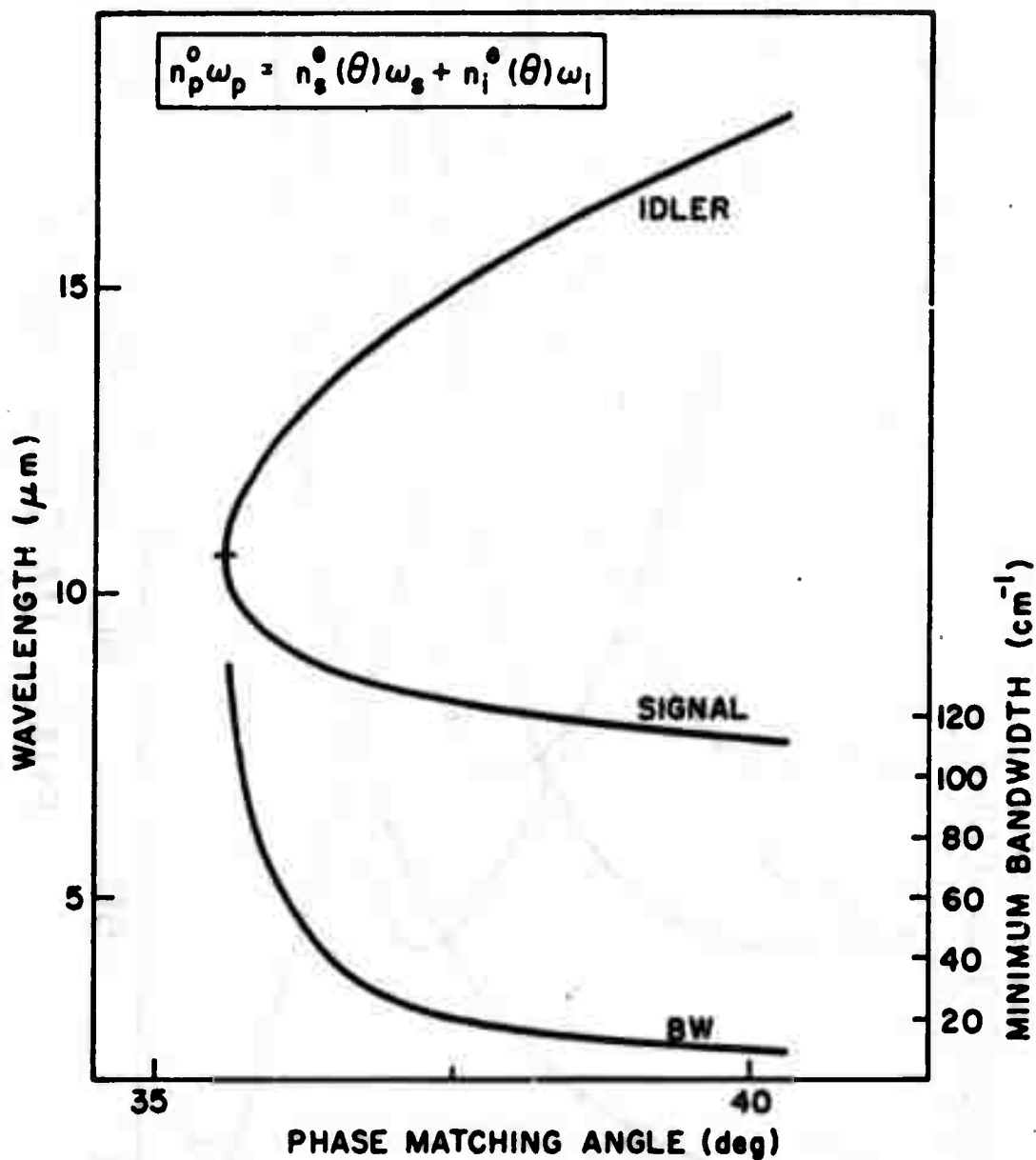


FIG. 27(a)--Theoretical tuning curve and minimum bandwidth for type I phasematching for a one cm CdGeAs₂ crystal pumped by a pump wavelength of 5.3 μm.

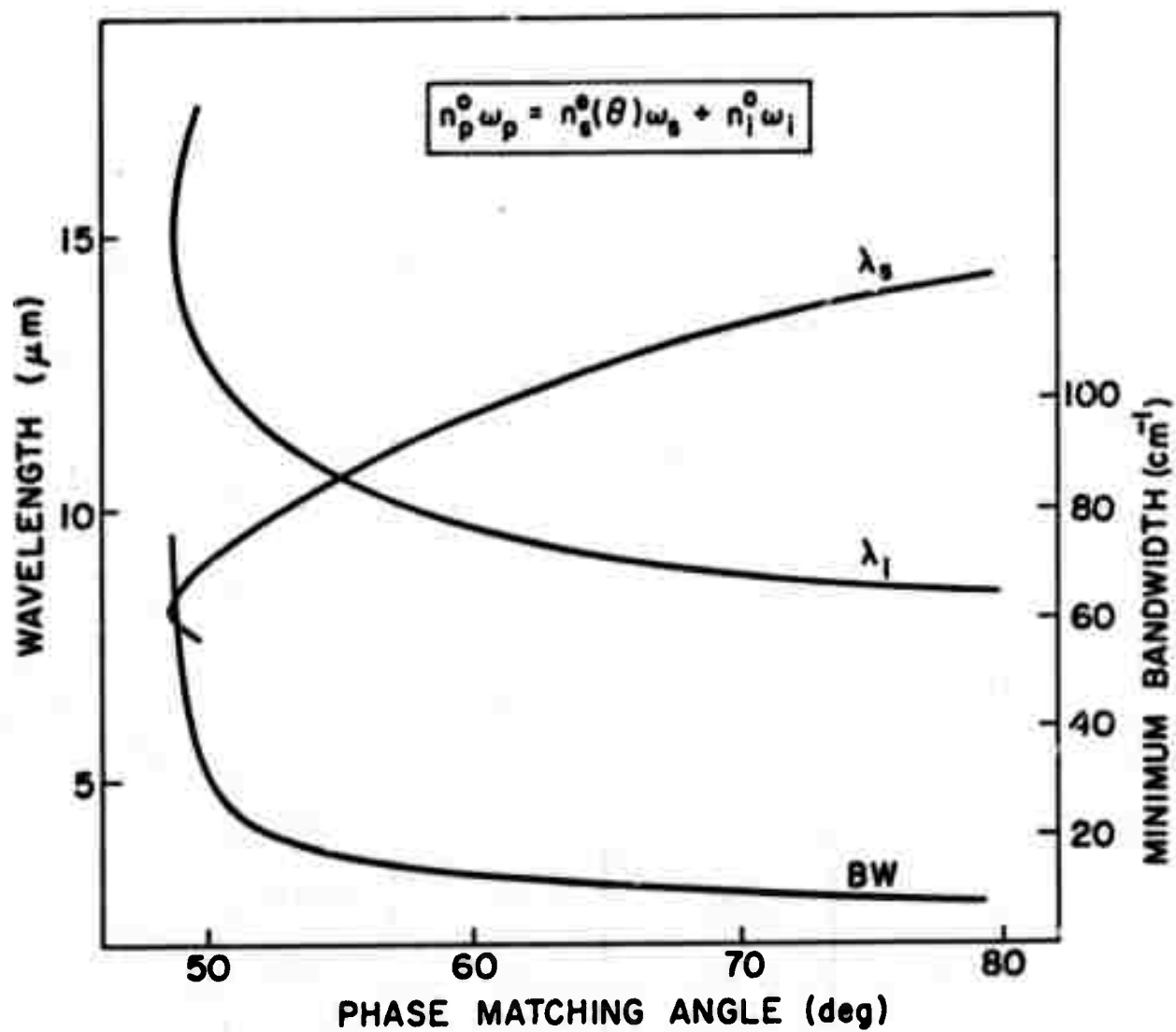


FIG. 27(b)--Theoretical tuning curve and minimum bandwidth for type II phasematching for a one cm CdGeAs₂ crystal pumped by a pump wavelength of 5.3 μm.

TABLE XV

MEASURED INDICES OF REFRACTION FOR CdGeP₂

Wavelength $\lambda(\mu\text{m})$	n_e	n_o	$n_e - n_o$
0.85	3.4834	3.4283	0.0551
0.90	3.4397	3.3958	0.0439
0.95	3.4099	3.3710	0.0389
1.00	3.3841	3.3493	0.0348
1.15	3.3334	3.3068	0.0266
2.10	3.2282	3.2147	0.0135
3.39	3.2026	3.1913	0.0113
4.00	3.1963	3.1856	0.0107
5.00	3.1899	3.1793	0.0106
6.00	3.1853	3.1746	0.0107
10.6	3.1517	3.1367	0.0150

estimate the index values to be good to at least one part in the third place. The average index of 3.2 agrees well with 3.1 as predicted from III-V analogs, but is smaller than the value of 3.6 reported by Goryunova et al.⁶¹ Figure 28 shows a plot of the indices of refraction. The birefringence of 0.01 is too small for parametric interactions. The result is in complete disagreement with Goryunova et al., but agrees with Boyd et al.²⁹ Goryunova et al. did their measurements on platelets grown by vapor transport while we used Bridgman grown material. Assuming the Russian measurements are correct, the only explanation may be that there exists two forms of CdGeP_2 both with chalcopyrite structure but with different order of the Cd and Ge atoms within the unit cell. This needs further clarification by careful x-ray analysis.

The birefringence of CdGeP_2 similar to CdGeAs_2 , increases with increasing temperature. At $2.10 \mu\text{m}$ we measure $dn_e/dT = 2.5 \times 10^{-4}/^\circ\text{C}$ and $dn_o/dT = 2.2 \times 10^{-4}/^\circ\text{C}$ which gives $d(\Delta n)/dT \approx 0.3 \times 10^{-4}/^\circ\text{C}$ in the temperature range of 25°C to 45°C .

2. Measurement of the Second Order Nonlinear Coefficient

We have measured the nonlinear coefficient relative to GaAs by second harmonic generation of a Q-switched CO_2 laser using the wedge technique described in Section A.4. Figure 29 shows a schematic of the experimental set-up. We Q-switched the CO_2 laser by rotating the grating. A He-Ne laser reflecting off the grating provided a trigger signal. By adjusting the aperture the laser operated in a Gaussian

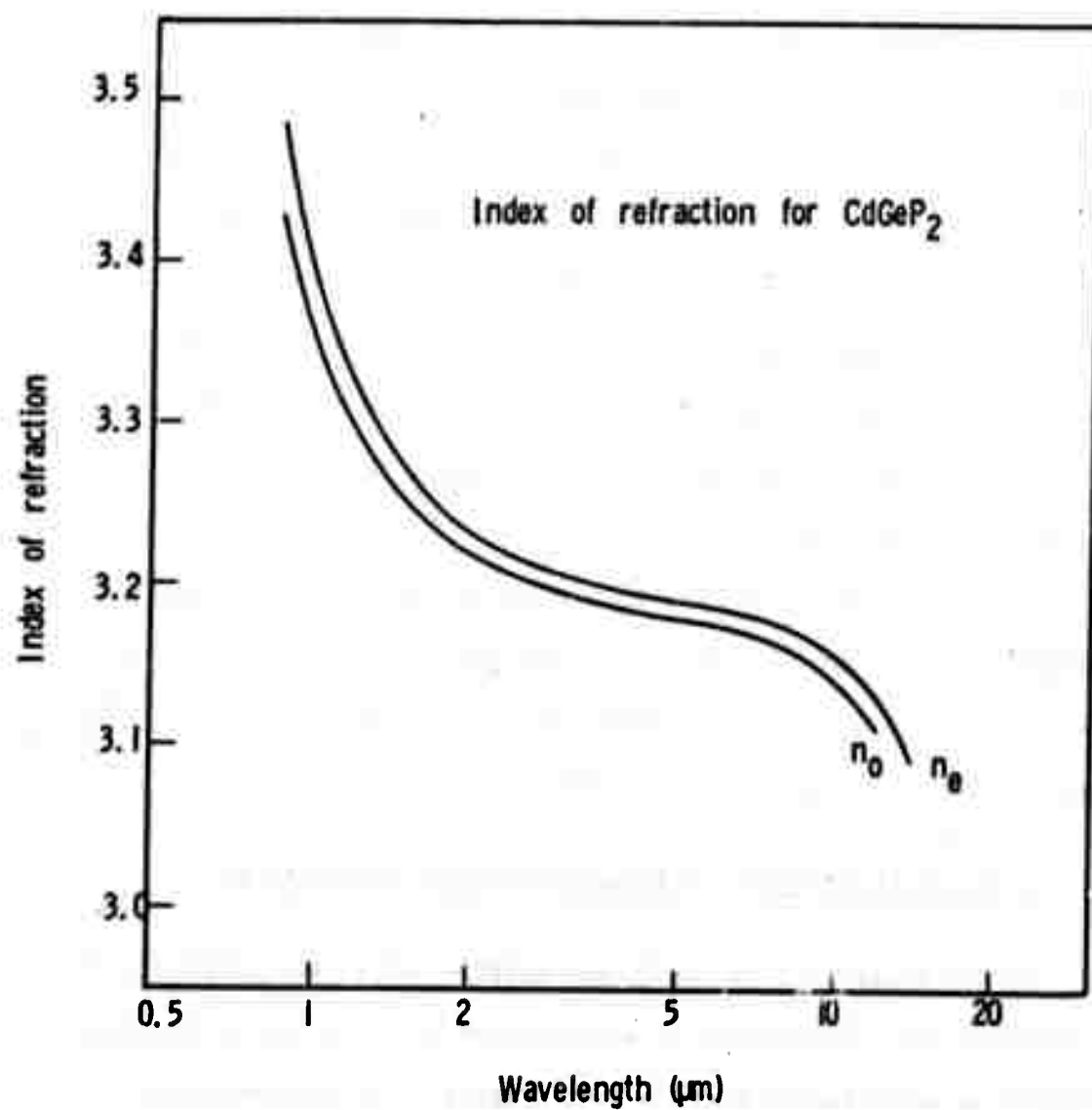


FIG. 28--Indices of refraction for CdGeP_2 .

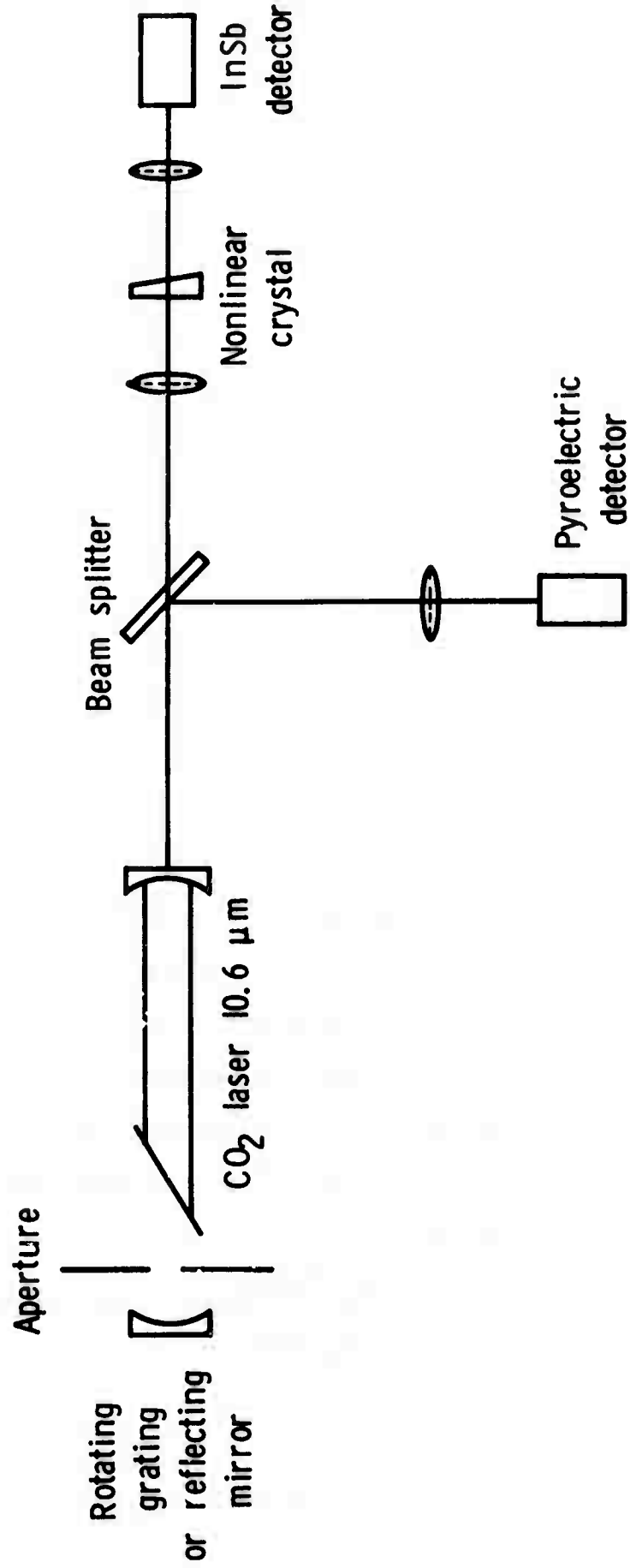


FIG. 29--Measurement of the nonlinear coefficients.

mode with a pulse length of about 300-400 nsec and peak power of approximately 200 watts. A pyroelectric detector monitored the CO_2 laser output. The detector was sufficiently fast to completely resolve the pulse. An uncoated 4 cm germanium lens focused the laser to a 40 μm spot size at the wedged SHG crystal. Another germanium lens focused the SHG signal onto a liquid nitrogen cooled InSb detector preceded by a sapphire filter which blocked the 10.6 μm CO_2 laser radiation. The detector had an active area of $0.5 \times 0.5 \text{ mm}^2$ and a response time of 8 μsec so it did not resolve the pulse. The detector output was fed into a boxcar integrator and a chart recorder.

The CdGeAs_2 samples for the nonlinear coefficient measurements came from boule No. 16. The GaAs reference sample was supplied by Monsanto. It was Cr doped and had a resistivity of $3 \times 10^8 \Omega\text{-cm}$. Table XVI lists the parameters for the experiment. The measured coherence length for CdGeAs_2 of $22 \pm 1 \mu\text{m}$ agrees well with the 21.2 μm calculated from Eq. (6.62) and the index data. The coherence length for GaAs is in good agreement with the published values in references 11 and 62 of $104 \pm 7 \mu\text{m}$ and $107 \pm 5 \mu\text{m}$, respectively. For the spot size and crystal thickness we used both ξ and $B \ll 1$ [cf. Eq. (6.10)]. In addition, since the spot size was much smaller than the translation distance between two SHG minima, we can use Eq. (6.65) to determine the nonlinear coefficient. The CdGeAs_2 nonlinear coefficient measured relative to GaAs is

$$\frac{d_{36}(\text{CdGeAs}_2)}{d_{14}(\text{GaAs})} = 3.4 \pm 20\% , \quad (6.87)$$

TABLE XVI

MEASUREMENT OF THE SHG NONLINEAR COEFFICIENT

	GaAs	CdGeAs ₂
Crystal orientation	(111)	(110)
Wedge angle	4°58'	1°46'
CO ₂ polarization	[110]	[$\bar{1}\bar{1}0$]
SHG polarization	[112]	[001]
d _{eff}	$\sqrt{2/3} d_{14}$	d ₃₆
n ₁	3.27 ¹¹	3.5688
n ₂	3.30 ¹¹	3.6933
l _c [m], measured	104 ± 3	22.1 ± 1

and with $d_{14}(\text{GaAs}) = 1.14 \times 10^{-21}$ (mks),⁶² we have that $d_{36}(\text{CdGeAs}_2) = 3.9 \times 10^{-21}$ (mks).

The optical properties of the II-IV-V₂ compounds can be estimated from the III-V analogs. Using the definition in Eq. (2.2) we compare the Miller's δ for CdGeAs₂ with the III-V analogs GaAs and InAs. We obtain $\delta(\text{CdGeAs}_2)/\delta(\text{GaAs}) = 1.8$ and $\delta(\text{CdGeAs}_2)/\delta(\text{InAs}) = 1.3$. Assuming that the average bond nonlinearity for CdGeAs₂ is similar to $1/2(\text{GaAs} + \text{InAs})$ we expect Miller's δ for CdGeAs₂ to be the average of the III-V analogs. The measured value is somewhat larger but it is much smaller than calculated by Chemla.¹⁵ He uses Levine's bond-charge model and obtains $\delta(\text{CdGeAs}_2)/\delta(\text{GaAs}) = 5.4$.

Recently Boyd et al.,²⁹ have measured the nonlinear coefficient for CdGeAs₂. They report $d_{36}(\text{CdGeAs}_2)/d_{14}(\text{GaAs}) = 2.62 \pm 15\%$, and for the coherence length they measure $21.5 \pm 1 \mu\text{m}$ and calculate $23.0 \mu\text{m}$. These results are in good agreement with our previously published results.⁶³ Also Goryunova et al.,⁶⁴ have measured the nonlinear coefficient for CdGeAs₂. They used a ruby laser with both the fundamental and the second harmonic frequency well above the bandgap frequency. Because of the reduced electronic contribution to the nonlinear coefficient, they measured a smaller value than expected in the transparent region of the crystal.

In Section VI.A.1(b), we defined three figures of merits where M_1 is applicable for 90° phasematching. For phasematching at other angles M_{SHGtot} or M_{SHGgaus} must be used. They are the figure of

merits for maximum SHG conversion and for SHG into a Gaussian mode. M_{SHGgaus} also applies when crystals are compared for use in parametric oscillators. Table XVII compares CdGeAs_2 with tellurium and Ag_3AsS_3 which are two of the most popular infrared nonlinear materials. For reference we also list GaAs. CdGeAs_2 has the second largest known nonlinear coefficient of any phasematchable crystal. Only tellurium has a larger coefficient, but since tellurium also has a larger double refraction angle, the CO_2 laser doubling efficiency is largest in CdGeAs_2 . The maximum useful crystal length l_{max} for CdGeAs_2 is 2.7 mm for confocal focussing compared to only 0.1 mm for tellurium. The theoretical $10.6 \mu\text{m}$ conversion efficiency in CdGeAs_2 for a 2.7 mm crystal and confocal focussing is $P_{\text{SH}}/P_{\text{Fund}} = 0.001 P_{\text{Fund}}(W)$ for the two phasematching conditions. This neglects surface reflections. We use the calculated doubling efficiency to estimate the threshold for a degenerate parametric oscillator pumped at $5.3 \mu\text{m}$. Assuming the equivalent loss due to the finite build-up time is negligible compared to the other losses in the cavity [cf. Eqs. (6.34) and (6.36)], we find from Eqs. (6.32) and (6.33) that the threshold pump power P_{th} is

$$P_{\text{th}} = \alpha_s \alpha_i \times 10^3 (W) \quad (6.88)$$

for a doubly resonant oscillator (DRO) and

$$P_{\text{th}} = 2\alpha_s \times 10^3 (W) \quad (6.89)$$

TABLE XVII

FIGURE OF MERITS FOR INFRARED NONLINEAR CRYSTALS

	CdGeAs ₂	Te	Ag ₃ AsS ₃	GaAs
n	3.60	4.86	2.52	3.3
d (rel. GaAs)	3.4	6.9	0.14	1
$M_1 = d^2/n^3$	193	322	1	22
θ_m (SHG of 10.6 μm)	35°34' (I) 54°51' (II)	14°10'	22°30'	---
ρ	1°20'	5°42'	3°30'	---
$l_{\text{max}} = \lambda/2n_1\rho^2 [\text{mm}]$	2.72	0.11	0.56	---
$M_{\text{SHGtot}} = M_1 \sqrt{n}/\rho$	607	274	1	---
$M_{\text{SHGgaus}} = M_1/\rho^2$	1330	121	1	---

for a singly resonant oscillator (SRO). With 10% signal and idler losses, the threshold pump power and power density are, respectively,

$$P_{th} = 10 \text{ W} \quad \text{and} \quad P_{th}/A = 1 \text{ MW/cm}^2 \quad (6.90)$$

for a DRO and

$$P_{th} = 200 \text{ W} \quad \text{and} \quad P_{th}/A = 20 \text{ MW/cm}^2 \quad (6.91)$$

for a SRO. The area A is as usual, defined as $\pi w_p^2/2$. Equations (6.90) and (6.91) are for confocal focusing in a 2.7 mm crystal. A larger crystal does not increase the gain, but it reduces the power density such that crystal damage is less probable. The necessary pump power to reach threshold is available at wavelengths near 5 μm either from a TEA CO laser or from a CdGeAs₂ doubled TEA CO₂ laser. However, the present CdGeAs₂ crystals are too lossy to attempt a parametric oscillator experiment. Assuming the losses will reduce with further crystal development, a 2.7 mm crystal should be adequate for a doubly resonant oscillator. For a singly resonant oscillator, however, the crystal should be at least 5 mm to reduce the power density. The measured optical damage threshold for CdGeAs₂ is 40 MW/cm² at 10.6 μm .

3. Phasematched Parametric Interactions

We have demonstrated several phasematching experiments in CdGeAs₂. The measured phasematching angles are in reasonable agreement with the calculated values based on the measured indices of refraction. Table XVIII lists the results. For the SHG experiments we used a CW CO₂ laser.

TABLE XVIII
PHASEMATCHING EXPERIMENTS

Process	SHG of 10.6 μm	SHG of 10.6 μm	SHG of 10.6 μm	Mixing of 10.6 μm + 5.3 μm
Boule No.	16	B4	31	31
Phasematching condition	II	II	I	I
Measured phase- matching angle	49° 30' ± 15'	48° 50' ± 15'	31° 40' ± 20'	33° 43' ± 1°
Calculated phase- matching angle	54° 51'	54° 51'	35° 34'	35° 30'
Walk-off angle, ρ	1° 20'	1° 20'	1° 20'	
Crystal length l (mm)	1.34	4.2	1.95	1.95
Measured angular half-width (deg)	7.5-8.5	2.25-3.0	3	1.7-1.8
Calculated angular half-width (deg)	8.5	2.25	3	1.9

We chopped the beam to reduce the crystal heating. A motor scanned the crystal through the phasematching position. Figure 30 shows the second harmonic output power versus the external rotation angle for one of the crystals. It shows the regular sinc-curve dependence given by Eq. (6.20). The curve has some oscillations near the maximum. These occur when the laser is normal to the crystal. The feed-back then makes the laser unstable which allows an accurate measurement of the phasematching angle. The oscillations are monitored at the SHG wavelength or by recording the CO_2 laser output. The angle between the center of the oscillations and the maximum of the sinc-curve gives the phasematching angle relative to the normal of the crystal face, and by x-ray diffraction we determine the angle between the normal and the c-axis. With this technique we measure the phase-matching angle within 15 minutes.

In Table XVIII the external half-angles at the half-power points are calculated using Eqs. (6.28), (6.29), and (6.30). By comparing the calculated with the measured half-angles, we obtain information about the crystal quality. In nonuniform crystals with variations in the indices of refraction, the phasematching condition may not be satisfied over the whole crystal length. This leads to a larger angular half-width than calculated. The crystals listed in Table XVIII have lengths between 2 and 4 millimeters and the quality is good enough for the phasematching length to be approximately equal to the crystal length.

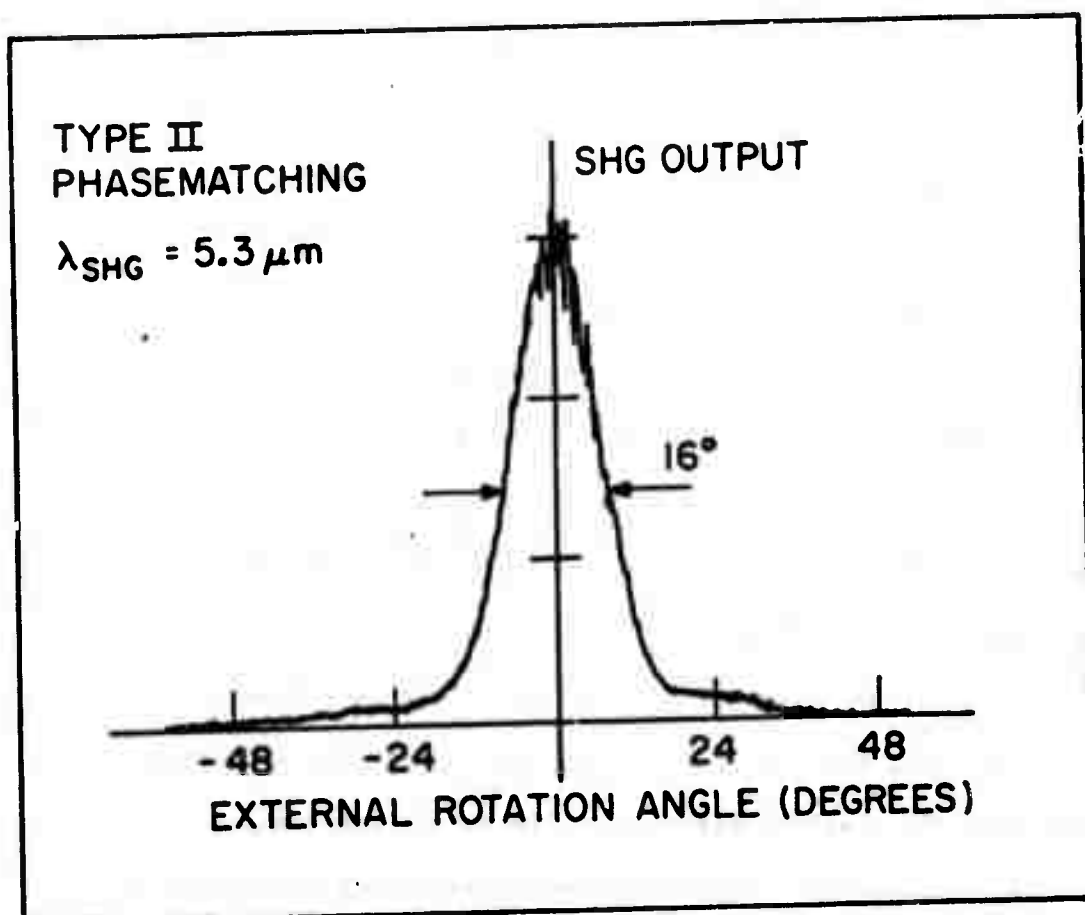


FIG. 30--Angular dependence of the second harmonic output power.

To further test the crystal quality, the crystal is translated perpendicularly through the laser beam while the phase-matched second harmonic output is monitored. Figure 31 shows a typical horizontal and vertical scan for the SHG crystal from boule No. 16. "Good" crystal regions are over distances of about 1 mm. It is therefore possible to avoid the areas with significant absorption.

The mixing experiment in Table XVIII between $10.6\text{ }\mu\text{m}$ and $5.3\text{ }\mu\text{m}$ to generate third harmonic at $3.53\text{ }\mu\text{m}$ was achieved by first doubling and then mixing in two separate CdGeAs_2 crystals. The crystals are placed right next to each other. For the doubling we used the 4.2 mm type II phase-matching crystal and the mixing was in a 1.95 mm crystal cut for type I phase-matching.

We have also generated third harmonic directly using a TEA CO_2 laser. The calculated phase-matching angles for tripling are $49^{\circ}4'$ for type I and $67^{\circ}0'$ for type II phase-matching. No solution exists for type III phase-matching. The 1.97 mm crystal from boule B17 was cut for type II phase-matching which we expect to give the largest nonlinear efficiency. The crystal quality was not as good as for some of the other crystals. Using Eqs. (6.27) and (6.49) we calculate an angular half-width of $3^{\circ}13'$ compared to a measured half-width of $4^{\circ}15'$. This corresponds to a phase-matching length of only 1.5 mm . The crystal could be used for both phase-matched type II SHG and type II THG and the measured internal angle between the two phase-matching positions of $11.2 \pm 1^{\circ}$ was in good agreement with the calculated difference of 12.1° .

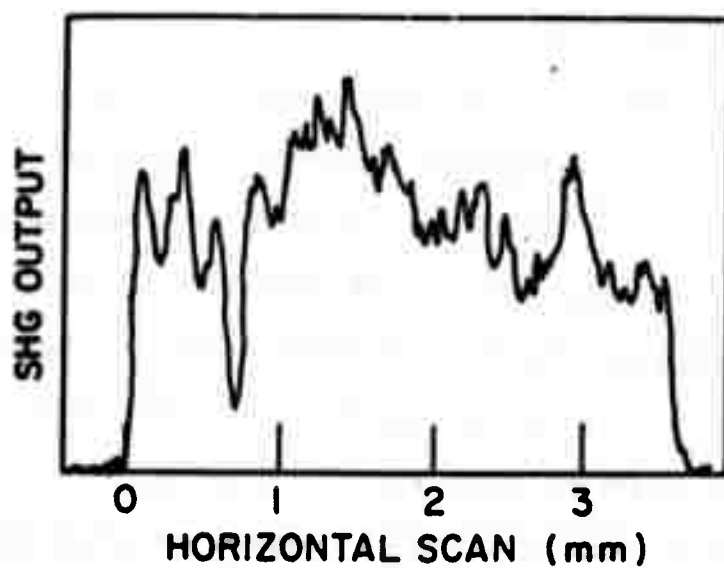
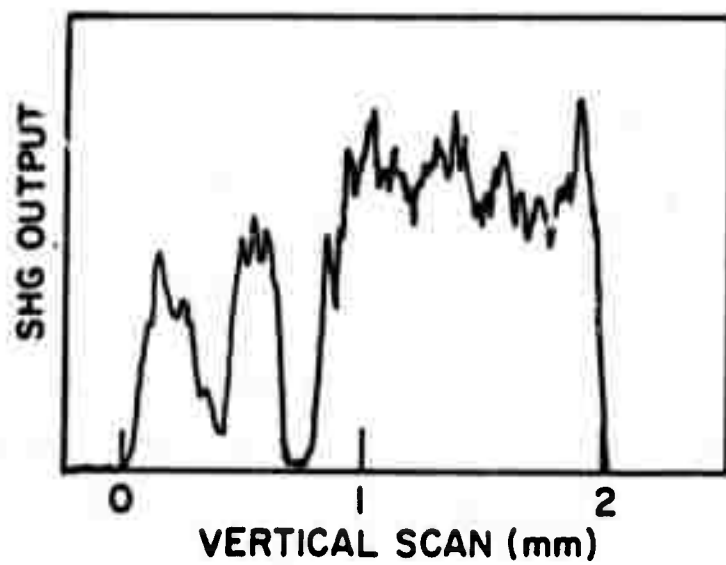


FIG. 31--Variation in the SHG output power over the crystal cross section.

The measured phasematching angle for the SHG crystal from boule No. 16 was $49^{\circ}30'$ as stated in Table XVIII. At one spot on the crystal, however, we measured $50^{\circ}40'$. This was probably due to a crystallite at a slightly different orientation to the rest of the crystal. To determine how a change in the dispersion D and the birefringence B at the fundamental frequency affect the phasematching angle θ_m , we differentiate Eqs. (2.5) and (2.6) and find

$$\delta\theta_m = \frac{1}{2} \tan \theta_m \left(\frac{\delta D}{D} - \frac{\delta B}{B} \right) \quad (6.92)$$

for both phasematching conditions. One of the problems with absorption in the crystals is that the resulting temperature increase changes the phasematching angle. We estimate the effect of a temperature raise of 10°C by using $\frac{dB}{dT} = 3.9 \times 10^{-5} \text{ }^{\circ}\text{C}^{-1}$ from Table XIV and assuming $\frac{dD}{dT} \approx 1 \times 10^{-4} \text{ }^{\circ}\text{C}^{-1}$. For CdGeAs_2 with a birefringence of $B = 0.089$ and a dispersion of $D = 0.029$ this gives $\delta\theta_m = +0.6^{\circ}$ for type I and $\delta\theta_m = 1.2^{\circ}$ for type II phasematching for SHG of $10.6 \text{ }\mu\text{m}$. The phasematching angle therefore increases with increasing temperature. A change in the carrier concentration also affects the phasematching angle. An increase of the hole concentration of $5 \times 10^{15} \text{ cm}^{-3}$ results in a decrease in the birefringence at $10.6 \text{ }\mu\text{m}$ of $\delta B = -0.002$ according to Eq. (6.86). From Eq. (6.68) we calculate the change in the dispersion of the ordinary index as $\delta D = 0.7 \times 10^{-4}$. This increases the phasematching angle by $\delta\theta_m = 0.5^{\circ}$ for type I and $\delta\theta_m = 1^{\circ}$ for type II phasematching. Finally it is worth noting that the indices of refraction for p-type material are also perturbed by the intraband

transitions between the split valence bands. It is more complicated, however, to evaluate the magnitude.

Recently, Boyd et al.²⁹ have measured the type I and type II phasematching angles for SHG of 10.6 μm to be $35 \pm 1^\circ$ and $51.6 \pm 0.5^\circ$ respectively. This is in reasonable agreement with our results considering they had crystals with much larger absorption. A birefringence change from boule to boule was observed by Boyd et al.⁶⁵ for ZnGeP_2 where they report a change of 0.001 out of a total birefringence of 0.048 at 1.06 μm . Unfortunately they did not measure the carrier concentration.

4. Maximum 10.6 μm Doubling Efficiency and Optical Damage Threshold

We have observed a maximum doubling efficiency in an uncoated CdGeAs_2 crystal of 1.4% for a TEA CO_2 laser. If we subtract the reflection losses at the crystal faces, this gives an expected doubling efficiency of 3% for a coated crystal. This compares to the best results reported for tellurium.^{58,59} The laser had a Gaussian output beam with a pulse length of 200 nsec and a repetition rate of 14 pps. A 27 cm focal length germanium lens focused the beam into the SHG crystal. The laser power was measured by a CRL power meter and the second harmonic by an Eppley thermopile. The crystal was 1.95 mm long and it was cut for type I phasematching. The measured absorption at the laser and the second harmonic frequency was $a_{10.6} = 0.84 \text{ cm}^{-1}$ and $a_{5.3} = 3 \text{ cm}^{-1}$, respectively. According to Eq. (6.21)

this reduces the theoretical SHG conversion efficiency by a factor of 0.40. At the measured 1.4% conversion efficiency the incident laser peak power was 12.5 kW. Including losses, this gives a theoretical conversion efficiency of 2.4% for a square laser pulse. The pulse shape, however, was more Gaussian and this reduces the theoretical conversion by a factor of approximately $2/3$ to 1.6% which agrees well with the measured conversion.

We observed a saturation in the SHG conversion efficiency before the optical burn density threshold was reached. This might be due to either a thermal effect or due to generated free carriers resulting from optical absorption between an impurity level and the valence or the conduction band. With reduced optical absorption we believe the saturation effect will vanish. For the measured crystal the saturating laser power density inside the crystal was approximately 15 MW/cm^2 .

The optical burn density measured by the TEA CO_2 laser was $38 \pm 2 \text{ MW/cm}^2$ for most crystals. In one crystal, however, it was as high as 55 MW/cm^2 . We have also measured the cw damage threshold. At $10.6 \mu\text{m}$ it is smaller than 1000 W/cm^2 .

5. Carrier Absorption

Figure 32 shows the free electron absorption in n-type CdGeAs_2 . The 3.5 power dependence is characteristic of charged impurity scattering [cf. Eq. (6.71)], and the result agrees with reference 66 which reports a power dependence of 3.2 - 3.4.

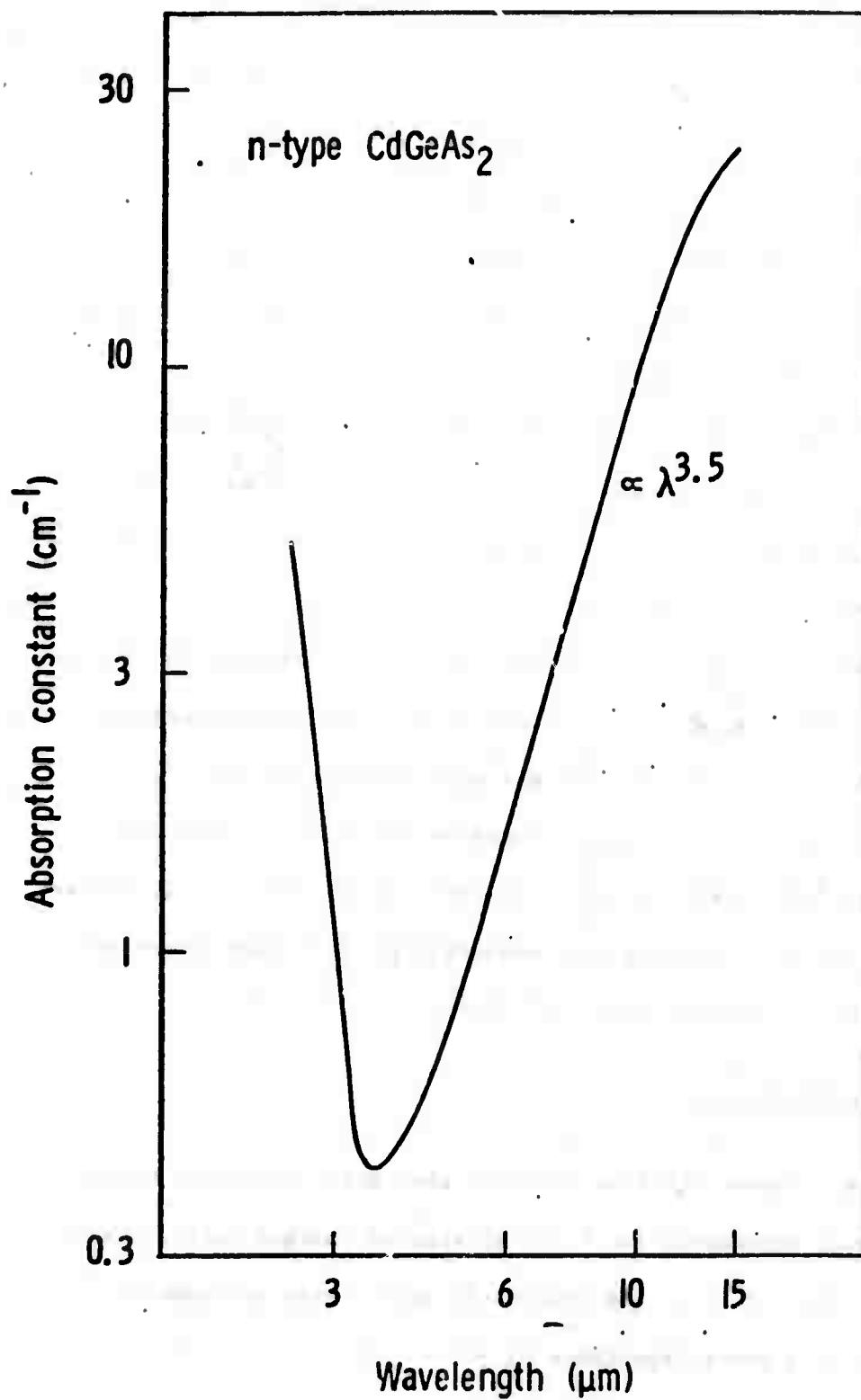


FIG. 32--Free electron absorption in n-type CdGeAs₂.

Figure 33 shows the lowest measured absorption in p-type CdGeAs_2 . By writing $\epsilon = 0.151 \text{ eV} - \hbar\omega$ in Eqs. (6.75) and (6.77) and adjusting the hole concentration to $2.4 \times 10^{15} \text{ cm}^{-3}$ we obtain excellent agreement between the measured and the calculated absorption for transitions between the valence bands v_1 and v_2 . The measured valence band splitting energy is therefore $0.15 \pm 0.01 \text{ eV}$ which is not too far off our estimated 0.20 eV . A theoretical value for the splitting energy of 0.17 eV is given in reference 66. This reference also discusses intraband absorption but uses a formula that does not apply for the chalcopyrites.

In conclusion, in order to obtain negligible absorption in p-type CdGeAs_2 the hole concentration should be smaller than 10^{15} cm^{-3} . Compensation or doping to reduce the carrier concentration is therefore necessary to obtain high optical quality material.

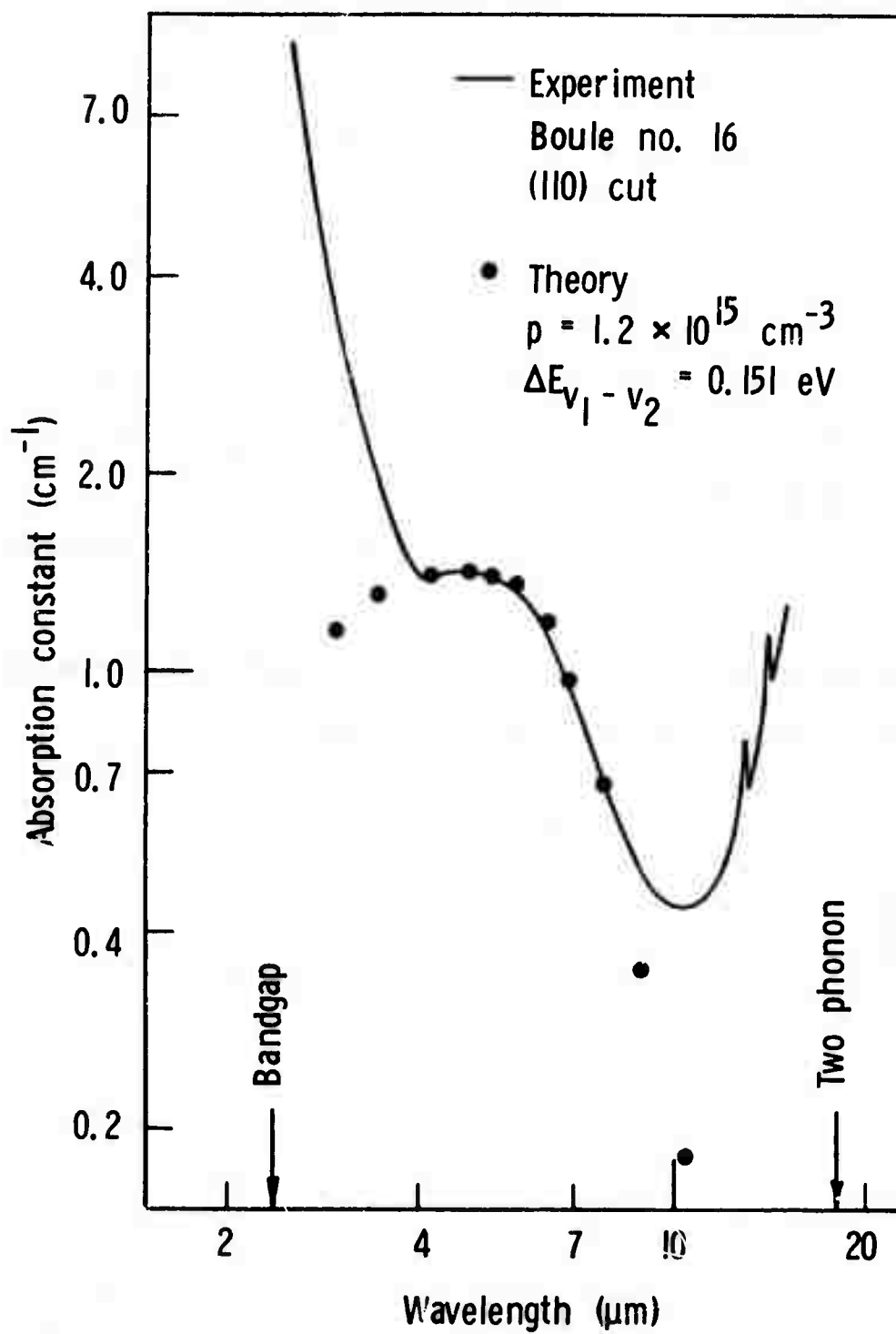


FIG. 33--Intra band absorption in p-type CdGeAs_2 .

CHAPTER VII

APPLICATION OF TUNABLE RADIATION FOR AIR POLLUTION DETECTION

Perhaps the most challenging application of tunable infrared radiation is for air pollution detection. In this chapter we compare the detection sensitivity using an infrared parametric oscillator to other laser detection methods. The important results have been published and are presented in Appendix D. Of the three analyzed schemes: Raman backscattering, resonance backscattering, and resonance absorption; only the last is sensitive enough to detect dispersed pollutants.

CHAPTER VIII

CONCLUSION

CdGeAs_2 is very promising for infrared parametric generation and efficient SHG and mixing. We have measured the nonlinear coefficient and determined the phasematching conditions. The crystal is phasematchable over most of its transparency range between 2.4 and 18 μm and it has the highest figure of merit of any phasematchable nonlinear crystal. CdGeP_2 is not phasematchable. It has approximately the same tetragonal distortion as CdGeAs_2 but the birefringence is a factor of ten smaller.

The growth of high optical quality chalcopyrite crystals is hindered by several problems. Extensive crystal cracking occurs during growth and the boules have nonuniform optical transmission. We have measured the linear thermal expansion coefficient for CdGeAs_2 . It is very anisotropic and this probably explains the large number of cracks. We have been able to reduce the cracks by growth of single crystals in a bismuth solution. There has been no correlation between the nonuniform optical transmission and the impurity content. The material probably undergoes significant self-compensation during growth and we suspect that slight stoichiometric variations may explain the nonuniformity in the optical transmission.

To explain one of the absorption mechanisms in p-type material we have determined the bandstructure near the Brillouin zone center.

The bandstructure results let us calculate the absorption due to intraband transitions between the split valence bands and we obtain good agreement with measured values for CdGeAs_2 . Experimentally we determine the valence band splitting energy to be $\Delta E_{v_1-v_2} = 0.15 \pm 0.01$ eV. To have negligible intraband absorption the hole concentration must be smaller than 10^{15} cm^{-3} .

The free carriers also affect the indices of refraction and the measured phasematching angles. An increase in the carrier concentration of $5 \times 10^{15} \text{ cm}^{-3}$ changes the phasematching angle by approximately 1° for SHG of a CO_2 laser with type II phasematching.

Because of the anisotropic effective masses in CdGeAs_2 , carrier injection introduces a birefringence change. We have proposed to use this effect to construct a $10.6 \mu\text{m}$ modulator.

Since the carrier concentration is very important for the measured optical properties of CdGeAs_2 we have determined the temperature dependence of the carrier concentration in p-type CdGeAs_2 . It is constant from 77°K to 200°K and then starts to increase. At room temperature the carrier concentration in the CdGeAs_2 grown by the vertical Bridgman method is usually between 5×10^{15} to $5 \times 10^{16} \text{ cm}^{-3}$.

By SHG, THG, and mixing experiments we have verified several of the calculated phasematching conditions. We have observed as high as 2% $10.6 \mu\text{m}$ doubling efficiency in a 2 mm CdGeAs_2 crystal, and the measured burn density is 40 MW/cm^2 for a 200 nsec CO_2 laser pulse.

We expect the quality to improve with further crystal development. It is a long and tedious process, however, to determine the optimum growth conditions. To minimize the optical absorption it is necessary

to reduce the carrier concentration by compensation or doping. The CdGeAs_2 has an extensive tuning range and due to a large figure of merit only a few millimeter long crystal is necessary to reach parametric oscillator threshold. Presently available crystals have almost low enough optical absorption to allow the construction of a doubly resonant oscillator. The calculated threshold pump power at $5.3 \mu\text{m}$ for a 2.7 mm crystal is low for 10% loss at the signal and the idler wavelength.

The most straight forward application of an infrared parametric oscillator is in spectroscopy with air pollution detection as a particular stimulating possibility.

APPENDIX A

TYPE I AND TYPE II PHASEMATCHING EQUATIONS

The extraordinary index of refraction for a wave propagating at an angle θ with respect to the crystal c-axis is given by⁸

$$\frac{1}{n_e(\theta)^2} = \frac{\cos^2 \theta}{n_o^2} + \frac{\sin^2 \theta}{n_e^2} \quad . \quad (A.1)$$

When the birefringence $B = n_e - n_o$ is much smaller than n_o , we can rewrite Eq. (A.1) as

$$n_e(\theta) \approx n_o + B \sin^2 \theta \quad . \quad (A.2)$$

The phase-matching conditions for second harmonic generation in a positive birefringent crystal ($B > 0$) is

$$n_o^{2\omega} = n_e^\omega(\theta) \quad (A.3)$$

for type I and

$$n_o^{2\omega} = \frac{1}{2} \left(n_o^\omega + n_e^\omega(\theta) \right) \quad (A.4)$$

for type II phasematching. We calculate the phasematching angle by substituting Eq. (A.2) into Eqs. (A.3) and (A.4). Defining the dispersion as $D = n_o^{2\omega} - n_o^\omega$, we find for the two phasematching conditions that

$$\sin \theta_I = \sqrt{D/B^\omega} \quad (\text{A.5})$$

and

$$\sin \theta_{II} = \sqrt{2D/B^\omega} \quad (\text{A.6})$$

where B^ω is equal to the birefringence at the fundamental frequency ω .

Similarly for a negative birefringent crystal ($B < 0$) where the phasematching conditions for type I and type II phasematching can be written, respectively, as

$$n_e^{2\omega}(\theta) = n_o^\omega \quad (\text{A.7})$$

and

$$n_e^{2\omega}(\theta) = \frac{1}{2} \left(n_o^\omega + n_e^\omega(\theta) \right), \quad (\text{A.8})$$

we obtain

$$\sin \theta_I = \sqrt{-D/B^{2\omega}} \quad (\text{A.9})$$

and

$$\sin \theta_{II} = \sqrt{-\frac{D}{B^{2\omega} - \frac{1}{2} B^\omega}} \quad (\text{A.10})$$

For the extraordinary wave, the power flow and the wavevector are not in the same direction. The Poynting vector walk-off angle is given by⁸

$$\tan \rho = \frac{n_e(\theta)^2}{2} \left(\frac{1}{n_e^2} - \frac{1}{n_o^2} \right) \sin 2\theta, \quad (\text{A.11})$$

which with the approximation $|B| \ll n_o$ reduces to the simpler expression

$$\tan \rho \approx - \frac{B}{n_o} \sin 2\theta. \quad (\text{A.12})$$

Using Eqs. (A.5) and (A.6) or Eqs. (A.9) and (A.10) we can determine quickly if a material has sufficient birefringence for phase-matched SHG.

APPENDIX B

SECOND HARMONIC GENERATION IN A WEDGED PLATELET

Equation (6.21) gives the SHG output power from a crystal with a constant length l . It assumes Gaussian modes with spot sizes w_1 and $w_2 = w_1 / \sqrt{2}$ at the fundamental and the second harmonic wavelength. In order to examine how a wedged sample as in Fig. (B.1) modifies the SHG output power, we recast Eq. (6.21) in terms of the peak intensities and then average the varying crystal length over the transverse mode distribution. With $P_{1out} = I_1(\pi w_1^2/2)$ and $P_{2out} = I_2(\pi w_2^2/2)$ we obtain

$$I_2 = \frac{128 \eta_0^3 \omega_1^2 d^2 I_1^2}{(n_2 + 1)^2 (n_1 + 1)^4} S(l) \quad (B.1)$$

Here $S(l)$ is expressed by

$$S(l) = \frac{\left(e^{-(\alpha_2 l/2)} - e^{-\alpha_1 l} \right)^2 + 4 e^{-\left(\frac{\alpha_2}{2} + \alpha_1 \right) l} \sin^2 \frac{\Delta k l}{2}}{(\Delta k)^2 + \left(\frac{\alpha_2}{2} - \alpha_1 \right)^2}, \quad (B.2)$$

where $l = l_0 - y \tan \alpha$ according to Fig. (34). To calculate the SHG power, $S(l)$ must be averaged over the transverse mode distribution. As before, we assume the laser has a Gaussian mode such that $I_1(r) = I_1 \exp[-2r^2/w_1^2]$. With the crystal dimensions in the

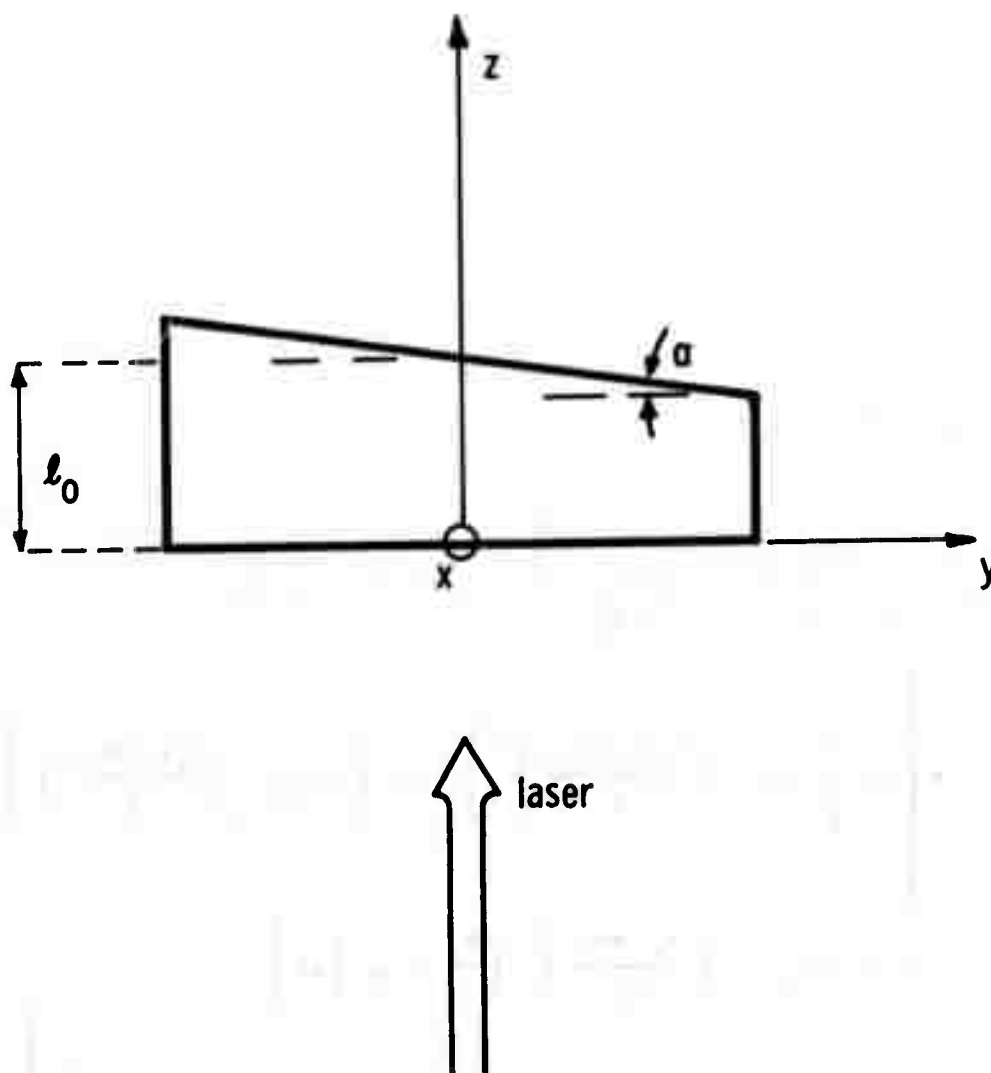


FIG. 34--Geometry for SHG in a wedged platelet.

x and y direction much larger than the spot size, we find

$$\begin{aligned}
 P_{2out} &= \iint_{-\infty}^{\infty} I_2(x,y) dx dy \\
 &= \frac{128\eta_0^3 \omega_1^2 d^2 I_1^2}{(n_2 + 1)^2 (n_1 + 1)^4} \iint_{-\infty}^{\infty} S(l_0 - y \tan \alpha) e^{-4 \frac{x^2 + y^2}{w_1^2}} dx dy, \quad (B.3)
 \end{aligned}$$

and using

$$\int_{-\infty}^{\infty} e^{-Ay - (4y^2/w_1^2)} dy = \frac{\sqrt{\pi} w_1}{2} \exp \left(\frac{w_1^2 A}{4} \right), \quad (B.4)$$

we rewrite Eq. (B.3) as

$$\begin{aligned}
 P_{2out} &= \frac{128\eta_0^3 \omega_1^2 d^2 P_{1out}^2}{(n_2 + 1)^2 (n_1 + 1)^4 \pi w_1^2} \left[(\Delta k)^2 + \left(\frac{\alpha_2}{2} - \alpha_1 \right)^2 \right]^{-1} \\
 &\times \left\{ \exp \left[-\alpha_2 l_0 + \left(\frac{\alpha_2 w_1 \tan \alpha}{4} \right)^2 \right] + \exp \left[-2\alpha_1 l_0 + \left(\frac{\alpha_1 w_1 \tan \alpha}{2} \right)^2 \right] \right. \\
 &- 2 \cos \left[\Delta k l_0 - 2 \left(\frac{w_1 \tan \alpha}{4} \right)^2 \left(\frac{\alpha_2}{2} + \alpha_1 \right) \Delta k \right] \\
 &\times \left. \exp \left[- \left(\frac{\alpha_2}{2} + \alpha_1 \right) l_0 + \left(\frac{w_1 \tan \alpha}{4} \right)^2 \left(\left(\frac{\alpha_2}{2} + \alpha_1 \right)^2 - (\Delta k)^2 \right) \right] \right\} \quad (B.5)
 \end{aligned}$$

Equation (B.5) is the final result of this appendix.

EVALUATION OF THE INTRABAND ABSORPTION INTEGRAL

In this appendix we evaluate the integral in Eq. (6.72). Denoting the integral by S we have

$$S = \int |M|^2 e^{E_1/kT} \delta(E_1 - E_i - \hbar\omega) d^3k . \quad (C.1)$$

Let ΔE represent the energy difference at $k = 0$ between the v_1 and the v_i band. This gives

$$\begin{aligned} E_1 - E_i &= \Delta E - \frac{\hbar^2}{2} \left[\left(\frac{1}{m_{1,\parallel}} - \frac{1}{m_{i,\parallel}} \right) k_{\parallel}^2 + \left(\frac{1}{m_{1,\perp}} - \frac{1}{m_{i,\perp}} \right) k_{\perp}^2 \right] \\ &= \Delta E - \frac{\hbar^2}{2} \left[\frac{k_{\parallel}^2}{\Delta m_{\parallel}} - \frac{k_{\perp}^2}{\Delta m_{\perp}} \right] , \end{aligned} \quad (C.2)$$

where the definitions of Δm_{\parallel} and Δm_{\perp} in Eq. (C.2) should be apparent and according to Table II both are positive. The $v_1 - v_2$ band absorption is most important since this occurs in the middle of the crystal transparency range. For this transition the matrix element in Eq. (6.73) is always of the form

$$|M|^2 = A k_{\parallel}^2 + B k_{\perp}^2 . \quad (C.3)$$

The matrix element for the $v_1 - v_3$ transition also can reduce to this form for certain polarizations. Using Eq. (C.3) we have that the integral in Eq. (C.1) depends only on k_{\parallel}^2 and k_{\perp}^2 , and it is therefore useful to introduce polar coordinates in the (k_x, k_y) plane. After the angular integration we obtain

$$S = 2\pi \int |M|^2 e^{E_1/kT} \delta(E_1 - E_1 - \hbar\omega) k_{\perp} dk_{\perp} dk_{\parallel} , \quad (C.4)$$

which further reduces to

$$S = \frac{2\pi\Delta m_{\perp}}{\hbar^2} \int |M|^2 e^{E_1/kT} dk_{\parallel} ; E_1 - E_1 = \hbar\omega , \quad (C.5)$$

when we make use of Eq. (C.2) and carry out the k_{\perp} integration. In Eq. (C.5) k_{\perp}^2 is replaced by

$$k_{\perp}^2 = \frac{\Delta m_{\perp}}{\Delta m_{\parallel}} k_{\parallel}^2 - \frac{2}{\hbar^2} (\Delta E - \hbar\omega) \Delta m_{\perp} , \quad (C.6)$$

We have to consider separately the two cases $\Delta E > \hbar\omega$ and $\Delta E < \hbar\omega$, and we refer to the integrals as respectively S_1 and S_2 . From the considerations of the integration path, it follows that

$$S_1 = \frac{4\pi\Delta m_{\perp}}{\hbar^2} \int_{k_{\parallel, \min}}^{\infty} |M|^2 e^{E_1/kT} dk_{\parallel} , \quad (C.7)$$

and

$$S_2 = \frac{4\pi\Delta m_{\perp}}{h^2} \int_0^{\infty} |M|^2 e^{E_1/kT} dk_{\parallel} \quad , \quad (C.8)$$

where

$$k_{\parallel, \min} = \sqrt{(2/h^2)(\Delta E - \hbar\omega)\Delta m_{\parallel}} \quad . \quad (C.9)$$

With the definitions

$$\epsilon = \Delta E - \hbar\omega \quad , \quad (C.10)$$

and

$$K = \frac{\Delta m_{\perp}}{m_{1,\parallel}} + \frac{\Delta m_{\perp}}{m_{1,\perp}} \quad , \quad (C.11)$$

we can express the integrals as

$$S_1 = S_2 [1 - \operatorname{erf}(\sqrt{K\epsilon/kT})] + \frac{4\pi\Delta m_{\perp}}{h^5} \frac{kT}{K} \frac{A\Delta m_{\parallel} + B\Delta m_{\perp}}{\sqrt{2\Delta m_{\parallel}\epsilon}} \exp\left[-\frac{\epsilon}{k} \frac{\Delta m_{\parallel}}{m_{1,\parallel}}\right] \quad , \quad (C.12)$$

and

$$S_2 = \frac{2\pi\Delta m_{\perp} kT}{h^5} \sqrt{\frac{2\pi \Delta m_{\parallel} kT}{K}} \left[\frac{A\Delta m_{\parallel} + B\Delta m_{\perp}}{K} - \frac{2\epsilon\Delta m_{\perp} B}{kT} \right] \\ \times \exp \left[-\frac{\epsilon}{kT} \frac{\Delta m_{\perp}}{m_{1,\perp}} \right] \quad . \quad (C.13)$$

In Eq. (C.12) $\text{erf}(x)$ is the error function defined by

$$\text{erf}(x) = \frac{2}{\sqrt{\pi}} \int_0^x e^{-t^2} dt \quad . \quad (C.14)$$

In Chapter VI, Section A.5 we use these integrals to calculate the intraband absorption in CdGeAs_2 .

REFERENCES

1. C.H.L. Goodman, "A New Group of Compounds with the Type (Chalcopyrite) Structure", *Nature* 179, 200 (1954).
2. C.H.L. Goodman, "The Prediction of Semiconducting Properties in Inorganic Compounds", *J. Phys. Chem. Solids* 6, 3 (1958).
3. A.S. Borschevskii, N.A. Goryunova, F.P. Kesamanly, and D.N. Nasledov, "Semiconducting $A^{II}B^{IV}C_2^V$ Compounds," *Phys. Stat. Solidus*, 21, 9 (1967).
4. G.D. Boyd and D.A. Kleinman, "Parametric Interactions of Focused Light Beams", *J. Appl. Phys.* 39, 3597 (1968).
5. S.E. Harris, "Tunable Optical Parametric Oscillators", *Proc. IEEE*, 57, 2096 (1969).
6. J.F. Nye, Physical Properties of Crystals (Oxford University Press, Oxford, 1957).
7. R.C. Miller, "Optical Second Harmonic Generation in Piezoelectric Crystals", *Appl. Phys. Letters* 5, 17 (1964).
8. M. Born and E. Wolf, Principles of Optics, (Pergamon Press, New York, 1965).
9. C.A. Klein and R.I. Rudko, " CO_2 Laser Radiation Absorption in Semi-Insulating Gallium Arsenide", *Appl. Phys. Letters* 13, 129 (1968).

10. D.C. Hanna, B. Luther-Davies, H.N. Rutt, R.C. Smith, and C.R. Stanley, "Q-Switched Laser Damage of Infrared Nonlinear Materials", IEEE J. QE-8, 317 (1972).
11. J.J. Wynne and N. Bloembergen, "Measurement of the Lowest-Order Nonlinear Susceptibility in III-V Semiconductors by Second-Harmonic Generation with a CO₂ Laser", Phys. Rev. 188, 1211 (1969).
12. S.C. Abrahams and J.L. Bernstein, "Crystal Structure of Luminescent ZnSiP₂", J. Chem. Phys. 52, 5607 (1970).
13. H. Pfister, "Kristallstruktur von ternären Verbindungen der Art A^{II}_B^{IV}₂C^V", Acta Cryst. 11, 221 (1958).
14. D.A. Kleinman, "Nonlinear Dielectric Polarization in Optical Media", Phys. Rev. 126, 1977 (1962).
15. D.S. Chemla, "Dielectric Theory of Tetrahedral Solids: Application to Ternary Compounds with Chalcopyrite Structure", Phys. Rev. Letters 26, 1441 (1971).
16. J.L. Shay, E. Buehler, and J.H. Wernick, "Electroreflectance, Absorption Coefficient, and Energy-Band Structure of CdGeP₂ near the Direct Energy Gap", Phys. Rev. B4, 2479 (1971).
17. J.E. Rowe and J.L. Shay, "Extension of the Quasicubic Model to Ternary Chalcopyrite Crystals", Phys. Rev. B3, 451 (1971).
18. C.K.N. Patel, R.E. Slusher, and P.A. Fleury, "Optical Non-linearities due to Mobile Carriers in Semiconductors", Phys. Rev. Letters, 17, 1011 (1966).

19. P.A. Wolff and G.A. Pearson, "Theory of Optical Mixing by Mobile Carriers in Semiconductors", Phys. Rev. Letters 17, 1015 (1966).
20. E.O. Kane, "Band Structure of Indium Antimonide", J. Phys. Chem. Solids 1, 249 (1957).
21. N.A. Goryunova, A.S. Poplavnoi, Yu. I. Polygalov, and V.A. Chaldyshev, "Energy Band Structure of Ternary Diamond-Like $A^2B^4C_5^2$ - Type Semiconductors", Phys. Stat. Solidus 32, 9(1970).
22. J.O. Dimmock, Semiconductors and Semimetals, vol. 3: Optical Properties of III-V Compounds, ed. R.K. Willardson and A.C. Beer (Academic Press, New York, 1967).
23. J.L. Shay and E. Buehler, "Electroreflectance Spectra of $CdSiAs_2$ and $CdGeAs_2$ ", Phys. Rev. B3, 2598 (1971).
24. F.H. Pollak and M. Cardona, "Piezo-Electroreflectance in Ge, GaAs, and Si", Phys. Rev. 172, 816 (1968).
25. A. Gavini and M. Cardona, "Modulated Piezoreflectance", Phys. Rev. B1, 672 (1969).
26. H. Ehrenreich, "Band Structure and Transport Properties of Some 3-5 Compounds", J. Appl. Phys. 32, 2155 (1961).
27. R.A. Smith, Semiconductors (Cambridge University Press, London, 1968).
28. A.A. Vaipolin, F.M. Gashimzade, N.A. Goryunova, F.P. Kesamanly, D.N. Nasledov, E.O. Osmanov, and Yu. V. Rud, "Investigation of the Physicochemical and Electric Properties of Crystals of some Ternary Semiconductor Compounds of the $A^{II}B^{IV}C_2^V$ Type". Academy of Science of the USSR, Bull. Phys. Series 28, 984 (1964).

29. G.D. Boyd, E. Buehler, F.G. Storz and J.H. Wernick, "Linear and Nonlinear Optical Properties of Ternary $A^{II}B^{IV}C_2^V$ Chalcopyrite Semiconductors", IEEE J. of Quant. Elect. QE-8, 419 (1972).
30. L.B. Zlatkin, Yu, F. Markov, and I.K. Polushina, "Values of the Effective Mass of Conduction Electrons in $CdGeAs_2$ ", Sov. Phys. Semiconductors 3, 1336 (1970).
31. O.V. Emel'yanenko, F.P. Kesamanly, I.K. Polushina, and V.A. Skripkin, "Thermoelectric Power and Effective Mass of Carriers in $CdGeAs_2$ ", Sov. Phys. Semiconductors 5, 304 (1971).
32. L.J. van der Pauw, "A Method of Measuring the Specific Resistivity and Hall Effect of Discs of Arbitrary Shape", Phillips Research Reports 13, 1 (1958).
33. L.F. van der Pauw, "A Method of Measuring the Resistivity and Hall Coefficient on Lamellae of Arbitrary Shape", Phillips Tech. Rev. 20, 220 (1959).
34. N.A. Goryunova, F.P. Kesamanly, E.O. Osmanov, and Yu, V. Rud, "Study of Certain Properties of $CdGeAs_2$ ", Izv.Akad. Nauk USSR, Inorg. Mater. 1, 814 (1965).
35. Handbook of Chemistry and Physics, 51st edition.
36. American Institute of Physics Handbook, 2nd edition.
37. A.S. Borshchevskii and N.D. Roenkov, "Phase Diagram of the Cadmium-Germanium-Arsenic System", Russian J. of Inorganic Chemistry 14, 8 (1969).
38. R.S. Feigelson, private communication.

39. M.P. Leroux-Hugan, "Propriétés de Quelques Composés Ternaires Semiconducteurs", Comptes Rendus 256, 118 (1963).
40. L.S. Birks, Electron Probe Microanalysis (Interscience Publications, New York, 1963).
41. R.L. Byer, "Parametric Fluorescence and Optical Parametric Oscillation", Ph.D. dissertation, Microwave Laboratory, W.W. Hansen Laboratories of Physics, Stanford University, Stanford, California.
42. L.B. Kruezer, "Single Mode Oscillation of a Pulsed Singly Resonant Optical Parametric Oscillator", Appl. Phys. Letters 15, 263 (1969).
43. C.K.N. Patel, R.E. Slusher, and P.A. Fleury, "Optical Nonlinearities due to Mobile Carriers in Semiconductors", Phys. Rev. Letters 17, 1011 (1966).
44. P.A. Wolff and G.A. Pearson, "Theory of Optical Mixing by Mobile Carriers in Semiconductors", Phys. Rev. Letters 17, 1015 (1966).
45. J.E. Midwinter and J. Warner, "The Effects of Phase Matching Method and of Crystal Symmetry on the Polar Dependence of Third-Order Nonlinear Optical Polarization", Brit. J. Appl. Phys. 14, 1667 (1965).
46. W.L. Bond, "Measurement of the Refractive Indices of Several Crystals", J. Appl. Phys. 36, 1674 (1965).
47. M. Cardona, "Temperature Dependence of the Refractive Index and the Polarizability of Free Carriers in some III-V Semiconductors", Int. Conf. on Semicond. Physics, Prague, 1960 (Academic Press, New York, 1961) 388.

48. K.H. Hellwege and A.M. Hellwege, Numerical Data and Functional Relationship Series - Part II, Elastic, Piezoelectric and Related Constants of Crystals, ed - Landolt and Bornstein, (Springer-Verlag, 1969).
49. P.D. Maker, R.W. Terhune, M. Nisenoff and C.M. Savage, "Effects of Dispersion and Focusing on the Production of Optical Harmonics", Phys. Rev. Letters 8, 21 (1962).
50. G.D. Boyd, H. Kasper and J.H. McFee, "Linear and Nonlinear Optical Properties of AgGaS_2 , CuGaS_2 , and CuInS_2 , and Theory of the Wedge Technique for the Measurement of Nonlinear Coefficients", IEEE J. Quant. Elect. QE-7, 563 (1971).
51. O. Madelung, Physics of III-V Compounds (John Wiley and Sons, New York, 1964).
52. H.Y. Fan, W. Spitzer and R.F. Collins, "Infrared Absorption in n-Type Germanium", Phys. Rev. 101, 566 (1956).
53. S. Visvanathan, "Free Carrier Absorption Due to Polar Modes in the III-V Compound Semiconductors", Phys. Rev. 120, 376 (1960).
54. S. Visvanathan, "Free Carrier Absorption Arising From Impurities in Semiconductors", Phys. Rev. 120, 379 (1960).
55. A.H. Kah, "Theory of the Infrared Absorption of Carriers in Germanium and Silicon", Phys. Rev. 97, 1647 (1955).
56. G.F. Bassani, Proc. of the International School of Physics "Enrico Fermi", Course XXXIV, The Optical Properties of Solids, ed. F. Tauc (Academic Press, New York, 1966).

57. C.C. Lee and H.Y. Fan, "Two-Photon Absorption and Photoconductivity in GaAs and InP", Appl. Phys. Letters 20, 18 (1972).
58. W.B. Gandrud and R.L. Abrams, "Reduction in SHG Efficiency in Tellurium by Photoinduced Carriers", Appl. Phys. Letters 17, 302 (1970).
59. F.D. Taynai, R. Targ, and W.B. Tiffany, "Investigation of Tellurium for Frequency Doubling with CO₂ Lasers", IEEE J. Quant. Elect. QE-7, 412 (1971).
60. F. Warner, D.S. Robertson, and K.F. Hulme, "The Temperature Dependence of Optical Birefringence in Lithium Niobate", Phys. Letters 20, 163 (1966).
61. N.A. Goryunova, L.B. Zlatkin, and E.K. Ivanov, "Optical Anisotropy of A²B⁴C₂⁵ Crystals", J. Phys. Chem. Solids 31, 2557 (1970).
62. F.H. McFee, G.D. Boyd and P.H. Schmidt, "Redetermination of the Nonlinear Optical Coefficients of Te and GaAs by Comparison with Ag₃SbS₃", Appl. Phys. Letters 17, 57 (1970).
63. R.L. Byer, H. Kildal, and R.S. Feigelson, "CdGeAs₂ - A New Non-linear Crystal Phasematchable at 10.6 μ m", Appl. Phys. Letters 19, 237 (1971).
64. N.A. Goryunova, S.M. Ryvkin, I.M. Fishman, G.P. Shpen'kov, and I.D. Yaroshetskii, "Generation of Second Harmonic in Ternary Semiconducting Compounds", Soviet Physics - Semiconductors 2, 1272 (1969).

65. G.D. Boyd, W.B. Gandrud, and E. Buehler, "Phasematched Up-Conversion of $10.6\ \mu$ Radiation in ZuGeP_2 , "Appl. Phys. Letters 18, 446 (1971).
66. B. Kh. Mamedov and E.O. Osmanov, "Infrared Absorption in p-type CdGeAs_2 Crystals", Sov. Phys. - Semicond. 5, 1120 (1972).